

**Boiling as a mechanism for colour zonations
observed at the Byrud emerald deposit, Eidsvoll,
Norway**

by

Lara Ellen Loughrey

B.Sc., Simon Fraser University, 2011

Thesis Submitted In Partial Fulfillment of the
Requirements for the Degree of
Master of Science

in the
Department of Earth Sciences
Faculty of Science

© Lara Ellen Loughrey 2013
SIMON FRASER UNIVERSITY
Fall 2013

All rights reserved.

However, in accordance with the *Copyright Act of Canada*, this work may be reproduced, without authorization, under the conditions for "Fair Dealing." Therefore, limited reproduction of this work for the purposes of private study, research, criticism, review and news reporting is likely to be in accordance with the law, particularly if cited appropriately.

Approval

Name: Lara Ellen Loughrey
Degree: Master of Science (Earth Sciences)
Title of Thesis: *Boiling as a mechanism for colour zonation observed at the Byrud emerald deposit, Eidsvoll, Norway*
Examining Committee: **Chair:** Daniel Gibson
Associate Professor

Dr. Dan Marshall
Senior Supervisor
Professor

Dr. Derek Thorkelson
Supervisor
Professor

Dr. Lee Groat
External Examiner
Professor, Department of
Earth, Ocean and Atmospheric
Sciences
University of British Columbia

Date Defended/Approved: December 13, 2013

Partial Copyright Licence



The author, whose copyright is declared on the title page of this work, has granted to Simon Fraser University the non-exclusive, royalty-free right to include a digital copy of this thesis, project or extended essay[s] and associated supplemental files (“Work”) (title[s] below) in Summit, the Institutional Research Repository at SFU. SFU may also make copies of the Work for purposes of a scholarly or research nature; for users of the SFU Library; or in response to a request from another library, or educational institution, on SFU’s own behalf or for one of its users. Distribution may be in any form.

The author has further agreed that SFU may keep more than one copy of the Work for purposes of back-up and security; and that SFU may, without changing the content, translate, if technically possible, the Work to any medium or format for the purpose of preserving the Work and facilitating the exercise of SFU’s rights under this licence.

It is understood that copying, publication, or public performance of the Work for commercial purposes shall not be allowed without the author’s written permission.

While granting the above uses to SFU, the author retains copyright ownership and moral rights in the Work, and may deal with the copyright in the Work in any way consistent with the terms of this licence, including the right to change the Work for subsequent purposes, including editing and publishing the Work in whole or in part, and licensing the content to other parties as the author may desire.

The author represents and warrants that he/she has the right to grant the rights contained in this licence and that the Work does not, to the best of the author’s knowledge, infringe upon anyone’s copyright. The author has obtained written copyright permission, where required, for the use of any third-party copyrighted material contained in the Work. The author represents and warrants that the Work is his/her own original work and that he/she has not previously assigned or relinquished the rights conferred in this licence.

Simon Fraser University Library
Burnaby, British Columbia, Canada

revised Fall 2013

Abstract

The Byrud emerald deposit was first discovered in the early 1860s, near Lake Mjøsa, southern Norway. From a geological, gemmological, and geochemical perspective, the Byrud emeralds are of great interest as they are vanadium-rich rather than chromium-rich, which is uncommon for the majority of emeralds worldwide. The emerald deposit genesis is consistent with a typical granite-related emerald vein system from dominantly magmatic fluid sources. Emerald mineralization occurs within pegmatite veins which are hosted within Cambrian black shale and Late Carboniferous quartz syenite sills, and intruded by a Permo-Triassic alkaline granite. Muscovite from an emerald-bearing pegmatite at Byrud yielded an Ar-Ar plateau age of 233.4 ± 2.0 Ma. The emerald display colour zonation alternating between emerald and beryl. Two dominant fluid inclusion types are identified: two-phase (vapour+liquid) and three-phase (brine+vapour+halite) fluid inclusions. Raman analyses indicate molar gas fractions for CO₂, N₂, CH₄, and H₂S are approximately 0.8974, 0.0261, 0.0354, and 0.0410, respectively. Formational temperatures and pressures of approximately 160 °C to 385 °C and below 1000 bars were derived from fluid inclusion data and lithostatic pressure estimates from fluid inclusion studies within the Oslo Paleorift.

The emerald from the Byrud mine displays growth zoning and banding from green emerald to colourless beryl. The use of chemical analyses, fluid inclusions and petrography is consistent with boiling as a mechanism for this distinct 'striped' colour zonation or banding. These zones are due to enrichment of vanadium and chromium in the green bands which host salt-saturated aqueous primary fluid inclusions with an overall 31 mass percent NaCl equivalent salinity. Vapour-rich primary fluid inclusions dominate within the colourless bands of the zoned emerald. The chemical compositions of the salt-saturated and the vapour-rich inclusions indicate they represent the coexisting liquid and vapour portions of a two-phase boiling system. This "boiling" formational model has application to not only other emerald deposits, but also other zoned gem deposits worldwide.

Keywords: emerald; beryl; Norway; fluid inclusions; stable isotopes; Ar-Ar dating

Dedication

This thesis is dedicated to my parents for their unconditional love, support and encouragement in all of my life's endeavours.

Acknowledgements

I would like to convey my gratitude to the following individuals for providing me with the inspiration to embark on my MSc candidature. My deepest thanks are directed to my supervisor, Prof. Dan Marshall, who guided me through both my undergraduate and graduate career. I appreciate his vast knowledge and skills in many areas, and his assistance in writing reports, papers and scholarship applications. Most importantly, I sincerely value his mentorship and support throughout all these years. I would like to thank Peter Ihlen whose contributions were very important to this project. His extensive experience and knowledge of the deposit proved to be beneficial in my understanding of the tectonic and mineralogical relationships at Byrud. A very special thank you goes to Arfinn Juliussen for his field assistance and enjoyable company during my fieldwork in Norway. My time in the field would not have been the same without him. I'd like to thank Fred Steiner Nordrum of the Norsk Bergverksmuseum in Kongsberg for sharing his expertise on the deposit and providing samples to this project. His guidance around the Kongsberg Silver Mine has added to my increasing knowledge of ore deposits and I am grateful for the opportunity to visit the mine. Additional samples donated by Bjorn Skår of Norsk Naturafeln were instrumental in determining fluid timing relationships. I'd like to especially thank Asbjørg and Sturla Vandli for their wonderful hospitality and great company during my stay at their farm in Eidsvoll. Access to the Byrud Mine by the current owners, Anne-Greta Røssa and Ole Jørgen Bjørnstad, is also gratefully acknowledged. Big thanks to Prof. Rune Selbekk for allowing me into the mineral collection at the Geological Museum in Oslo and donating samples to this project.

The isotopic work by Kerry Klassen of QFIR Stable Isotope Lab at Queen's University is thankfully acknowledged, as well as Peter Jones of Carleton University for the initial microprobe analyses. I would also like to thank Prof. Mati Raudsepp and Edith Czech at the University of British Columbia for guiding me on electron microprobe analysis of emerald. Thanks are due to Janet Gibates at the University of British Columbia who obtained Ar-Ar ages for the emerald. I would like to thank the other members of my committee, Prof. Derek Thorkelson, for his valuable suggestions that improved this thesis and to Prof. Lee Groat (University of British Columbia) for taking time out from his busy schedule to serve as my external examiner. I would also like to

thank Prof. Dan Gibson for the many conversations and lectures about the tectonic history of the Northern Cordillera, and for a great cross-Cordillera field trip. As well as thank Kevin Cameron for his advice and mentorship during my undergraduate and graduate career. Finally, this thesis would not be possible without the financial support from Simon Fraser University and the Department of Earth Sciences.

I would especially like to thank my family and friends for the support they provided me through my academic studies. I'd like to acknowledge my former labmate, TA, and good friend, Meghan, whose advice and shared passion for rocks (especially emeralds), motivated me to produce a thesis I am proud of. A very special thanks goes to Ashton for his support and motivation throughout my undergraduate and graduate career, especially reminding me of life outside of academia. A big hug goes to Meg, probably the best companion a graduate student could have. I am extremely grateful for my girls Amanda, Hannah, Cirisse, Justine, Megan and Taylor for their support and understanding throughout this experience. Special thanks goes to Waldo Sciences for their vast knowledge of Photoshop and assistance with this thesis. Thanks to all of my colleagues, faculty and staff at SFU and UBC without whom I would not have survived SFU and finished this thesis, especially Andrea, Nancy, Jolene, Stacy, Joe, Jerry and John Mayer.

Table of Contents

Approval.....	ii
Partial Copyright Licence	iii
Abstract.....	iv
Dedication.....	v
Acknowledgements	vi
Table of Contents.....	vii
List of Tables.....	x
List of Figures.....	xii
Preface.....	xiii
1. Introduction	1
1.1. Emerald.....	1
1.2. Goals of this thesis and previous work.....	3
1.3. Location, access, exposure, and sampling	5
1.4. Regional geology of Southern Norway	5
1.5. Local Geology	9
References.....	13
2. Petrography	16
2.1. Host rocks and alteration.....	16
2.1.1. Unaltered bituminous black shale.....	18
2.1.2. Metamorphosed black shale—biotite hornfels.....	18
2.1.3. Syenitic sill	20
2.1.4. Granitic rocks	21
2.2. Veins	23
2.3. Summary and discussion.....	27
References.....	30
3. Boiling as a mechanism for colour zonations observed at the Byrud emerald deposit, Eidsvoll, Norway: fluid inclusion, stable isotope and Ar-Ar studies*	31
3.1. Abstract.....	32
3.2. Introduction	33
3.3. Geologic Setting	34
3.4. Local Geology and Vein Petrology.....	36
3.5. Field and Laboratory Methods	39
3.6. Results	41
3.6.1. Emerald Composition.....	41
3.6.2. Fluid Inclusions	47
3.6.3. Microthermometry	50
3.6.4. Stable isotopes	55
3.6.5. Ar-Ar Geochronology	57
3.7. Discussion.....	61
3.7.1. Pressure-temperature constraints	61
3.7.2. Emerald mineralization model and classification	64

3.8. Conclusions.....	66
3.9. Acknowledgements	67
References.....	68
4. Additional Research and Deposit Model.....	72
4.1. Introduction	72
4.2. Electron microprobe analyses and prediction of H ₂ O content in emerald.....	72
4.3. Deposit model and comparison to other zoned emerald deposits	78
References.....	83
5. Conclusions.....	85
Appendices.....	87
Appendix A: Sample locations and descriptions	88
Appendix B: Bulk rock geochemistry	95
Appendix C: Fluid inclusion data	108
Appendix D: Electron microprobe analysis	114

List of Tables

Table 3-1. Electron microprobe compositions along a traverse of the Byrud emerald.	45
Table 3-2. Microthermometric measurements on the fluid inclusions from emerald at Byrud	53
Table 3-3. Stable isotope data for the Byrud emerald deposit.....	57
Table 3-4. $^{40}\text{Ar}/^{39}\text{Ar}$ Ages from vein muscovite in textural equilibrium with emerald.	59
Table 4-1. Channel H_2O and Na_2O contents (wt.%) of various emerald deposits worldwide	77
Table A-1. Listed locations, descriptions, samples, and measured structures from field stations.....	88
Table A-2. Sample descriptions of samples taken from the Byrud deposit by Peter Ihlen	92
Table A-3. Sample and field photographs taken at the Byrud deposit.....	93
Table B-1. Major, minor, and trace element compositions of whole rock samples	97
Table B-2. Quality control data for whole rock geochemical standards and blanks.....	100
Table C-1. Microthermometric measurements on the fluid inclusions from the Byrud deposit in emerald, quartz and fluorite.	108
Table D-1. Compositions of the Byrud emerald from electron microprobe analysis	115

List of Figures

Figure 1-1. Cyclosilicate structure of beryl oriented down the c axis.....	2
Figure 1-2. Evolutionary timescale of the Oslo Rift.....	8
Figure 1-3. Idealized vein cross-section of mineralized pegmatite.....	11
Figure 1-4. Idealized cross section across the Byrud mine.....	12
Figure 2-1. Scanned thin sections of host rocks to the emerald veins	17
Figure 2-2. Biotite hornfels displaying laminated bands and lenses of sulphides.....	19
Figure 2-3. Monzogranite in thin section.....	22
Figure 2-4. Pegmatite veins in thin section.....	24
Figure 2-5. Photomicrograph of emerald-bearing pegmatite.....	26
Figure 2-6. Photomicrographs of sample LEL12-FIB, a beryl-free vein in plane-polarized transmitted light (PPL) and cross-polarized transmitted light (XPL)	27
Figure 2-7. Paragenetic sequence of vein and alteration minerals	28
Figure 3-1. Geologic map of the Eidsvoll area, showing the locality of the Byrud emerald deposit on the western shore of Lake Mjøsa	33
Figure 3-2. Topographic map showing location of the emerald mine on the western shore of Lake Mjøsa, Norway	37
Figure 3-3. Hand specimen collected from the Byrud mine displaying the contemporaneous relationship of the pegmatite/aplite and emerald.....	38
Figure 3-4. Ternary FeO-Cr ₂ O ₃ -V ₂ O ₃ (mass %) plot of Byrud emerald	42
Figure 3-5. Mass percent oxide data for selected oxides in emerald along a microprobe traverse.....	43
Figure 3-6. Al versus the sum of other Y-site cations, in atoms per formula unit. The Byrud emerald compositions (dark gray plus signs) are superimposed on worldwide emerald data. The second graph is an Mg+Mn+Fe versus monovalent channel-site cations, in atoms per formula unit.....	44
Figure 3-7. Photomicrograph of a boiling assemblage in quartz	47

Figure 3-8. Zoned emerald from the Byrud deposit with colour zonations parallel to the c-axis of the crystal, as well as parallel to the basal pinacoid	49
Figure 3-9. Raman microprobe spectra of CO ₂ , N ₂ , CH ₄ , and H ₂ S in sample LL05B-1	51
Figure 3-10. Channel δD H ₂ O versus δ ¹⁸ O for the Byrud emerald (green stars) superimposed upon data from a number of world localities	56
Figure 3-11. ⁴⁰ Ar- ³⁹ Ar gas release spectra showing plateau age of Middle Triassic.	58
Figure 3-12. Pressure-temperature diagram showing the schematic constraints for the Byrud emerald veins derived from isochore constraints for a 30.7 weight percent NaCl fluid inclusion	62
Figure 4-1. Mass percent oxide data for selected oxides in emerald along a microprobe traverse	74
Figure 4-2. Photomicrograph of emerald crystal, sample LEL12-veinB-1	75
Figure 4-3. Channel H ₂ O versus emerald Na ₂ O contents for a variety of emerald deposits	78
Figure 4-4. Colour zonations parallel to the basal pinacoid from dark green (emerald) to light blue to colourless beryl. Sample from the Erongo deposit, Namibia.	80
Figure 4-5. Schematic diagram showing the relationship of co-existing liquid and vapour phases of a saline fluid within a vein/fracture system	82

Preface

This thesis presents new data and a deposit model for the formation of colour zonations observed in the Byrud emerald, one of the most vanadium-rich emerald deposits in the world. Chapter 1 is an introduction to beryl and emerald occurrences, specifically previous work at the Byrud mine and a description of the local and regional geological setting. Chapter 2 presents the petrology and mineralogy of the host rock and veins. Full rock descriptions accompanying this section are provided in Appendix A. Chapter 3 is a published peer-reviewed journal article in *Geofluids*, entitled 'Boiling as a mechanism for colour zonations observed at the Byrud emerald deposit, Eidsvoll, Norway: fluid inclusion, stable isotope and Ar-Ar studies' (Loughrey et al., 2013). This paper discusses the model of formation of the emerald through temperature and pressure conditions, fluid conditions and sources and presents an age for the emerald mineralization. Additional research and summary of the deposit model and its relation to other zoned emerald localities are presented in Chapter 4.

The version of the paper presented in Chapter 3 was co-authored by D. Marshall, P. Ihlen and P. Jones, who contributed to editing and the understanding of the emerald mineralization at the Byrud deposit. Marshall was actively involved in the interpretation of stable isotope and fluid inclusion work and was a major contributor to editing and writing. Ihlen contributions were very important in understanding field relationships between the host rocks and emerald mineralization in the area. His extensive experience in metallogenic deposits in the Oslo Rift greatly added to interpreting the tectonic and mineralogical relationships at the Byrud deposit. Jones contributed to the initial microprobe analyses, which was added to the geochemical analyses of the zoning observed in the emerald crystals. To minimize duplication some figures referred to in Chapter 1 and 2 are contained solely in the published paper (Chapter 3).

1. Introduction

1.1. Emerald

Few European occurrences of emerald are recorded in the literature. These deposits include Rila in Bulgaria, Val Vigezzo in Italy, Habachtal in Austria, Franqueira in Spain and Volodarsk in Ukraine (Groat et al., 2008; Kazmi and Snee, 1989). Emerald of the Habachtal deposit is the most studied European emerald deposit and was mined as early as the 1860s (Kazmi and Snee, 1989). This emerald deposit is hosted within biotite and chlorite schist which formed along the deposit margins during metasomatic alteration of serpentinites. In contrast the Rila emerald deposit from Bulgaria is associated with pegmatite veins along the contact zone between serpentinitized igneous rocks and biotite gneisses (Groat et al., 2008; Kazmi and Snee, 1989). Other than Byrud, there are no emerald deposits in Europe which display colour zonation in the form of green to clear colouration in adjacent growth zones. Other emerald localities that display similar colour zoning include Emmaville-Torrington in Australia, Erongo in Namibia, Leydsdorp in South Africa, some emerald from the Swat district, Pakistan, and Kafubu in Zambia (Hammarstrom, 1989; Grundmann and Morteani, 1989; Zwaan et al. 2005).

Emerald is the green gem variety of beryl containing chromium and vanadium and is the third most valuable gemstone (Groat et al., 2008). Beryl crystallises in the hexagonal system and is structured with interconnected six-membered rings of silica tetrahedra producing channels that parallel the *c* axis of the crystal structure. These channels accommodate a range of fluids and dissolved cations. A variety of trivalent and divalent cations (Fe, Mg, Sc, Mn, Ga, Ni, Cu) can be substituted at the same sites as Cr and V in the beryl structure, giving rise to different colour varieties of gem-quality beryl. Beryl's ideal chemical formula is $\text{Be}_3\text{Al}_2\text{Si}_6\text{O}_{18}$, but can be better defined by the formula $(\text{Be}_{3-X}, \text{Li}_{Y,X-Y})(\text{Al}, \text{Fe}, \text{Cr}, \text{V}, \text{Sc})^{3+}_{2-Z}(\text{Fe}, \text{Mg}, \text{Mn})^{2+}_Z\text{Si}_6\text{O}_{18} \cdot (\text{Na}, \text{K}, \text{Rb}, \text{Cs})_{2X-Y+Z}(\text{H}_2\text{O}, \text{He}, \text{Ar})_{\leq 2-(2X-Y+Z)+\text{Na}}$ where $(Y \leq 2)$, $(X \geq Y)$, $(Z < 2)$, and $(2X - Y + Z)$, and Na, K, Rb, Cs, H₂O, He, and Ar

cations can occupy vacant channel sites. The green gem variety of beryl, known as emerald, results from the substitution of Cr and/or V into the Al-site in the beryl crystal structure.

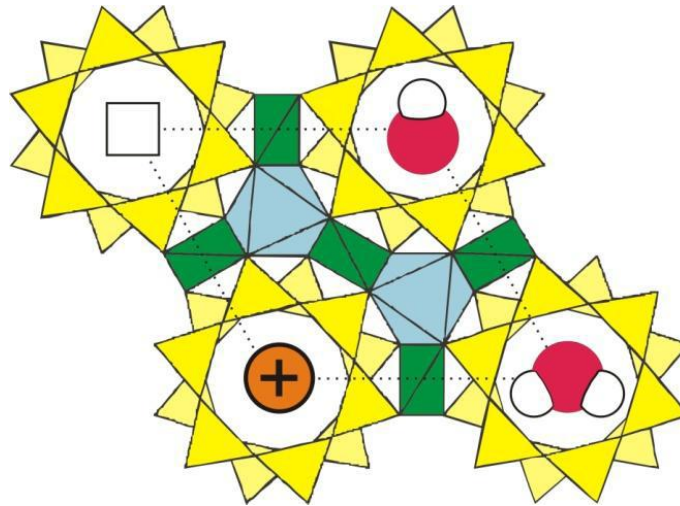


Figure 1-1. Cyclosilicate structure of beryl oriented down the c axis. Tetrahedral beryllium sites are in green, silica tetrahedron in yellow, aluminum octahedral in blue. The silica tetrahedral forms hollow channels which are occupied by water molecules (red) and dissolved cations (orange). Diagram modified from Turner and Groat (2007) and Hewton (2012).

Emerald forms through element partitioning and the interaction of Be-rich fluids with Cr and/or V. Beryl is relatively rare and very little beryllium fractionates into the upper continental crust. Chromium and vanadium are less common in the continental crust (Rudnick and Gao, 2003), and tend to be more concentrated in dunites, peridotites, and basalts, and their metamorphic counterparts. In some deposits, high concentrations of chromium and vanadium have been recorded in black shale (Schwarz et al., 2002). Beryllium tends to be more concentrated in rocks such as granite, pegmatite, more rarely shale and their metamorphic counterparts. There are three distinct deposit types documented in the literature (Groat et al., 2007). A common classification scheme for emerald deposits defines a Type 1 deposit related to a granitic intrusion and Type 2 deposits controlled by tectonic structures (Groat et al., 2007; Schwarz and Giuliani,

2001; Schwarz et al., 2001). The Byrud emerald is categorized as a Type 1 deposit. However, the majority of the host rocks are aluminum-rich shale rather than schist. Emerald mineralization at this locality occurs in clay-filled cavities within pegmatite, quartz-muscovite, and quartz veins. Most emerald deposits fall in the first category and are subdivided on the presence or absence of schist at the contact zone. Type 2 deposits are subdivided into schist without pegmatites and black shale with veins and breccias (Schwarz and Giuliani, 2001; Schwarz et al., 2001). A third deposit type has also been postulated characterizing the famous Colombian deposits based on emerald precipitation via sulphate reduction in veins hosted in Early Cretaceous organic-rich black shale to carbonaceous shale (Cheilletz and Giuliani, 1996). This type of deposit is relatively rare. The most common example of emeralds deriving chromium and vanadium chromophoric material from sediments is one of the world's largest and richest emerald deposit at Muzo, Colombia (Ottaway et al., 1994; Giuliani et al., 1995).

1.2. Goals of this thesis and previous work

The Byrud emerald is one of the few emerald deposits that display colour zonations between emerald and colourless beryl. The goal of this thesis was to investigate the colour zonation within the Byrud emerald and provide a comprehensive study of vanadium-rich Byrud emerald, to describe and characterize its geology, petrogenesis, and geochemistry. This thesis will also establish an age and conditions of emerald mineralization to produce a model for the genesis of emerald at Byrud.

The Byrud emerald deposit was mined between 1899 and 1909 and is one of the rare European occurrences of gemstone emerald. The initial discovery of emerald is not documented, but was probably in the early 1860s, because a collection of Byrud green beryl in the Swedish Natural History Museum was acquired about that time. Preliminary prospecting and blasting occurred during the 1880s. Evelyn Aston, daughter of an English mining prospector, inspected the occurrence on a ski tour on Lake Mjøsa. She initially noted an opening of two meters in height and one meter width, and assessed a gallery measuring approximately 3.5 meters in diameter (Nordrum et al., 2006; Rondeau

et al., 2008). During her next visit, accompanied by a miner, she found gem-quality emerald crystals in small clay-filled pockets. The morphology of the beryl crystals was initially described by Websky (1876) and later after the mine's abandonment in 1909, was described in greater detail by Goldschmidt (1911). Consequently, there have been limited geological and geochemical studies on the Byrud occurrence. The majority of the scientific investigations on the deposit have been an extensive mineralogical study by G. Raade at the Geological Museum in Oslo, identifying 45 different minerals from the Byrud occurrence (Nordrum and Raade, 2006; Rondeau et al., 2008).

The history, geology, and mineralogy of the Byrud deposit were comprehensively described by Nordrum and Raade (2006). A summary of the history and geology is also documented by Rondeau et al. (2008). Their work focussed on the gemmological properties, chemical compositions, spectroscopy and identification of multiphase fluid inclusions, with their results compared with other emerald localities worldwide. Microprobe analysis from Byrud, Norway; Emmaville, Australia; Menzies, Western Australia; and Poona, Western Australia was conducted by Schwarz (1991). Rondeau et al. (2008) characterized both the Byrud and Emmaville-Torrington emerald as distinctly low in concentrations of sodium, magnesium and iron. The crystals from Byrud show extremely low contents of Na₂O (0.06 – 0.10 wt.%) and MgO (0.07 – 0.11 wt.%) with high V₂O₃ (0.88 – 1.53 wt.%) contents (Schwarz, 1991; Rondeau et al., 2008).

Previous fluid inclusion work completed by Ventalon (2009) established two fluid inclusions types (FITs). The first is a two-phase (liquid + vapour) FIT with 5-50 volume percent vapour and a second, three-phase (liquid + vapour + halite) FIT. Microthermometric work completed by Ventalon (2009) indicates the presence of two contrasting saline fluids which either resulted from boiling or the two fluids successively circulated at the deposit. Estimated temperatures and pressures of trapping were roughly 300 °C and 400 to 1100 bars. Extensive microthermometric work was not completed and had not been integrated with isotopic thermobarometry. Giuliani et al. (1998) compiled oxygen isotopic compositions of worldwide emerald deposits and measured δD values of -37.8 and -40.8 ‰, and δ¹⁸O concentrations of -9.4 and -9.6 ‰ from historical samples from the Byrud deposit.

1.3. Location, access, exposure, and sampling

The Byrud emerald mine is located approximately 60 km north of Oslo, in southern Norway. Fieldwork was carried out at the Byrud mine near the town of Eidsvoll, in the autumn of 2012. Previous fieldwork by Peter Ihlen occurred in the autumn of 2010. Samples were taken from various locations within the mine and its surrounding areas, comprising the various rock types in the region and a number of emerald-bearing pegmatites. The collected material has been used for petrographic and geochemical studies. Sample descriptions, locations and field photographs are presented in Appendix A. Bulk rock geochemistry from samples collected at the Byrud mine are presented in Appendix B. The fieldwork conducted also included detailed mapping of the mine area and individual emerald-bearing veins. The emerald mine is accessible by a main road at Lake Mjøsa (Figure 3-1), with good exposures of monzogranite, pegmatite veins, syenite sills, and black bituminous shale/hornfels. The emerald mine comprising several adits and workings is situated at the bottom of a tree-covered slope adjacent to the main road and approximately 30-50 m from the western shore of Lake Mjøsa. All adits and workings were investigated. Samples of zoned emerald were also collected, in order to determine the emerald formational model, and for comparison to similar colour zoned emerald deposits in Australia, Namibia, and South Africa.

1.4. Regional geology of Southern Norway

The Byrud emerald deposit is located in the northeastern part of a Permian Paleorift structure in the Oslo region. The emerald mineralization at Byrud is related to Permo-Triassic intrusions associated with the evolution of the Oslo Paleorift (Figure 1-2). The tectono-magmatic evolution of the Oslo Paleorift has been thoroughly studied and comprises six evolutionary stages (Ramberg and Larsen, 1978; Larsen and Sundvoll, 1984; Olerud and Ihlen, 1986; Larsen et al., 2008).

The Oslo region is part of an elongated geological province from Langsundsfjord in the south to the northern end of Lake Mjøsa and includes Cambro-Silurian and Late

Carboniferous to Permian rocks. During the Permo-Carboniferous, a fault bounded lithospheric fault zone formed, encompassing the Oslo region and termed the Oslo Rift or Paleorift. This region also includes rift structures in Skagerrak and the Sparagmite region located in the south-eastern part of Norway. The development of the Oslo Paleorift is divided into a series of six stages that evolved over a period of 70 million years, encompassing volcanism, faulting, sedimentation, deep crustal magmatism and thermal metamorphism of the older rocks within the Oslo region. Initially, a vast, shallow, sedimentary basin developed in the Oslo area in front of the Caledonian mountain belt after a period of quiescence in geological activity prior to the end of the Carboniferous. The development of the basin marks the Stage 1 of rifting (Figure 1-2). Late Carboniferous syenitic sills occur throughout the Oslo region. These sills are termed maenites at Byrud. In most areas, Stage 2 constitutes the initiation of the Oslo Paleorift and the first phase of basaltic volcanism. During the Early Permian, the climax of the rift formation marks Stage 3 of the Oslo Paleorift formation. The area is characterised by porphyritic alkaline olivine basaltic lavas containing rhomb-shaped plagioclase phenocrysts. Lava volumes during this stage were at least 10 times greater than in the previous stage (Ramberg, 2008). Stage 3 is marked by major faults and fissure volcanoes, and the rift itself was formed. The first monzonitic batholiths were emplaced during this batholith phase. The faulting during Stage 3 formed a rift valley, similar to the present-day East African Rift Valley (Ramberg, 2008). Most of the graben segments within the rift structure were incorporated in the Oslo Paleorift and bounded on either side by high fault escarpments. During the Middle Permian, massive central volcanoes and calderas formed, marking key geological features during Stage 4 of the Oslo Paleorift. Development of basaltic central volcanoes in different parts of the rift produced prominent structures marked by large faults bounding the grabens. The rhomb porphyries continued to erupt with a decrease in volume and intensity as more central volcanoes gained dominance during this stage. In the early portions of Stage 4, the two large granite batholiths (the Drammen and Finnemarka granites) were emplaced (Figure 1-2). A third batholithic phase marks Stage 5 of the Oslo rifting during the Late Permian with the formation of deep-seated granites, riebeckitic-arfvedsonite granites, syenites and quartz-bearing syenites. No sedimentary or extrusive volcanic rocks are present within the Oslo Graben, likely due to the present erosional level. The magma supply to the Oslo Graben was renewed during Stage 5, with the crystallization of new batholiths

in the southernmost Vestfold Graben, and through the Akershus Graben extending to Skreifjella near Lake Mjøsa (Ramberg, 2008). As a result of chemical processes within the magma, the third batholithic phases are comprised of plutonic rocks, which are syenitic in composition containing quartz and/or riebeckitic-arfvedsonite. It is likely that the previous batholithic phases were derived from fractional crystallization at the base of the crust from mantle-derived alkaline basalts. Once fractionation had reached the stage where the residual buoyant magma surfaced, the magma extruded and crystallized without any assimilation of the country rock (Dons and Larsen, 1978). However, the syenitic and granitic rocks associated with Stage 5 have a more complex crystal fractionation history. It is probable that the ascending monzonitic magma was trapped during ascent and continued to fractionate to form a more evolved magma (Dons and Larsen, 1978). Differences in the characteristics of the country rock based on the gas phase remaining in the magma or escaping, mark differences in the conditions of crystallization (Dons and Larsen, 1978). This led to the different evolutionary trends observed in these syenitic to granitic rocks. Stage 6 marks the final stage of batholith development and the termination of the rift. This period of deep magmatic intrusions is marked by the youngest granites and is referred to as the fourth batholith phase. These intrusions have been dated at 245 million years, although younger ages are recorded in the literature. Younger dykes associated with the latest granites do exist within the Oslo Paleorift and it may be possible that the latest magmatic event is younger than 241 Ma (Ramberg, 2008; Larsen et al., 2008). Detailed regional geology associated with the Byrud mine area is described in Chapter 3.

1.5. Local Geology

Emerald mineralization is proximal to, but post-dates, flat-lying syenitic sills which range from 0.5 m to several meters thick. These sills crosscut and hornfelsed Cambro-Ordovician shale. These sills are one of the earliest syenitic intrusions from the first stage during the development of the Oslo Paleorift. These sills are mainly quartz-rich along the borders, with the quartz primarily occurring as smoky quartz. Commonly, the syenite sills occur within the Cambrian-Ordovician shales, specifically the black shales locally termed the Alum shales. The sills have been dated at 300 to 310 Ma, and were formed during the deposition of the Asker Group (Ramberg, 2008). Locally, the sills have been intruded by small pegmatite veins and veinlets that also crosscut the surrounding black Cambrian shale/hornfels (Figure 1-3). The pegmatites are generally discontinuous and form lenses or small dikes, ranging from a few centimetres to 50 cm thick. They consist of mainly K-feldspar and quartz with an overall alkali syenitic composition. Aplite dykes of similar composition are deemed contemporaneous with the pegmatite. The majority of the better-quality emerald occurs in the northern part of the mine area in small clay-bearing cavities hosted in the pegmatite. Quartz, muscovite, plagioclase, pyrite, pyrrhotite, fluorite, tourmaline, topaz and beryl are the most common pegmatite-associated minerals (Rondeau et al., 2008).

The pegmatite is likely related to a large alkaline granite intrusion located west of Byrud. Previous work has determined that beryl mineralization occurs dominantly in the pegmatite, and rarely as separate crystals in the syenite sills and black shales/hornfelses. It was hypothesized that the vanadium and chromium chromophores, which colour the emerald, were leached from the shales. The carbonaceous black shales and hornfelses contain several percent of amorphous carbon and fine-grained graphite, respectively, and sub-millimetre thick layers rich in Fe-sulphides.

The stratigraphy of the Cambro-Silurian sediments of the Oslo Paleorift has been described by Skjeseth, 1958; Bjørlykke, 1974; and Owen et al., 1990. The shale at Byrud is a black, fine-grained shale with local siltstone and sandstone. Typically, these shales are an argillaceous, often carbonaceous, rock impregnated with alum, originally containing iron sulphides, such as pyrite and marcasite, which, when decomposed forms sulphuric acid. The sulphuric acid reacts with aluminous and potassic materials within

the rock to produce aluminium sulphates. The Cambrian black shales were deposited in a relatively high-energy environment along with basal conglomerates and carbonate beds. This time period marked a period of transgression which covered the majority of the Baltic shield, and previous literature suggests shallower conditions prevailed after this transgression (Bkørlykke, 1974). The black shales were deposited in shallow water, and the more 'Alum-rich' shales were deposited in a moderately oxidizing environment. After deposition the environment was typically reduced, with an excess of H₂S and complete decomposition of any organic material (Skjeseth, 1958; Nyland and Teigland, 1984).

At the Byrud mine, most of the host rocks comprise the black shale and hornfelsed equivalent (Figure 1-4). The dominant basement rocks are weakly deformed gray monzodiorite-granodiorite (~1600 Ma) and sheared equivalents (Loughrey et al., 2013). In the study area it intrudes light-gray fine-grained gneissic meta-volcanic rocks.

Emerald in the pegmatite and associated aplite dykes are often embedded in feldspar, quartz, muscovite, pyrrhotite and in fluorite. From previous studies, the crystals occur up to 6 cm in length and 2 cm wide and form hexagonally shaped crystals with flat basal terminations; minor pyramidal faces have also been observed on the terminations of the Byrud emerald (Nordrum et al., 2006; Rondeau et al., 2008). The emerald colour is variable, from translucent and transparent green, bluish green to colourless, with grayish yellow beryl not uncommon. Some crystals have lighter cores, with topaz rarely present in the core. Many small gem-quality emerald crystals free of flaws and lighter in colour have been identified. Additionally, some emerald exhibit alternating colour zones parallel to the basal plane, varying from colourless beryl to deep green emerald.

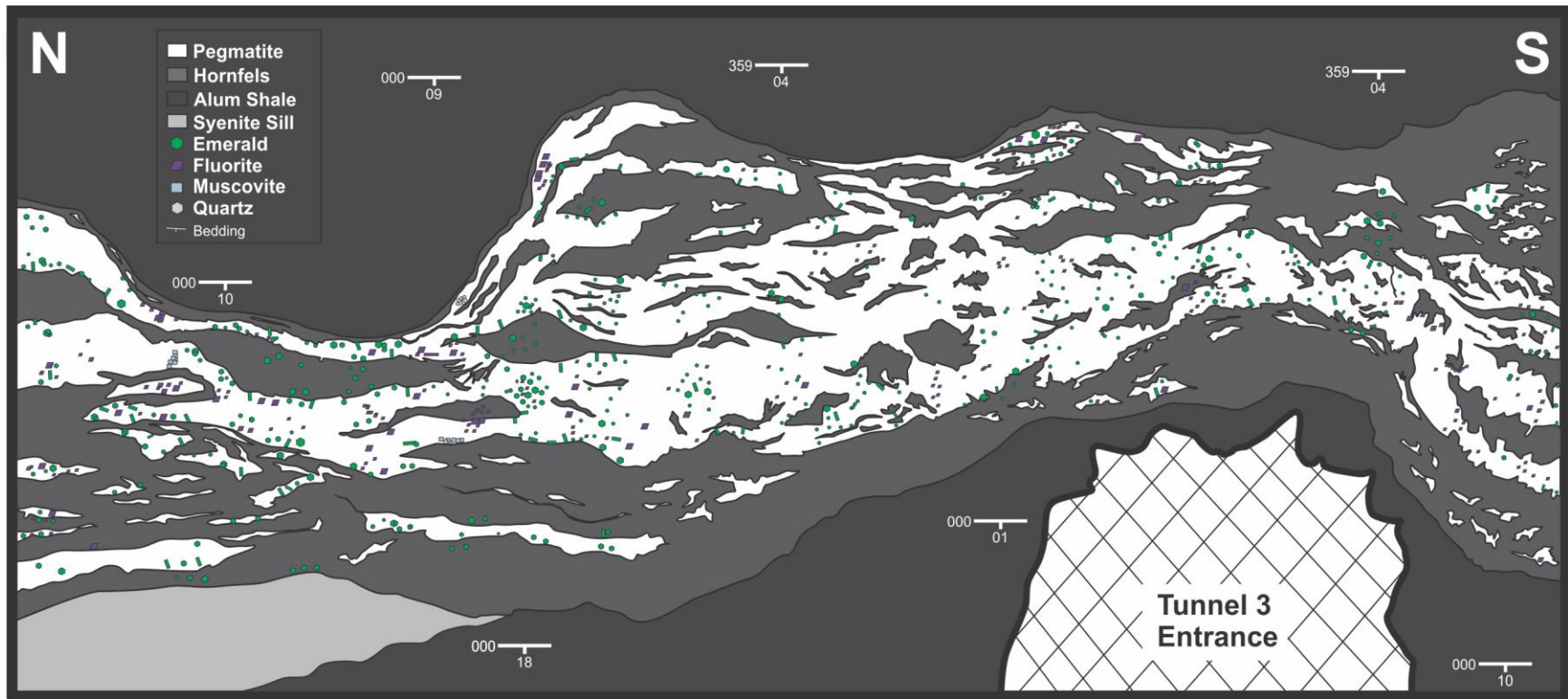


Figure 1-3. Idealized vein cross-section of mineralized pegmatite intruding the host rock comprising of black shales. Emerald mineralization occurs within the pegmatite veins and on the edge of the veins with the surrounding host rock.

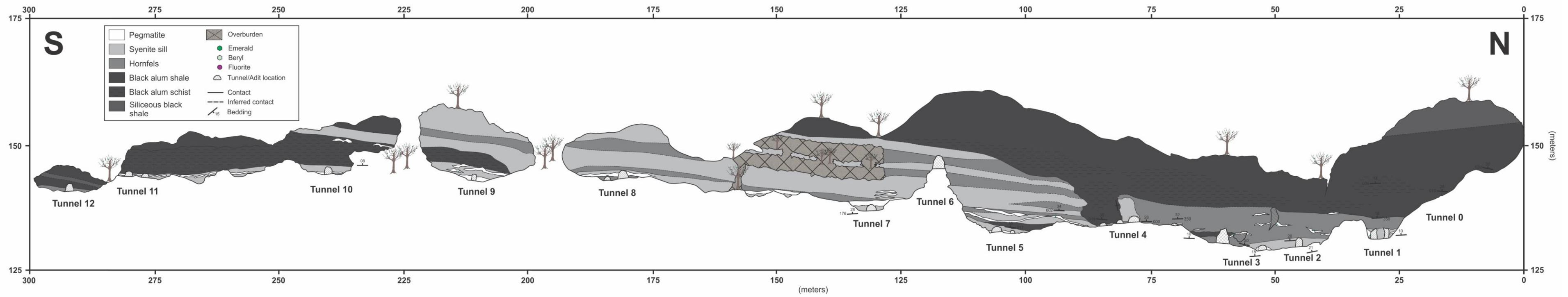


Figure 1-4. Idealized cross section across the Byrud mine showing structural and lithological relationships between rock units and location of tunnels and adits accessible at the deposit.

References

- Bjørlykke, K. (1974). Depositional History and Geochemical Composition of Lower Palaeozoic Epicontinental Sediments from the Oslo Region. *Norges geologiske underøkelse, Bulletin* **24**: 1-88.
- Cheilletz, A., and Giuliani, G. (1996). The genesis of Colombian emeralds: A restatement. *Mineralium Deposita*, **31**: 359-364.
- Dons, J.A., and Larsen, B.T. (Eds.) (1978). The Oslo Paleorift. A Review and Guide to Excursions, pp. 199. *Norges Geol. Unders.*, 337.
- Groat, L., Giuliani, G., Marshall, D., and Turner, D. (2008). Emerald deposits and occurrences: a review. *Ore Geology Reviews*, **34**: 87–112.
- Groat, L.A., Giuliani, G., Marshall, D., and Turner, D. (2007). Chapter 3: Emerald. In *Geology of Gem Deposits, Short Course 37*. Edited by L.A. Groat. Mineralogical Association of Canada, Yellowknife, Northwest Territories, 79-109.
- Giuliani, G., France-Lanord, P., Coget, D., Schwarz, A., Cheilletz, Y., Branquet, D., Giard, A., Martin-Izard, P., Alexandrov, P., and Piat, D.H. (1998). Oxygen isotope systematic of emerald: relevance of its origin and geological significance. *Mineralium Deposita*, **31**: 513–9.
- Giuliani, G., Cheilletz, A., Arboleda, C., Carrillo, V., Rueda, F., and Baker, J.H. (1995). An evaporitic origin of the parent brines of Colombian emeralds: fluid inclusion and sulphur isotopic evidence. *European Journal of Mineralogy*, **7**: 151–65.
- Goldschmidt, V.M., (1911). Die Kontaktmetamorphose im Kristianiagebiet. *Videnskapselskapets Skrifter, I. Mat-naturv. Klasse*, **1**: 56 and 357-358.
- Grundmann, G., and Morteani G., (1989). Emerald mineralization during regional metamorphism; the Habachtal (Austria) and Leydsdorp (Transvaal, South Africa) deposits, *Economic Geology*, **84**: 1835-1849.
- Hammarstrom, J.M. (1989). Mineral chemistry of emeralds and associated minerals from Pakistan and Afghanistan: an electron microprobe study. *In Emeralds of Pakistan: Geology, Gemology and Genesis* (A.H. Kazmi & L.W. Snee, eds.), pp.125-150. Van Nostrand Reinhold Company, New York, N.Y.
- Hewton, M. (2012). Investigation of the Mountain River beryl (emerald variety) occurrence, Mackenzie Mountains, Northwest Territories. pp.139. MSc Thesis. Simon Fraser University, Burnaby, Canada.
- Kazmi, A.H., and Snee, L.W. (1989). Geology of the world emerald deposits: a brief review. In: *Emeralds of Pakistan* (eds Kazmi AH, Snee LW), pp. 165–228. Van Nostrand Reinhold, New York, NY.

- Larsen, B.T., Olausson, S., Sundvoll, B., and Heeremans M. (2008). The Permo-Carboniferous Oslo Rift through six stages and 65 million years. *Episodes*, **31**: 52–58.
- Larsen, B.T., and Sundvoll, B. (1984). The Oslo Graben: A Passive High Volcanicity Continental Rift. *EOS Transactions*, **65**: 1084.
- Loughrey, L., Marshall, D., Jones, P., Millsted, P., and Main, A. (2012). Pressure-temperature-fluid constraints for the Emmaville-Torrington emerald deposit, New South Wales, Australia: fluid inclusion and stable isotope studies. *Central European Journal of Earth Sciences*, **4**: 287–99.
- Loughrey, L., Marshall D., Ihlen P., and Jones P. (2013). Boiling as a mechanism for colour zonations observed at the Byrud emerald deposit, Eidsvoll, Norway: fluid inclusion, stable isotope and Ar–Ar studies. *Geofluids*, **13**: 542-558.
- Nordrum, F.S., and Raade, G. (2006). Das Smaragd-Vorkommen von Byrud (Eidsvoll) in S€ud-Norwegen [The emerald deposit at Byrud (Eidsvoll) in South Norway]. *Mineralien-Welt*, **17**: 52–64 [in German].
- Nyland, B., and Teigland, J. (1984). Sedimentologisk og geokjemisk undersøkelse av de kambriske og underordoviciske marine sedimenter i Oslofeltet. Thesis for cand. Real, pp. 196. Geologisk institutt, Universitetet i Oslo.
- Olerud, S., and Ihlen, P. (1986). Metallogeny associated with the Oslo paleorift. *Sveriges Geologiska Undersökning, Serie Ca: Avhandlingar och Uppsatser I A4*, **59**: 1–17.
- Ottaway, T.L., Wicks, F.J., Bryndzia, L.T., Keyser, T.K., and Spooner, E.T.C. (1994). Formation of the Muzo hydrothermal emerald deposit in Colombia. *Nature*, **369**: 552–4.
- Owen, A.W., Bruton, D.L., Bockelie, J.F., and Bockelie, T.G. (1990). The Ordovician succession of the Oslo region. *NGU Special Publication 4*: 54.
- Ramberg, I.B., Bryhni, I., Nottvedt, A., and Ragnes, K. (2008). The Making of a Land-The Geology of Norway, pp. 624. Geological Society of Norway.
- Ramberg, I.B., and Larsen, B.T. (1978). Tectonomagmatic evolution, In: *The Oslo Paleorift*. (eds Dons JA, Larsen BT), *Norges Geologiske Undersøkelse*, **337**: 55–73.
- Rondeau, B., Fritsch, E., Peucat, J.J., Nordrum, F.S., and Groat, L. (2008). Characterization of Emeralds from a historical deposit: Byrud (Eidsvoll), Norway. *Gems & Gemology*, **44**: 108–22.
- Rudnick, R.L., and Gao, S. (2003). The composition of the continental crust. *In The Crust* (R.L. Rudnick, ed.). *Treatise Geochem*, **3**: 1-64.
- Schwarz, D., Giuliani, G., Grundmann, G., and Glas, M. (2002). The origin of emerald...a controversial topic. *ExtraLapis English*, **2**: 18-21.

- Schwarz, D., and Giuliani, G. (2001). Emerald deposits – A review. *The Australian Gemmologist*, **21**: 17–23.
- Schwarz, D., Giuliani, G., Grundmann, G., and Glas, M. (2001). Die Entstehung der Smaragde, ein vieldiskutiertes Thema, ExtraLapis. In: Smaragd, der Kostbarste Beryll, der Teuerste Edelstein (eds Schwarz D, Hochleitner R), 21, pp. 68–73. ExtraLapis, Munich, Germany.
- Schwarz, D. (1991). Die chemischen Eigenschaften der Smaragde; II, Australien und Norwegen. *Zeitschrift der Deutschen Gemmologischen Gesellschaft*, **40**: 39–66.
- Skjeseth, S. (1958). Uran i kambrisk alunskifer i Oslofeltet og tilgrensende områder, NGU bulletin. **203**: 100-111.
- Ventalon, S., Dubois, M., Rondeau, B., and Régnier, S. (2009). Mineralising fluid properties of the emerald deposit of Byrud, Norway. *European Current Research on Fluid Inclusions (ECROFI XX)*, Granada, Spain, 273-274.
- Websky, H.J. (1976). Mineral-Fundstellen, Band 4, Skandinavien. Chr. Weise Verlag, München, 117-118.
- Zwaan, J.C., Seifert, A.V., Vrana, S., Laurs, B.M., Anckar, B., Simmons, W.B., and ... Garcia-Guillerminet, H. (2005). Emeralds from the Kafubu area, Zambia. *Gems and Gemology*, **41**: 116-148.

2. Petrography

2.1. Host rocks and alteration

The host rocks to emerald veins at the Byrud mine consist of unaltered black shales to metamorphosed black shales, syenite sills and syeno-granitic pegmatite and aplite veins. The contact metamorphism caused by the intrusion of the granitic rocks has transformed the black shales into biotite hornfelses locally. The flat-lying black shales became strongly imbricated during the Caledonian orogeny, and display characteristic metamorphic textures in thin section. The majority of the sills are rusty due to weathering of Fe-sulphides, mainly pyrrhotite, in the overlying Cambrian-Early Ordovician hornfelsed black shales. The sedimentary host rocks are well layered and the syenite sills roughly parallel bedding. The sills and later emerald-bearing pegmatite/aplite veins follow a north-south strike similar to that of the black shales. Within the mine adits, many of the sulphides have oxidised, precipitating sulphatic minerals such as jarosite and gypsum. A detailed description of the host rocks from samples gathered from the mine adits and surrounding outcrops at the Byrud mine are described below, shown in Figure 2-1, and accompanying rock descriptions are in Appendix A.

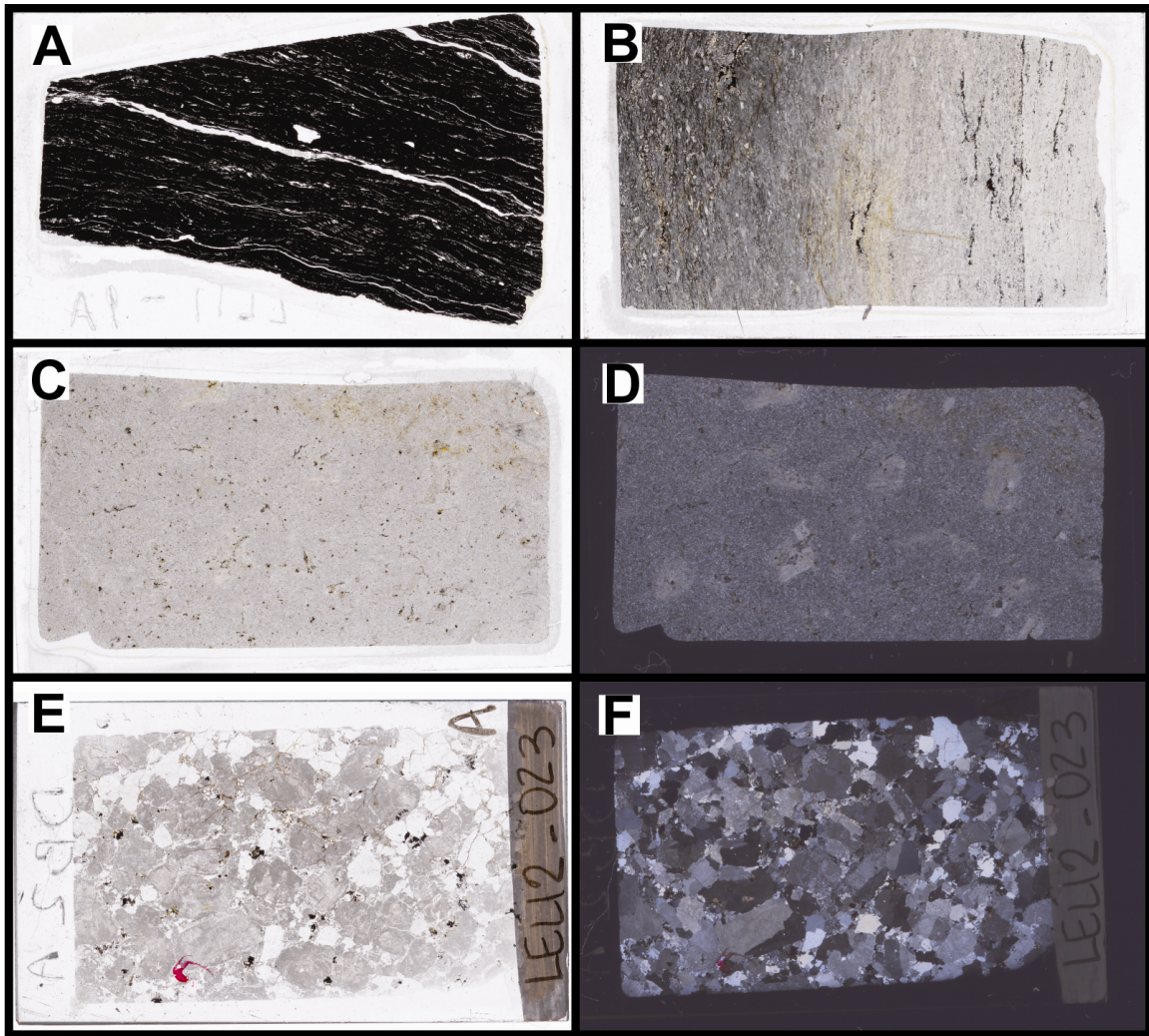


Figure 2-1. Scanned thin sections of host rocks to the emerald veins. Samples A) LL11-1A, black to dark gray shale, siltstone and fine-grained sandstone interbeds. B) LL11-2B-2, metamorphosed black shale – biotite hornfels near emerald-bearing pegmatite veins displaying a visible grain size reduction with fine-grained quartz as the dominant alteration in thin section. C) LL11-4A-2, syenite sill with visible phenocrysts observed in cross-polarized transmitted light in D). E) LEL12-023, coarse-grained monzogranite, dark opaques consists of pyrite and pyrrhotite. F) corresponding photomicrograph of LEL12-023 taken in cross-polarized transmitted light.

2.1.1. Unaltered bituminous black shale

The black shale contains fine-grained carbonaceous material, fine-grained graphite, clay and other minerals. The fine-grained nature of the shaley layers precludes distinguishing individual mineral grains. The clay in these black shales is interpreted as illite. Small scattered pyrite cubes and anhedral pyrrhotite are observed in thin section. Bedding is easily distinguishable by finely laminated layers (Figure 2-1). Lighter coloured fine-grained layers are quartz and feldspar rich. Darker coloured finer-grained interlayers are likely comprised of a dark gray shale, siltstone and fine-grained sandstone. Thin seams or lenses of organic material, including graphite are characteristic.

2.1.2. Metamorphosed black shale –biotite hornfels

The fine-grained metamorphosed black shale displays banding due to relict bedding. The hornfelsed rock is regarded as a biotite hornfels due to the presence of biotite porphyroblasts and fine-grained crystals of biotite and muscovite. Andalusite porphyroblasts are common in thin section surrounded by a fine-grained groundmass. Many of these porphyroblasts show two cleavages at right angles to one another. Inclusions are more abundant in the centres and radiate towards the corners of the crystals. The cruciform pattern is common in the chiastolite (andalusite) porphyroblasts. The chiastolite is altered to fine-grained muscovite locally (Figure 2-2). The majority of biotite and andalusite porphyroblasts, ranging up to 15% of the rock, are concentrated along fine-grained clay-rich layers. Quartz and minor feldspar are present up to 60%. Quartz, feldspar, muscovite, and occasional biotite occur as inclusions. Fe-oxides are present as an alteration product of the sulphides. Carbonaceous clay and minor graphitic rounded or elliptical areas are common up to 20%. Other areas are enriched in biotite (and/or muscovite) and coarser-grained quartz which occur along bands/lenses of sulphides. Biotite is locally altered to chlorite. Minor amphibole is replaced by biotite. Other accessory minerals include apatite and rutile. Pyrite and pyrrhotite, up to 5%, occur as the major sulphides with minor Fe-oxide alteration.

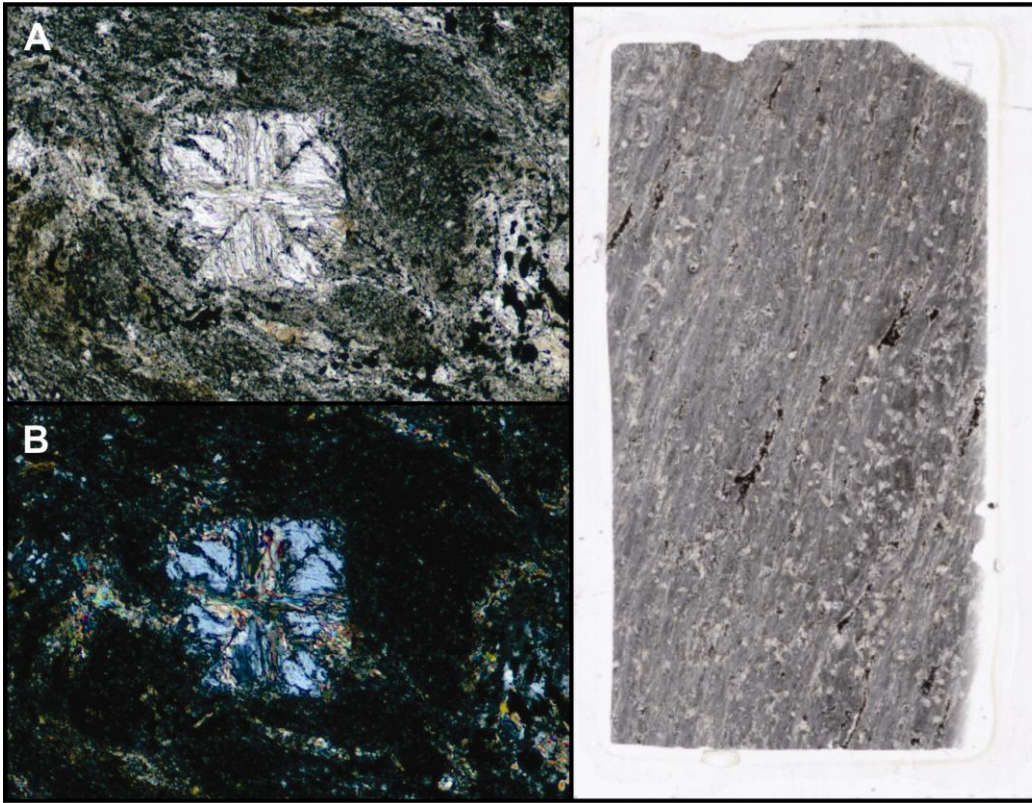


Figure 2-2. Biotite hornfels displaying laminated bands and lenses of sulphides. Typical chiastolite porphyroblasts are altered to fine-grained muscovite locally. Images are taken in A) plane polarised transmitted light. B) cross-polarized transmitted light. Field of view is approximately 0.98 mm. C) Scanned thin section of LL11-2A-1 taken in plane polarized light.

The contact metamorphosed black shale near the emerald-bearing pegmatite veins have a composition similar to the biotite hornfels. However, pervasive silica flooding or silicification is observed in these samples. Grain size reduction is prominent with fine-grained quartz as the dominant alteration in thin section. Alteration in hand sample is bleached, gray and cherty in contrast to its unaltered equivalent. Coarser-grained quartz, muscovite and minor biotite occurs along bands/lenses of sulphides, similar to the non-silicified hornfels. Sulphides and other accessory minerals present are the same as in the non-silicified hornfels.

2.1.3. Syenite sill

Quartz and feldspar phenocryst abundance rarely varies across a given sill but commonly varies within small distances between different sills. Both porphyritic and aphyric types are present in the mine area at Byrud. Locally, the syenite sills display chilled margins and are bounded by thin layers of hornfelsed shales. A darker coloured, feldspar-phyric phase occurs in the thicker sills, the slightly paler silicified aphyric sills are similar to the silicified biotite hornfels, thus, complicating field observations. The syenite sills are generally light gray to light pinkish gray on fresh surfaces and relatively coarser grained than the hornfels. Typically, the sills contain mm-scale feldspar distinguishing it from the hornfels. Along major joints and veins, the syenite sills have bleached areas, making it similar to the hornfels. In these areas the primary mineralogy has been altered to a secondary assemblage primarily comprising of quartz, chlorite, carbonate and low albite. Locally, the sills resemble quartzitic hornfels but are likely supergene altered, or bleached by acid sulphate waters.

Approximately 40% of the sills comprise zoned plagioclase and 55% K-feldspar, approximately 5% quartz, and minor micas, amphiboles, carbonate, zircon, rutile, muscovite, fluorite, chlorite, and apatite. Chlorite occurs as an alteration product of amphiboles and biotite. Sericite and carbonate occur as an alteration of feldspars. In some thin sections, the sills display an equigranular texture with minor sericitization of feldspar laths. Interstitial chlorite, carbonate and minor biotite occur together with minor altered opaque oxides. The opaques are dominantly pyrite, pyrrhotite, and chalcopyrite. Additionally, ilmenite, titanomagnetite, Fe-oxides and Mn-Ti-oxides are observed as alteration of some sulphides. A vanadium-rich rutile has been observed from electron dispersive analyses (EDS). These rutile crystals are rare in the sills and occur more commonly in the pegmatite, granite and black shale host to the emerald-bearing pegmatite.

All the mine openings with the exception of the most southern tunnel (#6) are in the lower syenite sill which is 1-2 meters thick. Along strike to the south of the northernmost openings, the syenite sill splits into several parallel sills ranging up to 1 m in thickness (Figure 1-5). An undulating or wavy strike in the layering of the hornfels rimming the thicker (2-4 meter) sill is also observed locally.

2.1.4. Granitic rocks

The monzogranite at the Byrud mine and surrounding areas is primarily composed of both sodic and potassic feldspar with quartz. The quartz is recognized by the lack of alteration and interference colours. Both perthitic and microperthitic textures are identified under cross polars in the majority of feldspar crystals (Figure 2-3A). Intergrowths of quartz and alkali feldspar are common displaying granophyric to micrographic textures (Figure 2-3B). Much of the potassic feldspar does not show microcline-type twinning, with only a few crystals displaying vague cross-hatched twins. Most of the feldspar crystals are altered to saussurite and few areas display pervasive sericitization. Minor calcitic alteration is present in the samples from Byrud. Amphibole is interstitial to large quartz and feldspar crystals, and is associated with the few sulphides present. Biotite and chlorite alter the amphibole. Zircon, ilmenite, rutile, titanite, apatite and minor fluorite are also observed as accessory minerals in thin section. Samples collected from the mine display pervasive biotite alteration of all amphibole, with minor chloritization of the biotites. Sulphides present include minor pyrite, pyrrhotite, chalcopyrite, with Fe-oxides altering pyrite.

Near the Byrud mine are amazonite-bearing granites. In hand sample, the amazonite is green in colour and displays perfect cleavage. Perthitic intergrowths are evident in thin section with some alteration to sericite. Fine-grained plagioclase laths are common in areas of the thin section. The granites in this area are compositionally similar to the granite present at the Byrud deposit. Chalcopyrite, pyrite, sphalerite and molybdenite are present in thin section. These granitic plutons in this region commonly have associated skarn deposits of Fe, Cu, Zn, Pb and/or Bi formed during the same stage of beryl mineralization at Byrud (Ihlen, 1978).

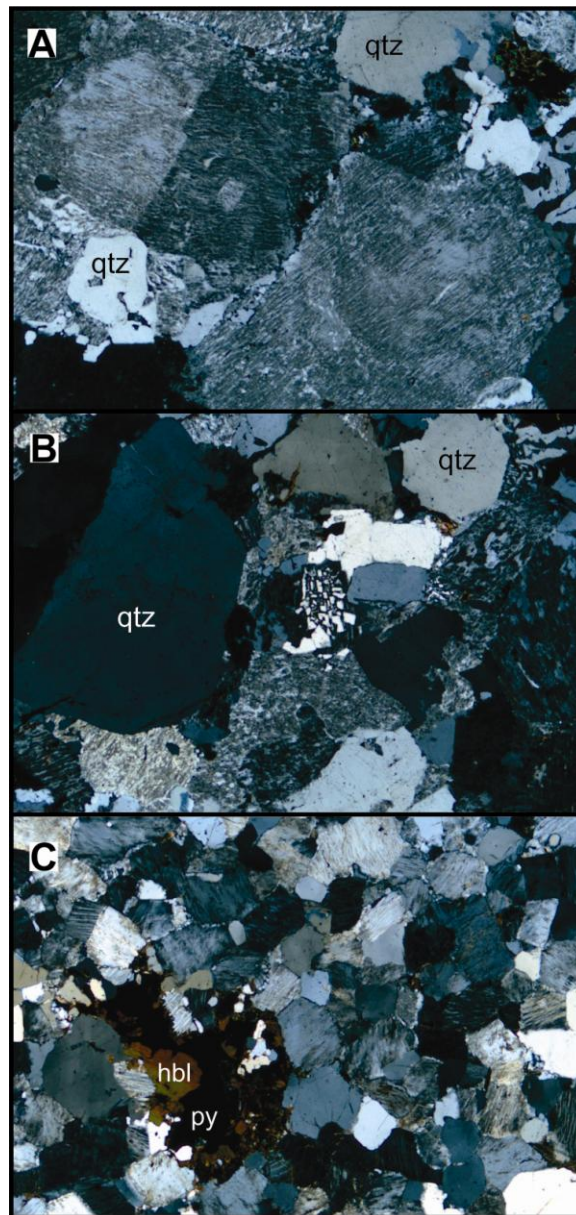


Figure 2-3. Monzogranite in thin section: A) perthitic texture displayed by fine intergrowths of potassium-rich feldspar and sodium-rich feldspar, sample LEL12-023; B) granophyric texture displayed by intergrowths of quartz (qtz) and alkali feldspar arranged around quartz and anhedral K-feldspar crystals, LEL12-023; C) finer-grained equivalent of the granite, displaying microperthitic textures in the feldspars, with quartz, hornblende (hbl), biotite and opaques (py-pyrite), sample LL11-4C-1. All images taken in cross-polarized transmitted light. Field of view is 4 mm.

2.2. Veins

At Byrud the veins consist of pegmatitic to aplite veins and dykes, varying in thickness from a few millimeters up to 1 m thick, as well as quartz and quartz-muscovite veins. Beryl and emerald occur in varying amounts in all the vein types. Beryl colour is variable and grains range up to 1 cm. These quartz-bearing alkali syenite pegmatitic veins also have beryl locally within miarolitic cavities. The major vein constituents at the Byrud deposit are fine to coarse grained quartz, K-feldspar, albite, and muscovite. Quartz occurs as clear quartz crystals, to smoky and milky white in hand sample. Generally, massive, subhedral to euhedral crystals are common in thin section, and rare prismatic crystals with pyramidal terminations have been found at the Byrud deposit. In thin section quartz occurs as both monocrystalline and polycrystalline quartz, with locally sutured boundaries. Minor quartz veinlets extend into the wallrock. Muscovite in the veins commonly occurs with quartz. Quartz is the dominant vein mineral with muscovite locally constituting up to 10% of the veins. The feldspars in thin section occur both as subhedral to euhedral crystals that are commonly replaced by micas and clays. The feldspar consists of 60% K-feldspar and 40% plagioclase. Finer-grained feldspar is also common within the pegmatite veins. Minor deformation features are observed in the plagioclase crystals and some crystals are zoned. Minor graphic textures are observed between quartz and feldspar crystals with few microperthitic textures. Within beryl-poor veins, albite content increases and is dominated by fine plagioclase laths. Similar textures occur as secondary veinlets within the mineralized pegmatitic veins. A lateral variation in grain size occurs towards the contact with the wallrock. Accessory minerals including beryl and emerald comprise the remaining vein minerals. Beryl and topaz are common at the contact between the veins and the host rock, and within the veins (Figure 2-4A). Fluorite has been observed in most of the vein samples and occurs with quartz, feldspar and beryl. It forms subhedral to anhedral crystals and as dark lilac disseminations (Figure 2-5). Fluorite commonly occurs interstitial to beryl and is associated with spherical or radiating muscovite (Figure 2-5). Topaz is commonly colourless to yellow and embedded in quartz and plagioclase within some of the pegmatite veins. Small apatite crystals are present with euhedral to subhedral zircon. Trace vesuvianite was also detected via EDS analyses. Tiny, dark gray to black grains occur as inclusions in feldspar and quartz. Most appear to be a tantalian and niobian

rutile which was also confirmed by EDS. Also, V-rich TiO₂, possibly rutile grains were also detected. Other accessory minerals include scheelite and ilmenite. Sulphides observed in the veins comprise of pyrite, pyrrhotite, and rarely molybdenite. Additionally, minor quartz-muscovite veinlets crosscut larger beryl and feldspar crystals and are locally associated with fluorite.

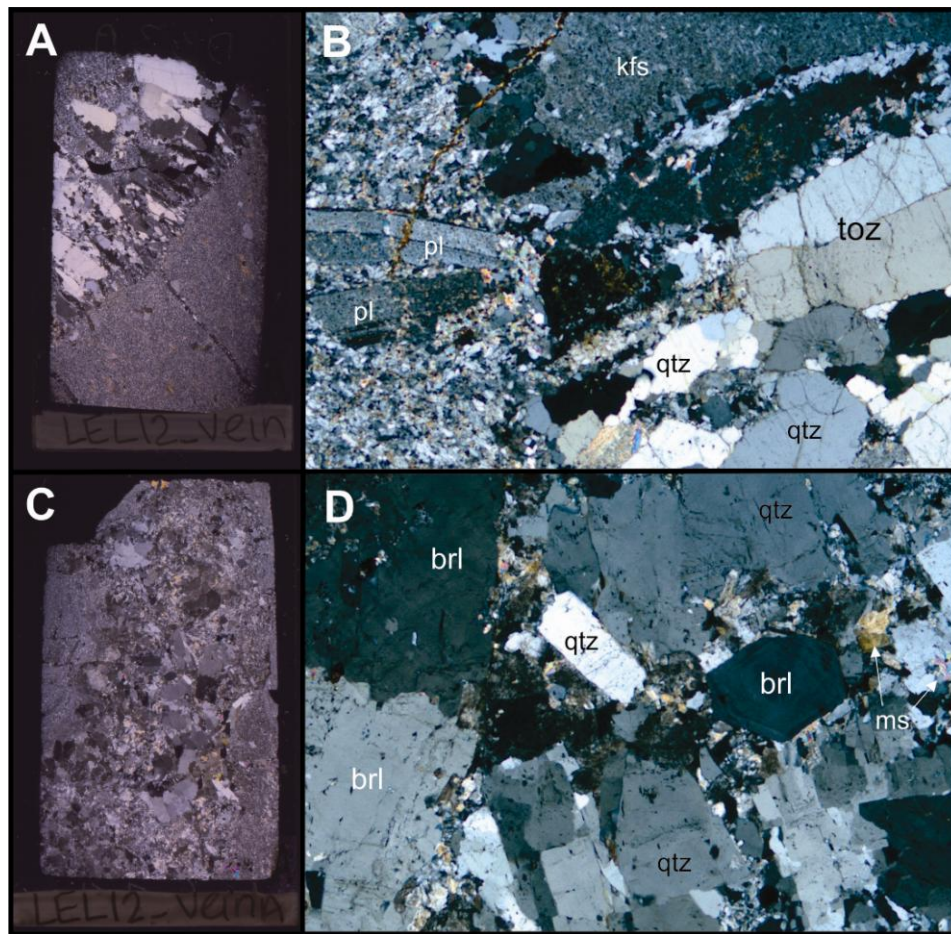


Figure 2-4. Pegmatite veins in thin section: A) scanned thin section of LEL12-vein B) same sample as A) contact between coarser grained pegmatite vein and finer grained host rock. The pegmatite contains K-feldspar (kfs), plagioclase (pl), quartz (qtz) and topaz (toz) with fine-grained muscovite as the fine-grained high birefractant minerals; C) scanned thin section of LEL12-veinA; D) euhedral beryl (brl) to massive beryl (brl) within pegmatite veins. Images in cross-polarized transmitted light. Field of view for the photomicrographs is 4 mm.

Emerald mineralization is often associated with feldspar, quartz, topaz, muscovite, pyrrhotite and fluorite. The crystals observed from the study area display hexagonal crystals with the largest crystal being 0.8 cm wide and less than 1 cm in length. A wide range of colours from translucent and transparent green, bluish green and colourless beryl were observed in the samples. Some of the crystals have a lighter core, primarily comprised of colourless beryl and minor topaz. Many of the studied emerald crystals display alternating growth zones parallel and perpendicular to the *c* axis of the beryl structure. These growth zones vary from colourless beryl to deep emerald green. Descriptions of these colour zones are presented in Chapters 3 and 4. Colourless beryl is also present at the mine, occurring as hexagonal crystals up to 1.5 cm in length. In thin section, beryl occurs as massive intergrown crystals to individual euhedral crystals (Figure 2-4B), and rarely as intergrown needles. There are up to 45 minerals recorded at the Byrud emerald deposit with albite, apatite, calcite, fluorite, beryl, muscovite, orthoclase, pyrite, quartz, rutile, and topaz as the most common. A full list of minerals at Byrud mine can be found in Nordrum and Raade (2006).

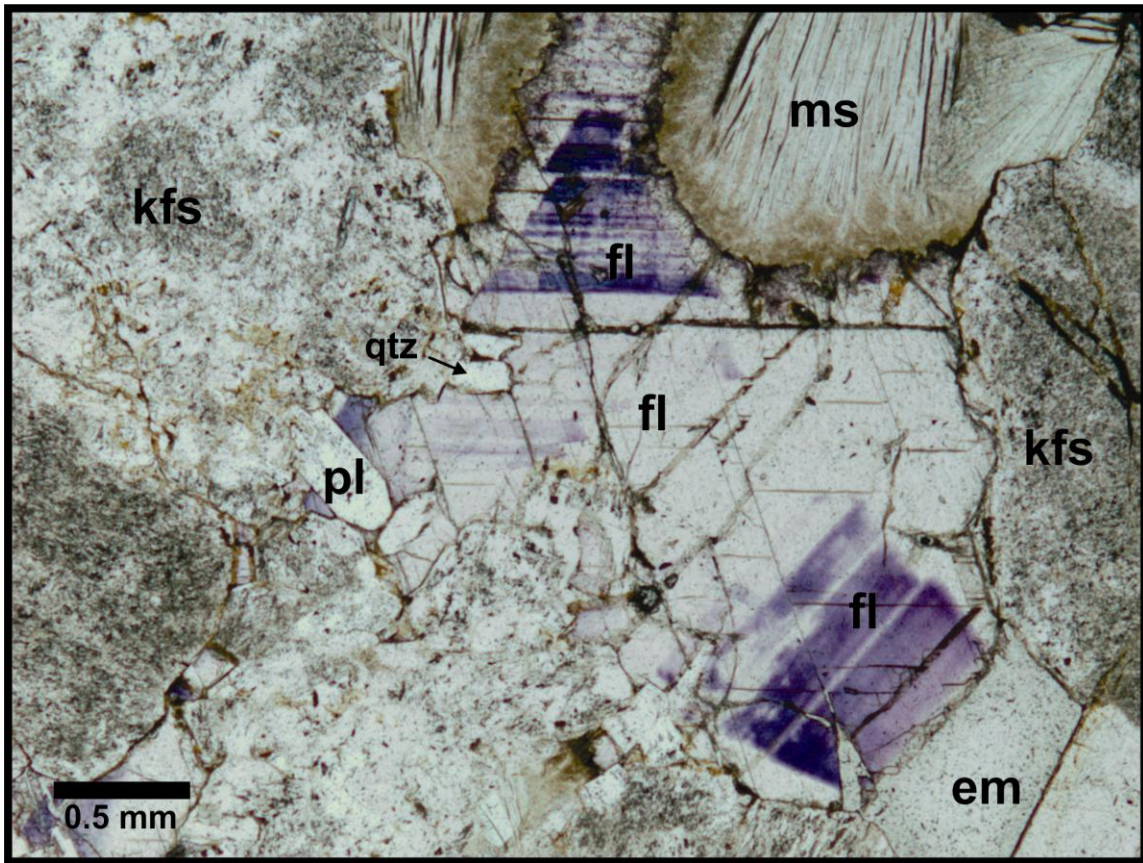


Figure 2-5. Photomicrograph of emerald-bearing pegmatite primarily composed of highly altered potassium feldspar (kfs), muscovite (ms), quartz (qtz) and plagioclase (pl). Fluorite (fl) is present and occurs with emerald (em) in the pegmatites. The fluorite is easily identifiable by its isotropic character, cleavage and purple zonations. Sample number: LL11-05C. Photo taken in plane polarized light.

Veins dominated by fluorite, chlorite, sphalerite and free of emerald also occur within the Byrud study area. Fluorite is the most common mineral in these veins and locally occurs with radial or spherical chlorite (Figure 2-6). Calcite is minor and occurs as the dominant carbonate mineral with minor Fe-carbonate. Muscovite is minor and is associated with quartz and feldspar. Sphalerite, chalcopyrite, pyrrhotite and pyrite are the main sulphides. Clay alteration of the feldspars is pervasive with selective sericitization occurring throughout the samples.

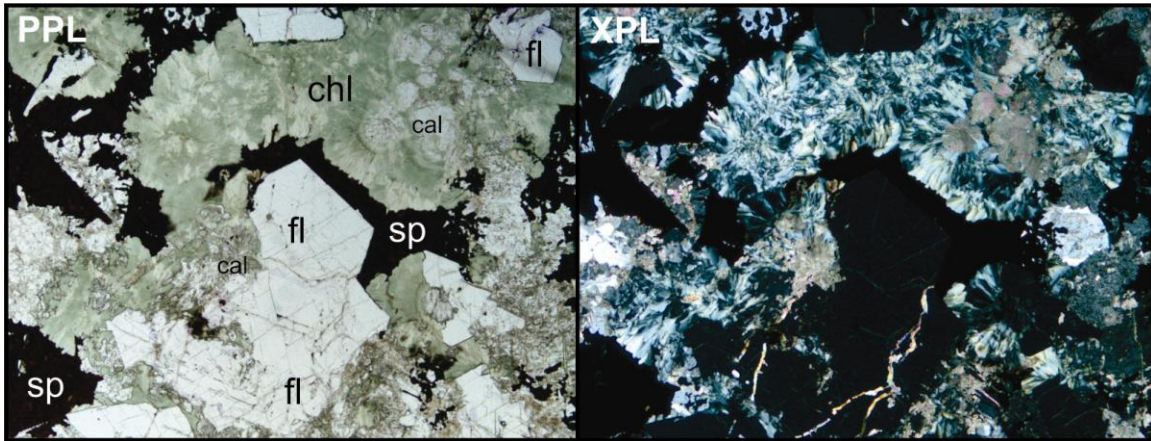


Figure 2-6. Photomicrographs of sample LEL12-FIB, a beryl-free vein in plane-polarized transmitted light (PPL) and cross-polarized transmitted light (XPL) displaying sphalerite (sp), fluorite (fl), chlorite (chl) and late stage calcite (cal) alteration. Field of view is approximately 4 mm.

2.3. Summary and discussion

The paragenetic sequence of the veins and alteration indicates two stages of hydrothermal fluid activity (Figure 2-7). Through petrographic observations, mineralization of an initial fluorite-chlorite-sulphide assemblage within localized cavities and veins occurred early in the sequence. Chlorite and sphalerite within beryl-free quartz and pegmatite veins precipitated first, followed by fluorite. Muscovite is associated with fluorite in the majority of these veins and is contemporaneous with this stage of fluorite mineralization. Minor rutile and apatite precipitated near the end of stage I. Feldspar precipitation began late in stage I, and continued in association with beryl crystallization. Albite with minor K-feldspar continued to precipitate late into stage II, as some beryl crystals show irregular crystal boundaries with feldspar. Sulphide mineralization specifically pyrite and pyrrhotite occurs as disseminations and as anhedral crystals within feldspar and quartz. Sulphide mineralization likely occurred late in stage I and early into stage 2. Antun (1967) and Bkørlykke (1974) observed the pyrrhotite as a secondary alteration of pyrite in the contact metamorphic aureole associated with the

igneous intrusion to the west; however, it was not determined whether the pyrrhotite occurs as an alteration in this study. Quartz precipitation began in stage II, and continued to the end of vein mineralization. Topaz, rutile, ilmenite, apatite and other accessory minerals precipitated during this stage of mineralization. Recrystallization of quartz occurred with muscovite in fractures and cuts fluorite, beryl, and post-dates vein mineralization. Calcite occurred as a replacement mineral or as infill in late-stage fractures. Albite precipitation continued late in stage II as inclusions of plagioclase are found within larger K-feldspar crystals. Clay alteration of the feldspars post-dates mineralization.

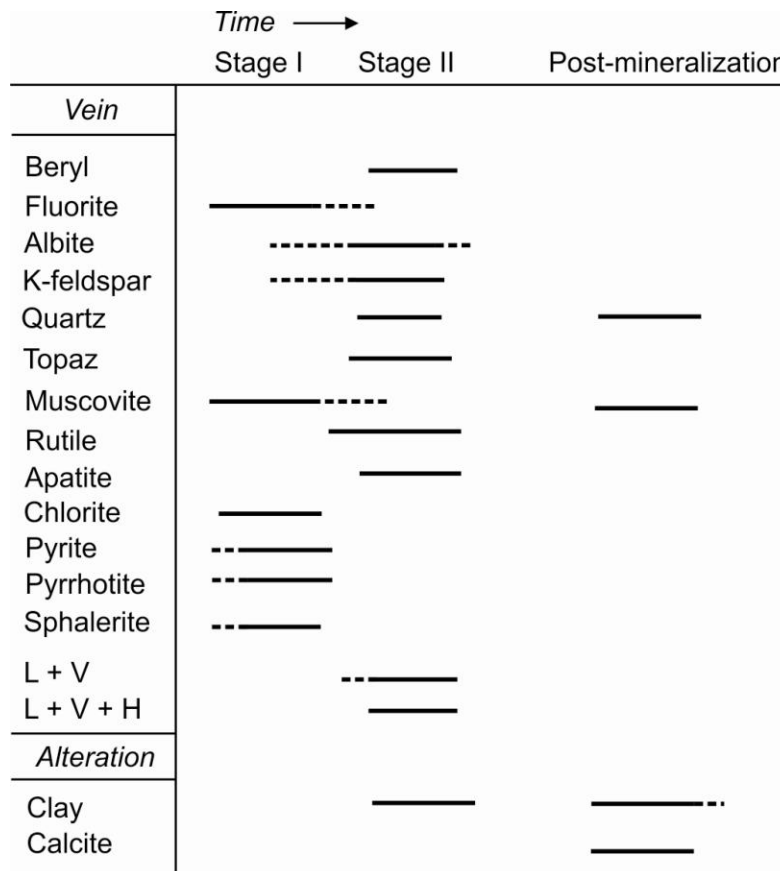


Figure 2-7. Paragenetic sequence of vein and alteration minerals, in addition to fluid inclusion populations of liquid + vapour (L + V) and liquid + vapour + halite (L + V + H). Fluid inclusion descriptions supplied in Chapter 3.

Fluids involved in beryl mineralization were sourced from the granitic rocks with varying degrees of interaction with the black shales leaching and mobilizing elements from the host rocks. Bulk rock geochemical analyses of the unaltered black shales show they are highly enriched in V and somewhat enriched in Cr, compared to normal continental crust, greywacke, and shale (Appendix B; Lentz, 2003). These shales have high carbon contents, with elevated Ba, Cs, Cu, Mo, Pb, Rb, U, V and Cr enrichment relative to typical shales. Therefore, the most likely source of the chromophoric elements for emerald mineralization is deemed to be from the shales with beryllium supplied by the plutons and via the fluid phase. Evidence for the source of these chromophoric elements are discussed in Chapter 3.

The emerald and beryl at the Byrud deposit display colour zonations which indicate differing fluid conditions during emerald and colourless beryl precipitation. Within the stage II mineralizing event, the fluid involved in the partitioning of V and Cr from the host rocks is related to a two-phase boiling system. Details on the crystal chemistry of emerald and its formation of the zonations are given in Chapters 3 and 4. As observed in other emerald localities, the increase in albite content indicates changes in fluid chemistry and vein conditions free of beryl mineralization (Turner and Groat, 2007). Decreases in Be content at the edge of a mineralizing system results in the stable aluminous phase being albite. When Be became more abundant in the mineralizing system, it interacted with the V and Cr supplied by the host rocks precipitating as emerald. As vein crystallization progressed, decreasing Be contents again reflected the precipitation of albite as interpreted from petrographic observations.

References

- Antun, P. (1967). Sedimentary pyrite and its metamorphism in the Oslo Region. *Norsk geol. Tidsskr.* **47**: 221-235
- Bjørlykke, K. (1974). Depositional History and Geochemical Composition of Lower Palaeozoic Epicontinental Sediments from the Oslo Region. *Norges geologiske underøkelse, Bulletin* **24**: 1-88.
- Ihlen, P.M. (1978). Ore deposits in the north-eastern part of the Oslo region and in the adjacent Precambrian areas. *NATO Advanced Study Institutes Series. Series C: Mathematical and Physical Sciences.* **36**: 277–86.
- Lentz, D.R. (2003). Geochemistry of sediments and sedimentary rocks: historical to research perspectives. In *Inorganic Geochemistry of Sediments and Sedimentary Rocks: Evolutionary Considerations to Mineral Deposit-Forming Environments*. Edited by D.R. Lentz. Geological Association of Canada, *GeoText* **4**: 1-6.
- Nordrum, F.S., and Raade, G. (2006). Das Smaragd-Vorkommen von Byrud (Eidsvoll) in SØud-Norwegen [The emerald deposit at Byrud (Eidsvoll) in South Norway]. *Mineralien-Welt*, **17**: 52–64 [in German].
- Rondeau, B., Fritsch, E., Peucat, J.J., Nordrum, F.S., and Groat, L. (2008). Characterization of Emeralds from a historical deposit: Byrud (Eidsvoll), Norway. *Gems & Gemology*, **44**: 108–22.
- Turner, D., and Groat, L.A. (2007). Chapter 4: Non-emerald gem beryl. In *Geology of Gem Deposits, Short Course 37*. Edited by L.A. Groat. pp. 79-109. Mineralogical Association of Canada, Yellowknife, Northwest Territories.

3. Boiling as a mechanism for colour zonations observed at the Byrud emerald deposit, Eidsvoll, Norway: fluid inclusion, stable isotope and Ar-Ar studies.*

Loughrey, L. E.

Department of Earth Sciences, Simon Fraser University,
Burnaby, BC, V5A 1S6, Canada

Marshall, D. D.

Department of Earth Sciences, Simon Fraser University,
Burnaby, BC, V5A 1S6, Canada

Ihlen, P.

Geological Survey of Norway (NGU), P.O. Box 6315 Sluppen, NO-7491,
Trondheim, Norway

Jones, P.

Earth Sciences, Carleton University,
Ottawa, ON, K1S 5B6, Canada

*Modified from a publication in *Geofluids* and reproduced here (including acknowledgements and references) as Chapter 3.

3.1. Abstract

The Byrud emerald deposit comprises pegmatite veins hosted within Cambrian black shales and Late Carboniferous quartz syenite sills, which are intruded by a Permo-Triassic riebeckite granite. The emerald deposit genesis is consistent with a typical granite-related emerald vein system from dominantly magmatic fluids with minor contributions from metamorphic source(s). Muscovite from an emerald-bearing pegmatite at Byrud yielded reliable Ar-Ar plateau age of 233.4 ± 2.0 Ma. Emerald display colour zonation alternating between emerald and beryl. Two dominant fluid inclusions types are identified: two-phase (vapour+liquid) and three-phase (brine+vapour+halite) fluid inclusions and these are interpreted to represent conjugate fluids of a boiling system. The emerald was precipitated from these saline fluids with approximate overall salinities on the order of 31 mass percent NaCl equivalent. Raman analyses indicate molar gas fractions for CO₂, N₂, CH₄, and H₂S are approximately 0.8974, 0.0261, 0.0354, and 0.0410, respectively. Formational temperatures and pressures of approximately 160 °C to 385 °C and below 1000 bars were derived from fluid inclusion data and lithostatic pressure estimates from fluid inclusion studies within the Oslo Paleorift. The colour zonation observed in the Byrud emerald crystals are related to alternating emerald and beryl precipitation in the liquid and vapour portions respectively of a two-phase (boiling) system.

3.2. Introduction

The Byrud emerald deposit was first discovered in the early 1860s, at Byrud Farm located near Lake Mjøsa, southern Norway (Figure 3-1). Vanadium-rich emerald, such as those from Byrud are relatively rare compared to the more common chromium-rich variety. There are only a few vanadium-rich emerald deposits including Colombia; Lened in the Northwest Territories, Canada; Salinha in Bahia, Brazil; Dyakou in Yunnan, China; Panjshir in Afghanistan; and Gandao in Pakistan (Rondeau et al., 2008; Groat et al., 2008).

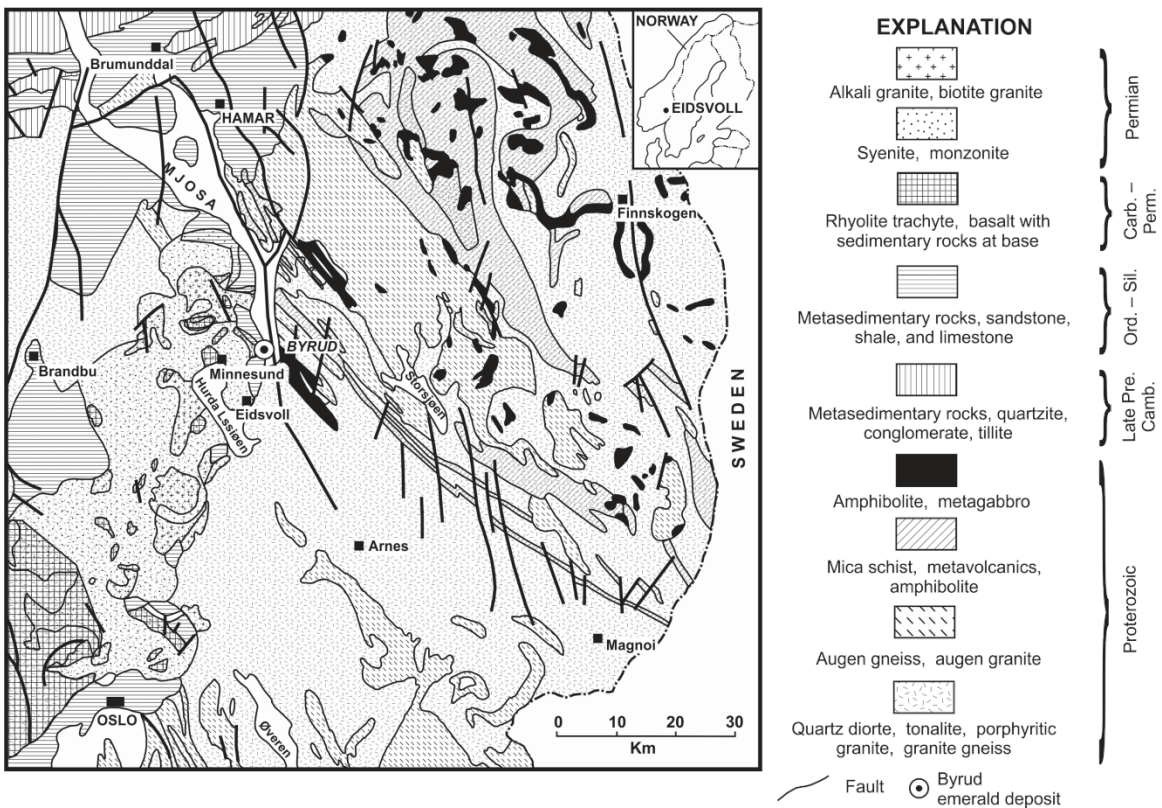


Figure 3-1. Geologic map of the Eidsvoll area, showing the locality of the Byrud emerald deposit on the western shore of Lake Mjøsa (modified from Kazmi and Snee, 1989; Larsen et al., 2008).

Initial prospecting and blasting at Byrud occurred late in the 19th century (Nordrum & Raade, 2006; Rondeau et al., 2008). The first gallery of a few square meters produced emerald crystals from small clay-filled cavities (Nordrum & Raade, 2006). In

the early stages of mining, a number of gemstone-quality emeralds were recovered, but many were pale in colour. During a 10 year mining interval, the recovery of gem quality emerald declined and the mine was abandoned by 1909. Consequently, there are few geological and geochemical data available for the Byrud occurrence. An extensive mineralogical study by G. Raade at the Geological Museum in Oslo identified 45 different minerals at Byrud. The history, geology, and mineralogy of the Byrud deposit were comprehensively described by Nordrum and Raade (2006). A summary of the history and geology is also documented by Rondeau et al. (2008). Their work focused on the gemological properties, chemical compositions, spectroscopy and identification of multiphase fluid inclusions, with their results compared with other emerald localities worldwide. Field work was conducted at the Byrud Mine in 2010 and 2012 and involved field and detailed mapping of the selected mineralized areas (specifically veins), detailed modal mineralogy, parageneses, alteration, and structures. This field work has been complemented by laboratory studies including petrography, scanning electron microscopy, electron microprobe analyses, and fluid inclusion studies with stable Ar-Ar isotopic analyses. This study focuses on identifying the genesis of the zoned emerald at Byrud and constraining the pressures, temperatures, and fluid conditions during deposition.

3.3. Geologic Setting

The Byrud emerald deposit in Eidsvoll, Akershus, southern Norway, is located in the northeastern part of the Permian Paleorift structure of the Oslo region. The emerald mineralization at Byrud is related to Permo-Triassic intrusions associated with the evolution of the Oslo Paleorift. The tectono-magmatic evolution of the Oslo Paleorift has been thoroughly studied and comprises six evolutionary stages (Ramberg and Larsen, 1978; Larsen and Sundvoll, 1984; Olerud and Ihlen, 1986; Larsen et al., 2008). The Oslo Paleorift is the northernmost part of the Rotliegende basin system in Europe. The rift was produced by lithospheric stretching and is tectonically related to the last phase of the Variscan orogeny. During the Late Carboniferous, the main graben formation began with 20-30 Ma of extensive volcanism and rifting, followed by uplift and emplacement of major batholiths. The emerald mineralization at Byrud is related to this stage of the rift system (Larsen et al, 2008). These batholithic rocks have been dated by the Rb-Sr

method yielding ages from 241 to 273 Ma (Sundvoll et al., 1990). Existing K-Ar geochronological data of the ore deposits yield ages ranging from 233 to 277 Ma (Ineson et al., 1975; Ihlen et al., 1977; Ineson et al., 1978). Zircon $^{238}\text{U}/^{206}\text{Pb}$ dates from igneous rocks within the Oslo Paleorift have similar ranges from 243 Ma (Nier, 1939) to 259 Ma (Faul et al., 1959). Molybdenite mineralization in the Oslo Paleorift near Drammen yielded a Re/Os age of 235 Ma (Neumann, 1960; Ineson et al., 1975). The final stage of the Oslo Paleorift concluded with the terminal intrusions in the Early Triassic, approximately 65 Ma after the onset of the tectonic and magmatic activity. Most of the ore deposits in the Oslo Paleorift have been related to the tectono-magmatic evolutionary model described by Larsen et al., (2008) and were formed during a number of different volcanic and intrusive stages (Ihlen, 1978; Olerud and Ihlen 1986). During the batholith stage of the Oslo Paleorift, hydrothermal activity resulted in most of the metallic and non-metallic mineralization in the area.

The initial Late Carboniferous and subsequent fissure eruptions built a 1000-2000 meter thick lava plateau composed of early alkali basaltic lavas and late latite porphyries and trachytes. This event generated a system of faults and breccia zones, with some representing reactivation of earlier Precambrian structures (Ramberg and Larsen, 1978; Larsen et al., 2008). Intrusions of circa 300 Ma (Larsen et al., 2008) syenitic (maenaite) sills along a Caledonian (Late Silurian) sole thrust of Cambrian shales are cut by Permian faults in some areas. One of these Permian faults parallels Lake Mjøsa (Lake Mjøsa Fault) immediately east of the emerald mine (Figure 3-1). The rocks to the east of this normal fault comprise a range of northwest-trending Meso- to Palaeoproterozoic granitic orthogneisses, gabbros and migmatitic gneisses. West of the fault at Byrud these Proterozoic orthogneisses are dominated by gray gneissic granodiorites unconformably overlain by Cambrian-Ordovician metasedimentary rocks. Further west inside the igneous complex of the Oslo Paleorift the fissure eruptions were succeeded by the formation of central volcanoes with associated emplacement of batholithic masses of early monzonites, nepheline syenites, intermediate stage syenites, granites, alkali syenites, alkali granites, late stage peralkaline syenites, and peralkaline granites (including riebeckite granite) emplaced at approximately 270-250 Ma (Larsen et al., 2008). These plutons are normally surrounded by a 3 km wide contact metamorphic aureole where the Cambrian to Early Ordovician black shales are metamorphosed into

biotite hornfels and Early Ordovician calcareous sediments converted to marbles and diopside-plagioclase hornfels. Most of the syenitic and granitic plutons contain miarolitic cavities within pegmatite segregations, which frequently host beryl.

3.4. Local Geology and Vein Petrology

Emerald mineralization occurred proximal to, but post-dates, flat-lying syenite sills which range in size from 0.5 m to several meters thick. These sills crosscut and hornfelsed Cambro-Ordovician shales (Figure 3-2). The sills are mainly quartz-rich along the borders, with the quartz primarily occurring as smoky quartz. At different levels the sills have been intruded by small pegmatite veins and veinlets that also crosscut the surrounding black Cambrian shale/hornfels (Figure 3-3). The pegmatite is generally discontinuous and form lenses or small dikes, ranging from a few centimetres to 50 cm thick. They consist of mainly K-feldspar and quartz with an overall quartz syenitic composition. The majority of the better-quality emerald occurs in the northern part of the mine area in small clay-bearing cavities in the pegmatite comprising dominantly quartz, muscovite, plagioclase, pyrite, pyrrhotite, fluorite, tourmaline, topaz and beryl (Rondeau et al., 2008). The pegmatite is likely associated with a large alkaline granite intrusion located west of Byrud. From field observations, it has been determined that beryl mineralization occurs dominantly in the pegmatite, and rarely as separate crystals in the syenite sills and black shale/hornfels (Figure 3-3). It was hypothesized that the vanadium and chromium chromophores, which colour the emerald, were leached from the shale. The carbonaceous black shale and hornfels contain several percent of amorphous carbon and fine-grained graphite, respectively, and locally thin layers rich in Fe-sulphides.

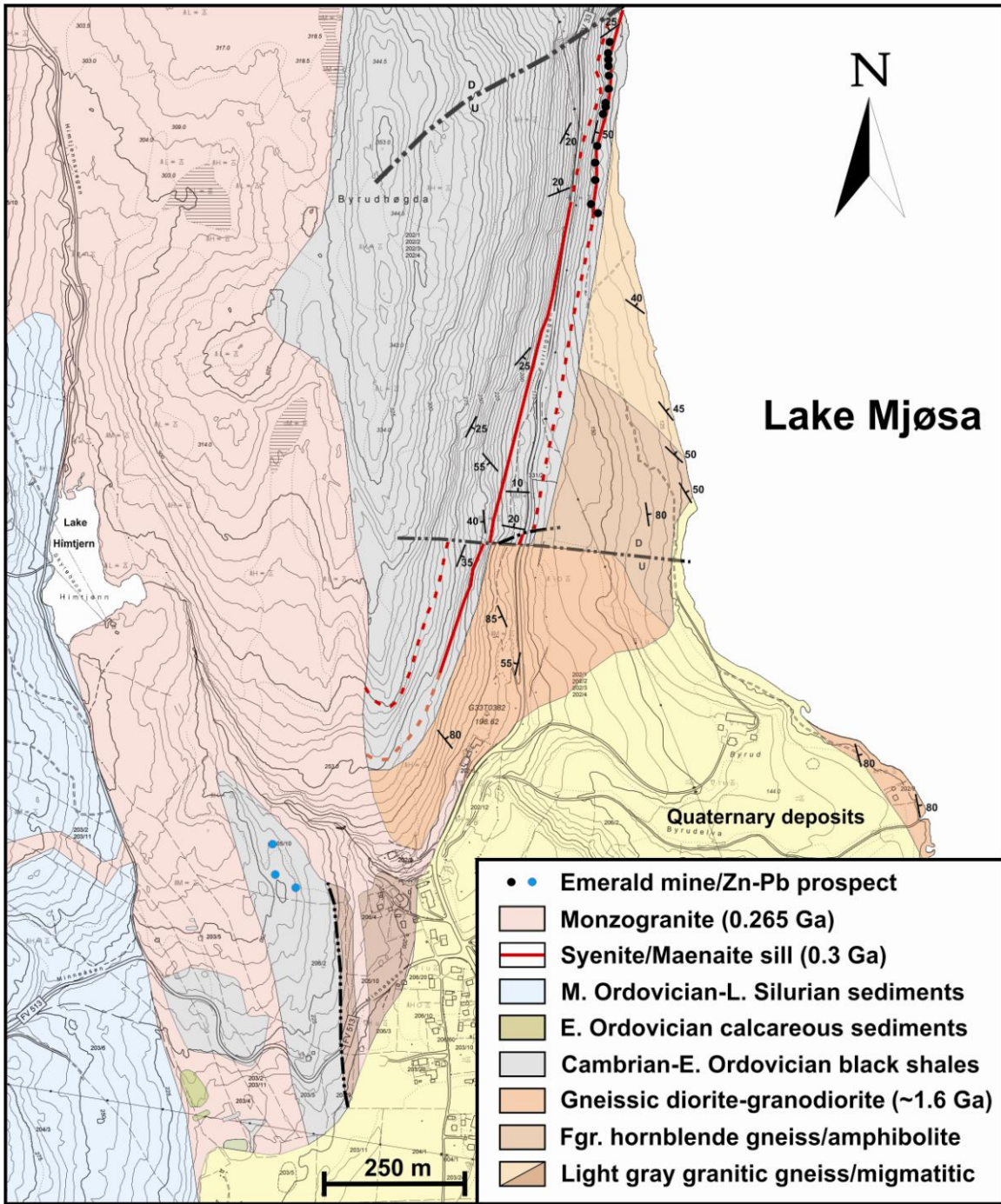


Figure 3-2. Topographic map showing location of the emerald mine on the western shore of Lake Mjøsa, Norway.

Emerald in the pegmatite and associated minor aplite dykes are often embedded in feldspar, quartz, muscovite, pyrrhotite and in fluorite. From previous studies, the crystals range up to 6 cm in length and 2 cm wide and form hexagonally shaped crystals with flat basal terminations; minor pyramidal faces have also been observed on the terminations of the Byrud emerald (Nordrum & Raade, 2006; Rondeau et al., 2008). The emerald colour is variable, from translucent and transparent green, bluish green to colourless, with grayish yellow beryl not uncommon. Some crystals have a lighter core, with topaz present in the cores. Many small flawless crystals of lighter colour have been identified. Additionally, some emerald exhibit alternating colour zones parallel to the basal plane, varying from colourless beryl to deep green emerald.



Figure 3-3. *Hand specimen collected from the Byrud mine displaying the contemporaneous relationship of the pegmatite/aplite and emerald. Dark layered clasts are contact metamorphosed host black shale/hornfels.*

3.5. Field and Laboratory Methods

Samples were taken from various locations within the mine and its surrounding areas, comprising the various rock types in the region and a number of emerald-bearing pegmatite veins. The collected material has been used for preliminary petrographic and geochemical studies. The fieldwork conducted also included detailed mapping of the mine area and individual emerald-bearing veins.

The emerald mine is accessible by a main road at Lake Mjøsa (Figure 3-2), with good exposures of riebeckite granite, pegmatite veins, syenite sills, and black bituminous shale/hornfels. The emerald mine is situated at the bottom of a tree-covered slope off the main road and is approximately 30-50 m from the western shore of Lake Mjøsa. All of the adits were investigated. Samples of zoned emerald were also collected, in order to determine the emerald formational model.

Electron microprobe analysis of beryl was performed at Carleton University using an automated 4 spectrometer Camebax MBX electron probe by the wavelength dispersive x-ray analysis method (WDX). Operating conditions were: 15kv accelerating potential and a beam current of 20 nano-amperes (nA). Counting times were up to 50 seconds or 40,000 accumulated counts. X-ray lines were chosen to minimize or eliminate possible elemental interferences. Raw x-ray data were converted to elemental weight % via the Cameca PAP matrix correction program. For the elements considered, the following standards, X-ray lines, and crystals were used: synthetic spinel, Al K α , TAP; Camargo olivine, Mg K α , TAP; albite, Si K α , TAP; wollastonite, Ca K α , PET; MnTi, Ti K α , PET; YVO $_4$, V K α , PET; synthetic chromite, Cr K α , LIF; MnTiO $_3$, Mn K α , LIF; synthetic fayalite, Fe K α , LIF; barite, Ba K α , PET; microcline, K K α , PET; synthetic cesium doped glass, Cs L α , PET; scandium metal, Sc K α , PET; tugtupite, Cl K α , PET; jadeite, Na K α , TAP. H $_2$ O was measured via a manometer during stable isotope analyses and an average value used to complement the probe analyses. Oxygen was calculated by stoichiometry and Be was calculated by difference.

For this study, 85 fluid inclusions from the emerald-bearing pegmatite veins were targeted for microthermometric measurements. Initial petrographic work was completed in order to identify different fluid inclusion assemblages in emerald and quartz. Of the 85

fluid inclusions measured, 53 inclusions were hosted in emerald and 32 in quartz. Fluid inclusion measurements were completed with a Linkam THMS-G 600 heating-freezing stage attached to an Olympus BX51 microscope equipped with 5, 10 and 50 X long working distance Olympus objectives. The stage is capable of measurements in the range of -190 to +400 °C. Prior to collecting heating and cooling measurements the stage was calibrated with two synthetic fluid inclusion standards. The first yields phase transitions for pure H₂O at 0.0 and 374.1 °C. The second standard comprises H₂O-CO₂ fluid inclusions and is used to calibrate the stage at -56.6 °C to the melting of solid CO₂. The stage was periodically tested against the standards and results were always within ±0.2 °C for the two low temperature phase transitions and within ±1.0 °C of the higher temperature phase transition. Raman spectra of fluid inclusions in emerald and quartz were collected on a laser-excited Dilor LabRam Raman microspectrometer using the 514.2 nm Ar ion laser. The presence of CO₂, N₂, H₂S, and CH₄ in two-phase and three-phase inclusions in both emerald and quartz were referenced to lines 1388, 2325, 2612, and 2910 cm⁻¹, respectively from Burke (2001) and Wopenka and Pasteris (1987). Mole fraction ratios for CO₂, N₂, H₂S, and CH₄ were calculated using equation (1) from Wopenka and Pasteris (1987) with relative scattering cross sections numbers supplied by Dhalmelincourt et al., 1979.

Stable isotope studies were performed on emerald, quartz and feldspar from material gathered from the Byrud farm and analyzed at Queen's University. The beryl-quartz and beryl-feldspar oxygen isotope equilibrium temperatures were calculated using the fractionation equations of O'Neil et al., 1967, Zheng, 1993a, Matsuhisa et al., 1979, and Xue et al., 2010.

Muscovite from the emerald-bearing pegmatites was chosen for ⁴⁰Ar-³⁹Ar geochronology to determine the age of emerald mineralization and to relate the local igneous rocks to the formation of emerald at Byrud. Sample LL11-06 was crushed, sieved, and handpicked to ensure pure mineral separate and sent to the Pacific Centre for Isotopic and Geochemical Research at the University of British Columbia. The sample was then crushed in a ring mill, washed in distilled water and ethanol, and sieved when dry to 40 +60 mesh. Appropriate mineral grains were picked out of the bulk fraction. Mineral separates were wrapped in aluminum foil and stacked in an irradiation capsule with similar-aged samples and 28.03 Ma Fish Canyon Tuff sanidine separates

(Renne et al., 1998) as neutron flux monitors. The samples were irradiated in July, 2012 at the McMaster Nuclear Reactor in Hamilton, Ontario, for 180 MWH in the medium flux site 8B. Analyses (n=33) of 11 neutron flux monitor positions produced errors of <0.5% in the J value. The mineral separates were step-heated at incrementally higher powers in the defocused beam of a 10W (New Wave Research MIR10) CO₂ laser until fused. The gas evolved from each step was analyzed by a VG5400 mass spectrometer equipped with an ion-counting electron multiplier. All measurements were corrected for total system blank, mass spectrometer sensitivity, mass discrimination, radioactive decay during and subsequent to irradiation, as well as interfering Ar from atmospheric contamination and the irradiation of Ca, Cl and K (Isotope production ratios: $(^{40}\text{Ar}/^{39}\text{Ar})_{\text{K}}=0.0302\pm 0.00006$, $(^{37}\text{Ar}/^{39}\text{Ar})_{\text{Ca}}=1416.4\pm 0.5$, $(^{36}\text{Ar}/^{39}\text{Ar})_{\text{Ca}}=0.3952\pm 0.0004$, $\text{Ca}/\text{K}=1.83\pm 0.01(^{37}\text{Ar}_{\text{Ca}}/^{39}\text{Ar}_{\text{K}})$).

3.6. Results

3.6.1. *Emerald Composition*

Emerald compositions from literature data compiled in Groat et al. (2008) are shown in Figure 3-4. The Byrud emerald have higher concentrations of vanadium than any other emerald deposit. Electron microprobe analyses were conducted along a traverse perpendicular to a zoned emerald crystal. The emerald displays concentric growth zones with a lighter colourless beryl core (Figure 3-5). The oxide concentrations for Cr, V, and Fe are shown along the electron microprobe traverse (Figure 3-5) across the zoned emerald. There is a good correlation between Cr and V concentrations and an inverse correlation between these elements and Fe. Overall, the emerald from Byrud are predominately vanadium-rich, with zones in the emerald related to chemical variations that result in emerald and beryl zones. Chemically, substitution occurs at the Y site in the crystal structure of beryl. Differences in colour and chemistry are due to complicated substitutions at this site and/or slight variations in fluid composition, with values of Cr₂O₃, V₂O₃, and Fe₂O₃, ranging up to 0.05, 0.47, and 0.30 mass percent respectively. These concentrations have been plotted relative to emerald analyses worldwide (Figure 3-4). The more vanadium-rich zones of the crystal are plotted in dark and the colourless beryl in light on Figure 3-4. The emerald/beryl colours are clearly related to vanadium

concentrations. The electron microprobe data from this study are comparable to similar results obtained by Rondeau et al. (2008) and Schwarz (1991), however both studies report higher vanadium concentrations.

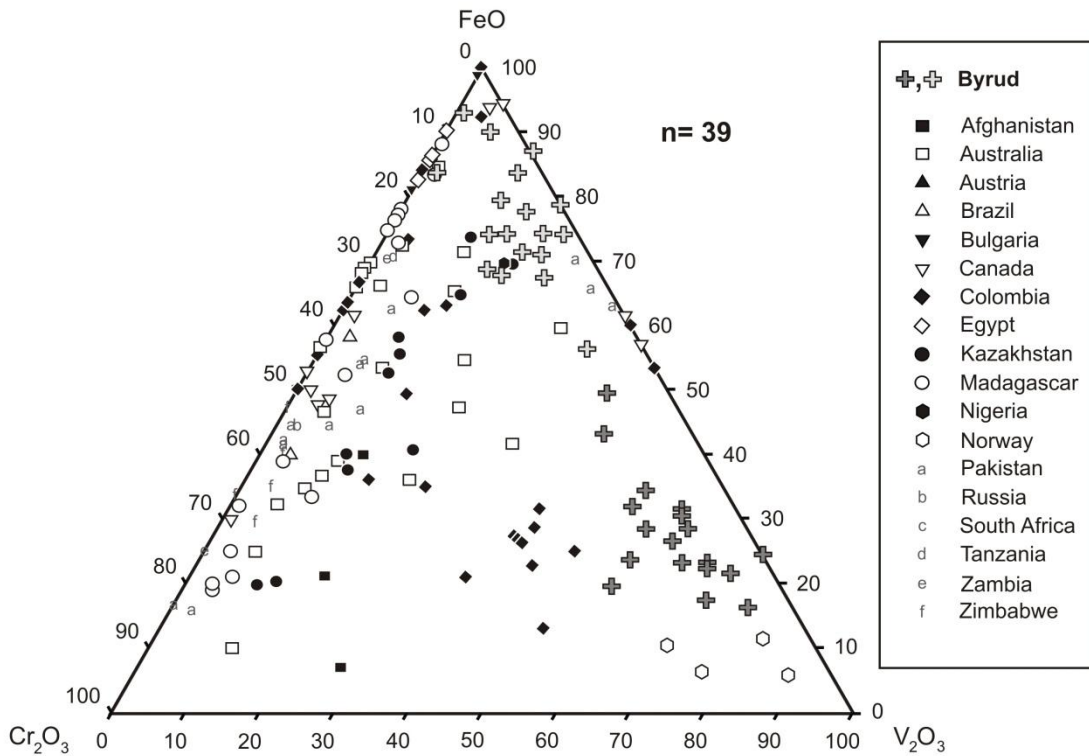


Figure 3-4. Ternary FeO-Cr₂O₃-V₂O₃ (mass %) plot of Byrud emerald compositions (dark and light gray plus signs) superimposed on the worldwide emerald compositions from literature data compiled in (Groat et al., 2008). Data are normalized from mass percent microprobe analyses, with Fe data reported as FeO.

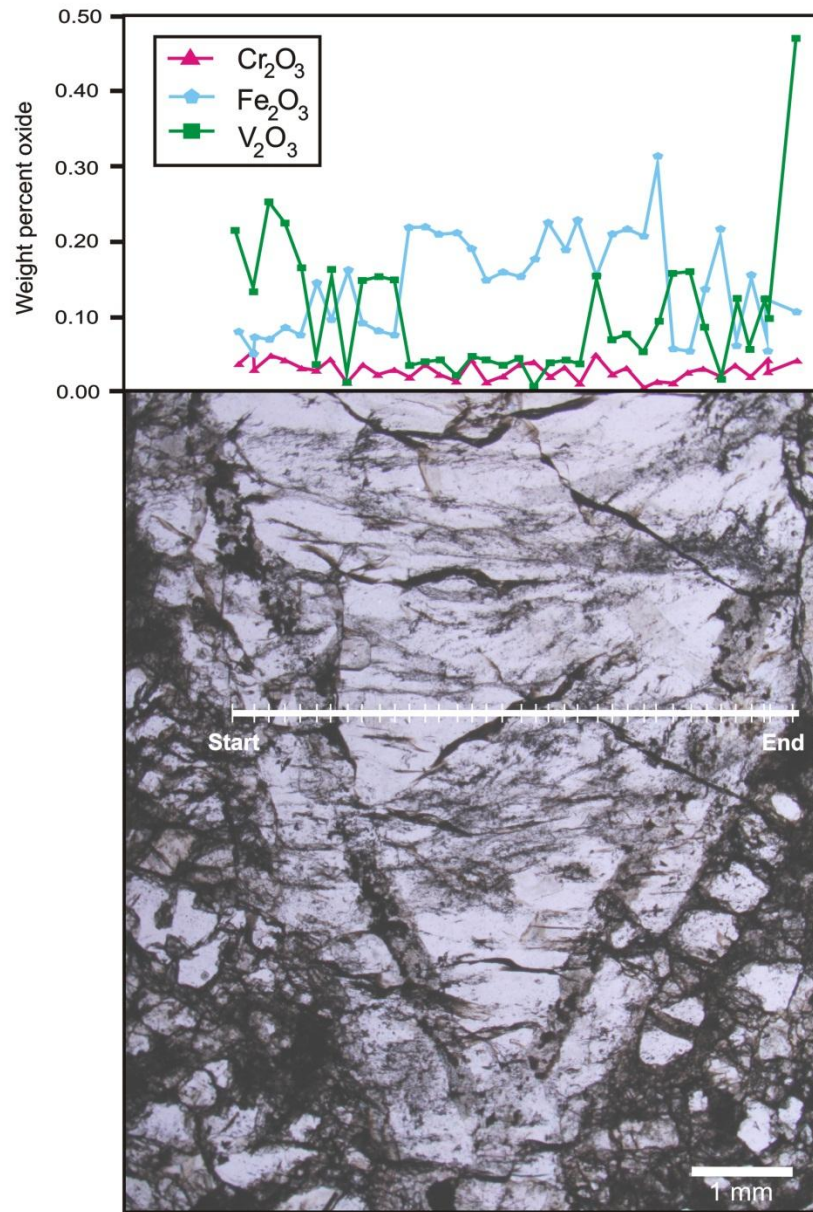


Figure 3-5. Mass percent oxide data for selected oxides in emerald along a microprobe traverse (thick horizontal white line). The photomicrograph is a zoned emerald crystal taken in plane polarized light. Electron microprobe analyses points are equally spaced (tick marks) from left to right and correspond to analyses 1 to 38 (Table 3-1).

Selected cation concentrations relative to Al and Mg+Mn+Fe respectively are plotted in Figure 3-6. The Byrud deposit displays low divalent-cation concentrations versus Al, comparable to the Australian and Kazakhstan emerald deposits. Additionally, the values for MgO and Na₂O are extremely low for the Byrud emerald and this is an additional characteristic of the deposit.

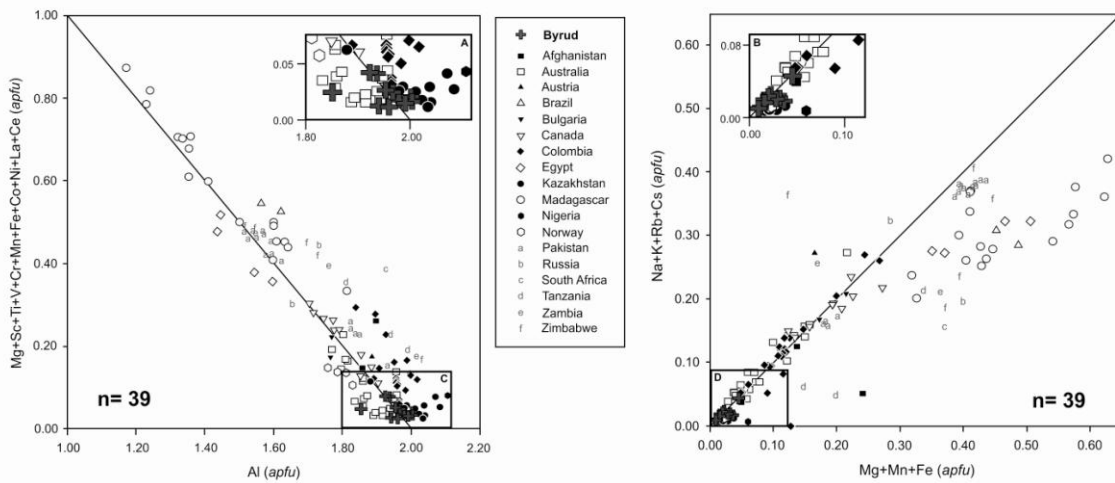


Figure 3-6. Al versus the sum of other Y-site cations, in atoms per formula unit. The Byrud emerald compositions (dark gray plus signs) are superimposed on worldwide emerald data. The second graph is an Mg+Mn+Fe versus monovalent channel-site cations, in atoms per formula unit. The Byrud emerald compositions (dark gray plus signs) are superimposed on worldwide emerald data compiled from the literature in Groat et al., 2008. Rectangles labelled A and B are expanded rectangles of insets C and D.

Table 3-1. Electron microprobe compositions along a traverse of the Byrud emerald.

Analysis#	1	2	3	4	5	6	7	8	9	10	11	12	13	14	15	16	17	18	19
SiO ₂ (mass %)	66.19	67.05	66.4	66.92	66.74	66.12	67.32	67.52	66.07	67.26	66.35	66.36	65.63	65.78	66.51	66.35	66.66	66.58	66.07
Al ₂ O ₃	18.61	18.78	18.57	18.72	18.73	18.80	18.56	19.08	18.62	18.82	18.68	18.69	18.40	18.73	18.77	18.64	18.89	18.92	18.85
TiO ₂	0.01	0.02	0.01	0.00	0.00	0.00	0.00	0.00	0.00	0.00	0.00	0.01	0.00	0.01	0.00	0.02	0.00	0.00	0.00
K ₂ O	0.01	0.01	0.01	0.00	0.00	0.00	0.00	0.01	0.00	0.00	0.00	0.00	0.00	0.00	0.00	0.00	0.00	0.00	0.00
CaO	0.00	0.00	0.00	0.00	0.00	0.00	0.00	0.00	0.00	0.00	0.00	0.00	0.00	0.00	0.00	0.00	0.00	0.00	0.00
FeO	0.04	0.06	0.06	0.07	0.06	0.12	0.08	0.14	0.08	0.07	0.06	0.19	0.19	0.18	0.18	0.16	0.13	0.14	0.13
Cs ₂ O	0.01	0.01	0.01	0.00	0.01	0.00	0.00	0.00	0.01	0.00	0.01	0.00	0.03	0.00	0.01	0.01	0.01	0.02	0.02
MnO	0.01	0.02	0.00	0.00	0.00	0.00	0.00	0.00	0.00	0.01	0.01	0.02	0.02	0.02	0.00	0.01	0.01	0.00	0.00
MgO	0.07	0.08	0.03	0.03	0.05	0.06	0.03	0.05	0.05	0.06	0.05	0.06	0.06	0.06	0.06	0.05	0.02	0.02	0.03
BaO	0.00	0.00	0.00	0.00	0.00	0.00	0.00	0.00	0.00	0.00	0.00	0.00	0.00	0.00	0.00	0.00	0.00	0.00	0.00
Sc ₂ O ₃	0.04	0.06	0.05	0.03	0.01	0.01	0.01	0.02	0.04	0.02	0.02	0.07	0.07	0.06	0.07	0.06	0.06	0.07	0.07
V ₂ O ₃	0.12	0.13	0.24	0.22	0.16	0.03	0.15	0.00	0.14	0.14	0.14	0.03	0.04	0.03	0.01	0.04	0.04	0.03	0.04
NaO	0.09	0.07	0.05	0.04	0.06	0.06	0.04	0.09	0.06	0.05	0.07	0.11	0.10	0.10	0.10	0.11	0.05	0.05	0.05
Cr ₂ O ₃	0.05	0.02	0.04	0.04	0.03	0.02	0.04	0.01	0.03	0.02	0.02	0.01	0.03	0.02	0.01	0.04	0.01	0.01	0.03
H ₂ O	0.95	0.00	0.69	0.00	0.25	0.97	0.00	0.00	1.14	0.00	0.75	0.60	1.75	1.25	0.40	0.67	0.23	0.27	0.91

Table 3-1. Continued.

Analysis#	20	21	22	23	24	25	26	27	28	29	30	31	32	33	34	35	36	37	38
SiO ₂ (mass %)	66.99	66.32	66.38	66.57	66.32	66.13	66.18	65.70	65.47	66.93	66.13	65.78	66.87	67.06	61.43	66.96	67.00	65.05	66.28
Al ₂ O ₃	18.86	18.40	18.71	18.77	18.87	18.79	18.56	18.68	18.21	18.86	18.72	17.13	18.66	18.73	17.52	18.62	18.86	17.92	18.13
TiO ₂	0.00	0.02	0.00	0.00	0.00	0.00	0.00	0.00	0.08	0.00	0.00	0.00	0.00	0.00	0.00	0.00	0.00	0.12	0.01
K ₂ O	0.00	0.00	0.00	0.00	0.00	0.00	0.00	0.00	0.00	0.00	0.00	0.01	0.00	0.00	0.00	0.00	0.00	0.00	0.00
CaO	0.00	0.00	0.00	0.00	0.00	0.00	0.00	0.00	0.06	0.00	0.00	0.16	0.00	0.00	0.06	0.00	0.00	0.00	0.00
FeO	0.15	0.20	0.16	0.20	0.13	0.18	0.19	0.18	0.27	0.05	0.04	0.12	0.19	0.05	0.13	0.04	0.10	0.09	0.13
Cs ₂ O	0.02	0.03	0.03	0.03	0.00	0.02	0.02	0.01	0.01	0.01	0.01	0.02	0.03	0.01	0.00	0.00	0.01	0.03	0.02
MnO	0.01	0.02	0.01	0.00	0.00	0.01	0.02	0.01	0.02	0.00	0.00	0.02	0.01	0.13	0.02	0.00	0.01	0.00	0.02
MgO	0.04	0.07	0.06	0.06	0.02	0.06	0.05	0.07	0.14	0.03	0.03	0.15	0.07	0.04	0.06	0.04	0.06	0.06	0.13
BaO	0.00	0.00	0.00	0.00	0.00	0.00	0.00	0.00	0.00	0.00	0.00	0.00	0.00	0.00	0.00	0.00	0.00	0.00	0.00
Sc ₂ O ₃	0.07	0.06	0.05	0.06	0.06	0.05	0.07	0.06	0.09	0.02	0.03	0.02	0.03	0.02	0.04	0.02	0.03	0.07	0.08
V ₂ O ₃	0.00	0.03	0.03	0.03	0.14	0.06	0.07	0.05	0.09	0.15	0.15	0.08	0.01	0.12	0.05	0.12	0.09	0.47	0.46
NaO	0.09	0.10	0.10	0.10	0.06	0.10	0.11	0.10	0.24	0.04	0.06	0.08	0.09	0.11	0.09	0.06	0.07	0.07	0.12
Cr ₂ O ₃	0.03	0.01	0.03	0.00	0.04	0.02	0.03	0.00	0.01	0.00	0.02	0.02	0.01	0.03	0.02	0.04	0.02	0.04	0.04
H ₂ O	0.00	0.94	0.58	0.29	0.49	0.75	0.92	1.42	1.64	0.00	1.02	2.88	0.12	0.00	7.72	0.20	0.00	2.53	0.79

All analyses are calculated based on 18 oxygen and 3 beryllium. H₂O is calculated by difference from the sum of all oxides.

3.6.2. Fluid Inclusions

Fluid inclusion studies on the Byrud emerald deposit identified two dominant Fluid Inclusion Types (FITs). The first is represented at room temperature by a two-phase (vapour+liquid) fluid inclusions (Figure 3-7). This FIT is abundant in quartz and emerald, and consists of a brine and vapour bubble. The second FIT is represented at room temperature by three-phase inclusions. These are commonly observed in quartz and to a lesser extent in emerald. (Figure 3-7). These inclusions consist of a brine, vapour bubble, halite cube and rarely trapped accidental minerals. Previous studies indicate that the three-phase fluid inclusions may have trapped several sulphide phases, such as pyrrhotite, galena, and sphalerite, which are distinctive to the Byrud emerald (Rondeau et al., 2008). The fluid inclusions in the samples studied occur as planes of inclusions along healed fractures, growth zones or as isolated inclusions. Minor growth zones observed in the emerald and quartz made it possible to conclusively identify primary and pseudo-secondary fluid inclusions from both FITs, based on timing relationships between fluid inclusions and mineral growth characteristics.

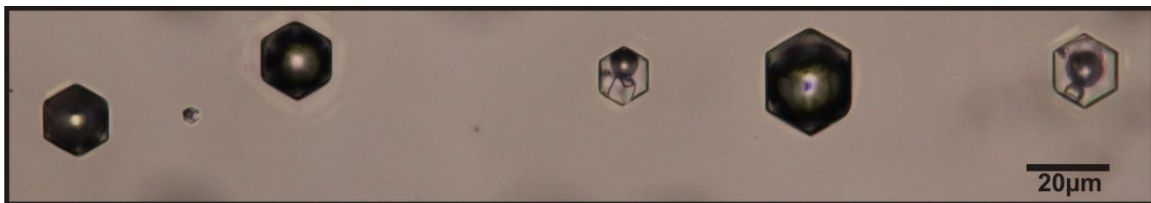


Figure 3-7. *Photomicrograph of a boiling assemblage in quartz consisting of a two-phase (vapour+liquid) and three-phase (liquid+vapour+halite) fluid inclusions. Sample LL11-08A. Photo taken in plane polarised light.*

Petrographically, primary three-phase fluid inclusions and pseudo-secondary two-phase fluid inclusions occur in a zoned emerald crystal. Trails of pseudo-secondary inclusions occur in the clear zones of the emerald (i. to vii. in Figure 3-8). The trails are only observed in these zones and terminate within the clear zones and at the edge between a green and clear zone. In Figure 3-8, it was also possible to identify primary

three-phase fluid inclusions within the green (emerald) zones. Further petrographic observations of two-phase and three-phase fluid inclusions along the same healed fractures are also identified in a number of quartz crystals (Figure 3-7). Fluid inclusion assemblages (FIAs) were identified based on the relationships of the fluid inclusions to healed fractures and growth zones (Goldstein, 2003).

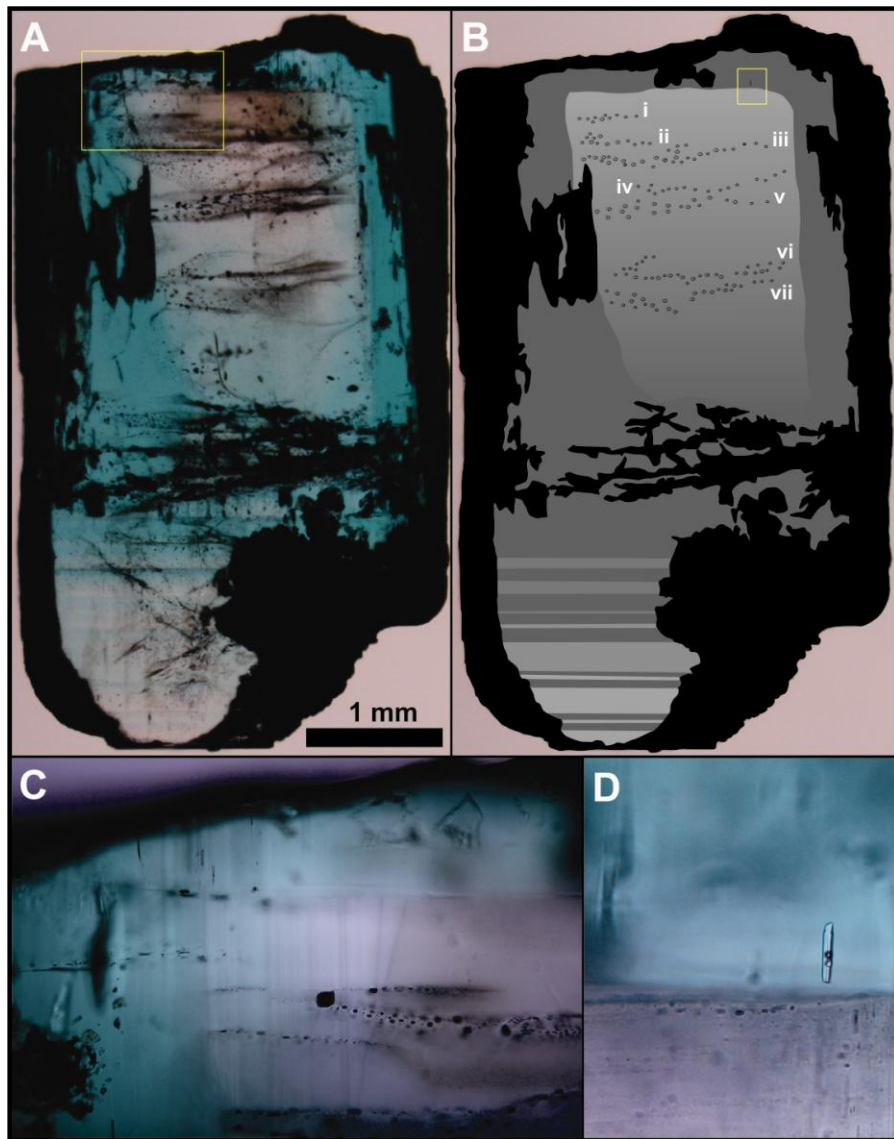


Figure 3-8. *A: Zoned emerald from the Byrud deposit with colour zonations parallel to the c-axis of the crystal, as well as parallel to the basal pinacoid. These colour zones alternate between green (emerald) and colourless beryl with variable growth zone thickness. Both liquid+vapour (L+V) pseudo-secondary fluid inclusions and liquid+vapour+halite (L+V+H) primary fluid inclusions are present in this sample. B: Schematic of the growth zones and the L+V pseudo-secondary vapour-rich inclusions trails labelled i. to vii. These trails terminate in the clear zones, as well as at the clear/green zone boundaries. C: photomicrograph of the expanded area of the rectangle in A showing the pseudosecondary (L+V) inclusion trails. D: Expanded area of the rectangle in B showing a primary c-axis parallel L+V+H fluid inclusion in a green (emerald) zone.*

The dominant phase in the two-phase inclusions is the gaseous phase that occupies approximately 50-70% of the fluid inclusion volume at room temperature. A second sub-FIT of two-phase inclusions displays fluid inclusion volumes where the gaseous phase occupies approximately 10-20%, and the aqueous brine comprises 80-90% of the remaining fluid inclusion volume. The inclusions display relatively consistent phase proportions within each sub-FIT and FIA, generally, and range up to 60 microns in size. The main phase in the three-phase FITs is the aqueous brine that constitutes approximately 50-60% of the fluid inclusion volume, with 25-35% volume in the vapour phase and the remaining 15% volume is halite. A second sub-FIT related to the three-phase inclusions is present displaying fluid inclusion volumes of 15% vapour phase, 10% halite cube and 75% aqueous brine. These inclusions can range up to 48 microns in size, and display somewhat variable phase proportions within specific FIAs. None of the two-phase and three-phase inclusions within the two sub-FITs could be identified as primary or pseudosecondary and in general displayed textures consistent with necking down, it is however possible that both these sub-FITs are derived from inhomogeneous trapping of varying amounts of the liquid and vapour portions of a boiling system.

Fluid inclusions within the pegmatites and progenitor granite sampled 3 km from the emerald mineralization have abundant fluid inclusions. These fluid inclusions are petrographically similar to the two- and three-phase FITs as well as sub-FITs observed in the quartz and emerald from Byrud. Predominantly, the granite hosted fluid inclusions occur along healed fractures in quartz and are confidently identified as secondary. There are numerous isolated three-phase fluid inclusions of indeterminate origin, and although these may be primary fluid inclusions, the lack of growth zones precludes identification of any primary fluid inclusions (Goldstein, 2003).

3.6.3. Microthermometry

Fluid inclusion microthermometric experiments on the two-phase FIT in emerald resulted in the nucleation of clathrate during rapid cooling at approximately -44 °C and ice at approximately -55 °C (Table 3-2). In rare cases, solid CO₂ formed at approximately -107 °C. Upon further cooling to -160 °C, no other phase changes were observed. Heating the inclusions from -160 °C resulted in melting of solid CO₂ ranging from -56.6 to -59.8 °C. Continued heating resulted in the first melting of ice over the temperature

range -65 °C to -54 °C. Further heating resulted in the final ice melt temperatures which ranged from -5.8 °C to 0.0 °C, with clathrate final melt temperatures ranging between +9.1 °C to +12.7 °C. Heating the inclusions from room temperature resulted in an increase in the volume of the vapour bubble, until the inclusions undergo total homogenisation to the vapour (Liquid + Vapour → Liquid) over a temperature range from 161 °C to 383 °C. Final ice melt and clathrate melt temperatures correspond to a range of salinities from 0.0 to 7.8 mass percent NaCl equivalent, using Bodnar (2003b) and a modification of the Diamond (1992) technique. Impurities in the CO₂ were detected via depression of the CO₂ triple point. However due to the mixtures of CO₂, N₂, CH₄, and H₂S present, more precise mole fraction estimates in the two-phase inclusions were obtained via Laser Raman spectroscopy and are on the order of 0.8974, 0.0261, 0.0354, and 0.0410, respectively (Figure 3-9).

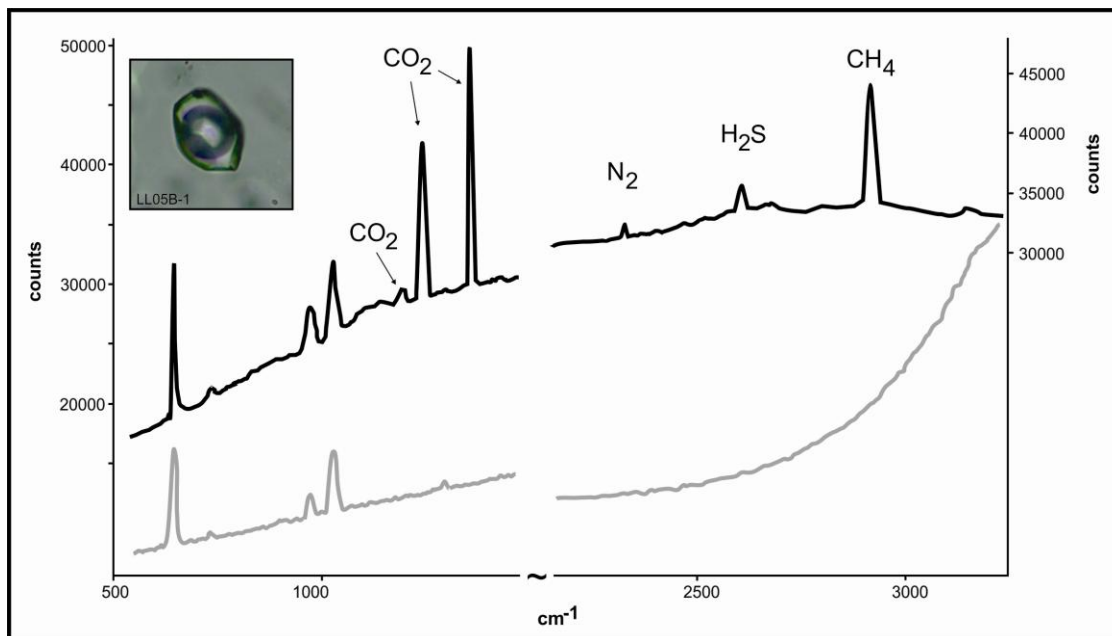


Figure 3-9. Raman microprobe spectra of CO₂, N₂, CH₄, and H₂S in sample LL05B-1 are shown in black signature. The corresponding background spectra (gray) show the peaks from background beryl over the analysed spectra regions. The analysed fluid inclusion shown in the inset is 60µm in length.

Upon rapid cooling from room temperature to -160 °C, the three-phase FIT nucleated clathrate at approximately -68 °C and ice at approximately -87°C. No other phase changes were observed during cooling. Heating the inclusions resulted in the first melting of ice over the temperature range -58 °C to -51 °C. Final ice melt temperatures upon further heating occurred over the temperature range -29.4 °C to -18.3 °C, with clathrate final melt temperatures ranging between +10.3 °C to +14.2 °C. Heating the inclusions from room temperature resulted in a decrease in the vapour bubble and halite cube until final homogenization of the fluid inclusion to the liquid (and more rarely the vapour) phase over the temperature range of 152 °C to 192 °C for inclusions where total homogenisation is via halite melting (Liquid + Halite → Liquid), and over the range 231 °C to 319 °C for inclusions that undergo total homogenisation via vapour bubble homogenisation (Liquid + Vapour → Liquid). The halite melting temperatures measured in the three-phase inclusions correspond to a range of salinities from 29.8 to 31.5 mass percent NaCl equivalent, using the equations of Bodnar (2003a,b). Some three-phase inclusions trapped rare birefringent phases. The birefringent phases did not melt upon heating and are thus interpreted as accidentally trapped minerals.

Table 3-2. Microthermometric measurements on the fluid inclusions from emerald at Byrud.

finc number	Tn cla	Tn ice	Tm ice	Tm hydrohalite	Tm cla	Tmhal	Th total	Fluid Inclusion Assemblages
1	-38.4	-58.3	-3.9	nv	11.1	nv	383.3	S (1)
2	-35.7	-54.3	-3.8	nv	11.4	nv	380.2	S(1)
3	-36.1	-55.4	-3.8	nv	11.3	nv	376.4	S (1)
4	-34.8	-36.7	-3.7	nv	nv	nv	348.9	PS(1)
5	nv	-36.5	-3.1	nv	nv	nv	nv	PS (1)
6	nv	-36.4	-3.4	nv	nv	nv	362.4	PS (1)
7	-30.4	-52.4	-2.0	nv	12.1	nv	280.4	P (1)
8	-31.4	-58.5	-2.1	nv	11.9	nv	309.7	P (1)
9	nv	-53.7	-1.9	nv	nv	nv	275.9	P (1)
10	nv	-82.4	-0.5	nv	12.7	nv	280.2	S (2)
11	-38.4	-55.7	-4.1	nv	9.8	nv	nv	P (3)
12	-48.2	-62.4	-4.7	nv	10.5	nv	290.2	S(4)
13	-48.7	-61.4	-3.9	nv	nv	nv	287.4	S(4)
14	-38.7	-58.4	-3.7	nv	11.2	nv	375.1	PS (5)
15	-39.8	-54.2	-2.5	nv	9.1	nv	352.8	PS (6)
16	-37.9	-57.4	-2.9	nv	10.6	nv	371.1	PS (6)
17	nv	-42.5	-0.2	nv	nv	nv	271.4	S (7)
18	-45.9	-66.7	-1.5	nv	10.7	nv	297.8	PS (8)
19	nv	-51.2	-0.8	nv	nv	nv	270.1	S (9)
20	-40.5	-58.4	-0.1	nv	12.1	nv	261.4	S (10)
21	-48.1	-57.6	-4.6	nv	nv	nv	281.4	S (11)
22	nv	-51.6	-3.5	nv	nv	nv	218.2	S(12)
23	nv	-50.1	-3.4	nv	nv	nv	178.1	S(12)
24	-48.4	-53.4	-3.5	nv	9.8	nv	251.2	S(12)
25	-46.2	-49.8	-4.1	nv	nv	nv	230.2	P (13)
26	-43.6	-52.2	-4.3	nv	11.0	nv	229.4	P (13)
27	-45.2	-50.9	-4.2	nv	11.2	nv	238.4	P (13)
28	-44.1	-53.4	-2.4	nv	11.4	nv	200.1	P (14)
29	-44.4	-53.5	-2.5	nv	nv	nv	199.8	P (14)
30	nv	-53.9	-2.5	nv	nv	nv	161.2	P (14)
31	-45.9	-56.7	-3.4	nv	nv	nv	267.1	S (15)
32	-51.6	-57.8	-5.1	nv	nv	nv	285.4	S (16)
33	-50.4	-61.3	-5.1	nv	10.4	nv	231.4	S (16)
34	-52.4	-60.1	-5.0	nv	10.8	nv	248.5	S (16)
35	-55.9	-60.4	-5.3	nv	11.0	nv	194.5	P (17)
36	-53.4	-67.6	-5.7	nv	nv	nv	237.4	S (18)
37	nv	-60.4	-5.8	nv	nv	nv	239.7	S (19)
38	nv	-84.2	-25.1	-1.1	nv	161.2	317.9	S (20)
39	nv	-87.4	-22.5	-0.5	10.3	168	287.9	S (20)
40	nv	-84	-29.4	nv	11.8	179.2	259.4	S (21)
41	-63.4	-89.4	-23.4	-5.1	10.3	192.4	264.2	S (22)
42	nv	-89.2	-24.1	-5.5	10.8	185.4	221.0	S (23)
43	nv	-86.4	-19.1	-0.3	nv	184.1	290.2	S (24)
44	nv	-89.4	-20.5	-0.4	nv	178.2	292.4	S (25)

45	nv	-89.6	-25.2	-5.6	nv	182.1	231.7	S (26)
46	nv	-88.1	-23.9	-5.4	nv	175.7	234.1	S (27)
47	nv	-89.9	-26.8	-5.1	14.2	173.2	242.7	S (28)
48	-72.1	-78.4	-22.1	-4.8	13.8	169.4	298.4	S (28)
49	nv	-89.7	-19.8	-4.1	nv	nv	nv	S (29)
50	nv	-88.7	-27.4	-4.2	nv	178.4	301.4	S (30)
51	nv	-89.4	-25.1	-4.5	nv	169.2	237.4	S (31)
52	nv	-88.9	-18.3	-4.5	nv	152.4	238.2	S (31)
53	nv	-87.1	-25.2	-4.0	nv	164.2	319.4	S (32)
54	-38.2	-62.1	-29.1	-1.1	nv	218.1	386.4	S(33)
55	-40.2	-58.7	-24.9	-0.8	12.3	217.8	385.6	S(33)
56	-38.7	-61.7	-23.6	nv	13	218.9	390.1	S(33)
57	-30.1	-86.1	-28.8	nv	12.2	242.1	>420	S(34)
58	nv	-52.3	-21.7	nv	nv	194.2	380.2	S(35)
59	nv	-51.6	-24.9	nv	nv	246.1	420.2	S(36)
60	nv	-68	-25.1	nv	nv	244.1	412.1	S(36)
61	nv	-62	-24.8	nv	nv	242.4	414.3	S(36)
62	-40.2	-51.7	-4.3	nv	9.2	nv	>420	S(37)
63	-42.5	-71.9	-6.1	nv	10.4	nv	>420	S(38)
64	-45.3	-57.2	-5.4	nv	10.1	nv	>420	S(38)
65	-43.2	-50.2	-5.2	nv	9.8	nv	>420	S(38)
66	-37.4	-48.9	-2.4	nv	8.9	nv	>420	S(39)
67	-38.4	-50.5	-4.9	nv	9.7	nv	>420	S(40)
68	-38.2	-49.7	-5	nv	9.5	nv	>420	S(40)
69	-47.2	-54.1	-6.2	nv	9.5	nv	>420	S(41)
70	-41.2	-55.4	-5.8	nv	10.1	nv	>420	S(41)
71	nv	-75.4	-20.2	-1.2	nv	196.4	>420	S(41)
72	-44.1	-72.6	-28.4	-1.2	11.9	250.2	373.2	S(42)
73	-38.8	-68.3	-24.8	nv	12.2	231.5	335.4	S(42)
74	-37.9	-65.4	nv	-0.8	11.8	232.7	361.2	S(42)
75	-34.5	-60.4	-1.6	nv	10.7	nv	>420	S(43)
76	-34.7	-57.8	-1.9	nv	9.2	nv	>420	S(43)
77	-39.1	-67.5	-24.2	nv	nv	255.2	398.5	S(44)
78	-38.4	-68.1	-26.1	nv	12.1	260.1	396.1	S(44)
79	nv	-79.2	-21.6	nv	nv	257.7	270.1	S(45)
80	nv	-75.7	-22.1	nv	nv	253.4	258.1	S(45)
81	nv	-81.4	-25.8	nv	nv	258.1	281.6	S(45)
82	-34	nv	-3.1	nv	11.2	nv	>400	S(46)
83	nv	-38.6	-1.1	nv	nv	nv	300.9	S(47)
84	nv	-36.7	-0.9	nv	nv	nv	301.2	S(47)
85	nv	-36.5	-0.8	nv	nv	nv	291.7	S(47)

All temperatures reported in Celsius, Tn cla=Clathrate nucleation temperature, Tn ice=Ice nucleation temperature, Tm ice=Ice melting temperature, Tm cla=Clathrate melting temperature, Tm hydrohalite=hydrohalite melt temperature, Tm hal=halite melting/dissolution temperature, Th total= final homogenization temperature to a one-phase fluid, nv=not visible, P=primary, S=secondary, PS=pseudo-secondary, (1),(2),(3)=individual fluid inclusion assemblage. Light gray sample numbers are measurements made in emerald, dark gray sample numbers are measurements in quartz.

3.6.4. Stable isotopes

Emerald and beryl crystallise in the hexagonal system and are composed of interconnected six-membered rings of silica tetrahedra producing channels parallel to the c-axis. The channels are wide enough to accommodate a range of aqueous fluids and dissolved cations that maintain charge balance within the beryl. The fluids and most importantly water, trapped within the channel contribute minimally to the overall $\delta^{18}\text{O}$ of the beryl host. More significantly, these fluids contain the only hydrogen as molecular H_2O within the beryl structure and represent the original formational fluid in equilibrium with the beryl during crystallization (Taylor et al., 1992). Extraction and trapping of the channel fluids above 800°C and subsequent δD analyses have been used in conjunction with $\delta^{18}\text{O}$ analyses of the beryl to distinguish between different emerald deposits, determine fluid source and deposit type (Giuliani et al., 1997). Hydrogen and oxygen stable isotope ratios from emerald channel fluids (Table 3-3) yield $\delta^{18}\text{O}$ values ranging from 8.7 to 10.3 ‰, and δD values from -24 to -31 ‰, relative to VSMOW international standard. These values are consistent with the mixed $\delta^{18}\text{O}$ - δD signature from metamorphic and magmatic sources (Figure 3-10).

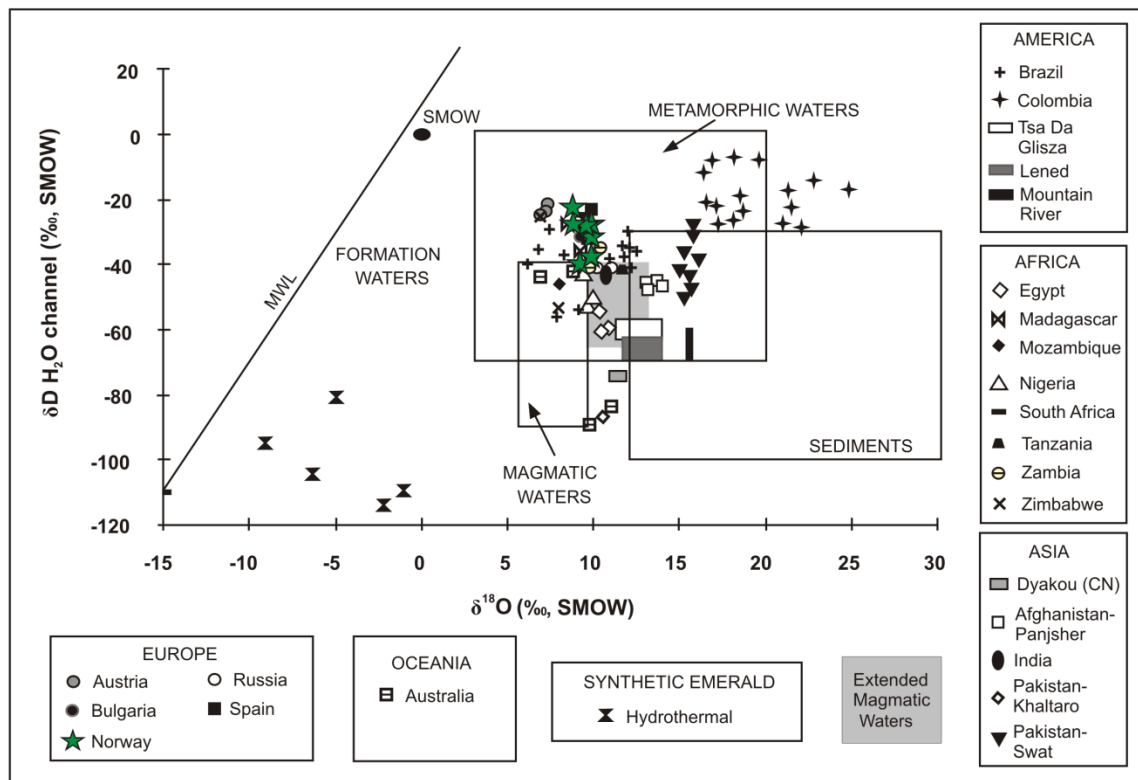


Figure 3-10. Channel $\delta D H_2O$ versus $\delta^{18}O$ for the Byrud emerald (green stars) superimposed upon data from a number of world localities compiled in the literature by Groat, 2008, Giuliani et al., 1997. The isotopic compositional fields are from Giuliani et al., 1998 including the extended (Cornubian) magmatic water box (gray). MWL=Meteoric Water Line, SMOW=standard mean ocean water.

The limited $\delta^{18}O$ OV-SMOW data for quartz and beryl (Table 3-3) yield quartz-beryl fractionation thermometry values for the Byrud emerald occurrence that are in excess of geologically feasible temperatures using the empirically derived equation of O'Neil et al., 1967, Zheng, 1993a, Matsuhisa et al., 1979, and Xue et al., 2010. The beryl-quartz thermometry yielded an equilibrium temperature of 1101 °C. The beryl-feldspar thermometers yielded excessively high temperatures ranging from 900 °C to 1300 °C with the use of a combination of O'Neil et al., 1967, Zheng, 1993a, Matsuhisa et al., 1979, and Xue et al., 2010. These high temperatures are likely related to variations in the emerald $\delta^{18}O$ due to chemical zonation and are discussed below.

Table 3-3. Stable isotope data for the Byrud emerald deposit.

Sample	Mineral	$\delta^{18}\text{O}_{\text{VSMOW}}\text{‰}$	Amt% H_2O	$\delta\text{D}_{\text{VSMOW}}\text{‰}$
LL11-05A	Beryl	9.5	0.8	-28
LL11-05A	Feldspar	8.7	-	-
LL11-05B	Beryl	9.1	1.1	-26
LL11-05C	Beryl	9.7	1.1	-31
LL1105C	Feldspar	10.3	-	-
LL11-06	Beryl	9.1	1.1	-24
LL11-07	Beryl	9.8	1.2	-26
LL11-07	Quartz	9.6	-	-

3.6.5. Ar-Ar Geochronology

Fresh muscovite from the emerald-bearing pegmatite veins yielded an ^{40}Ar - ^{39}Ar plateau age of 233.4 ± 2.0 Ma based on 69.5% of the total ^{39}Ar released (Figure 3-11), with an additional 16 percent of the gas yielding the same age as the plateau. There are slightly different ages observed in Figure 3-11, which represents minor amounts of radiogenic argon released during low and high temperature heating steps. These non-plateau steps displays minor amounts of gas that yield somewhat older ages (269 Ma to 281 Ma) and may possibly be interpreted as excess argon. However, from the inverse isochron plot, the same data produces an even tighter age of 234.3 ± 3.1 Ma and an exceptionally low MSWD of 2.3. The y-intercept is in direct agreement with atmospheric argon; as well the measured Ca/K (Figure 3-11; Table 3-4) are an order of magnitude less compared to typical muscovite with chlorite or clay alteration (Negro et al., 2008). Thus, the emerald-bearing pegmatite veins yield geologic interpretable plateau and isochron ages consistent with emerald deposition occurring at 234 ± 3.1 Ma as part of the Middle Triassic plutonism associated with the last stage of the Oslo Paleorift.

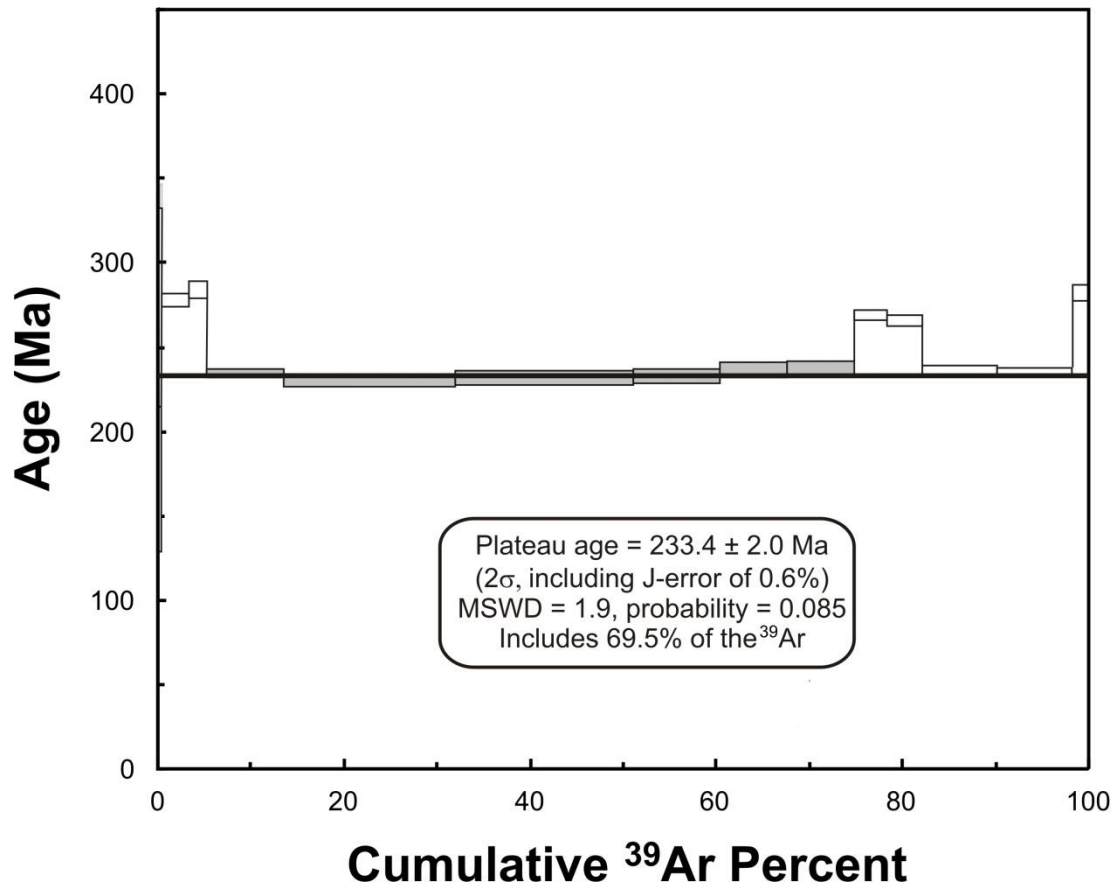


Figure 3-11. *⁴⁰Ar-³⁹Ar gas release spectra showing plateau age of Middle Triassic. The plateau age is shown as a black line across the individual spectrum. Laser heating steps used in the calculation of the plateau age are shown in gray.*

Table 3-4. $^{40}\text{Ar}/^{39}\text{Ar}$ Ages from vein muscovite in textural equilibrium with emerald.

Laser	Isotope Ratios LL11-06 muscovite (sample/mineral)											
Power(%)	40Ar/39Ar	1 σ	37Ar/39Ar	1 σ	36Ar/39Ar	1 σ	Ca/K	%40Ar atm	f 39Ar	40Ar*/39ArK	Age	2 σ
2.30	119.61	1.28	0.12	0.07	0.332	0.010	0.21	82.00	0.11	21.529	170.42	± 43.43
2.60	67.01	0.82	0.06	0.04	0.078	0.003	0.10	34.47	0.14	43.912	332.06	± 14.53
3.00	37.82	0.25	0.02	0.00	0.006	0.000	0.04	4.59	2.88	36.088	277.19	± 3.71
3.20	44.58	0.27	0.03	0.00	0.026	0.001	0.06	17.17	1.93	36.926	283.14	± 4.66
3.40	31.60	0.18	0.01	0.00	0.005	0.000	0.02	4.93	8.39	30.038	233.59	± 2.61
3.50	29.96	0.16	0.01	0.00	0.001	0.000	0.01	1.42	18.17	29.533	229.89	± 3.87
3.50	30.01	0.16	0.02	0.00	0.001	0.000	0.04	0.90	19.32	29.744	231.44	± 3.86
3.50	30.17	0.16	0.01	0.00	0.001	0.000	0.02	0.87	9.19	29.910	232.65	± 3.85
3.60	30.77	0.19	0.01	0.00	0.001	0.000	0.02	1.08	7.23	30.437	236.49	± 4.15
3.80	30.87	0.17	0.01	0.00	0.001	0.000	0.01	1.26	7.16	30.482	236.82	± 3.97
4.10	35.37	0.21	0.04	0.00	0.002	0.000	0.07	1.36	3.42	34.892	268.65	± 3.02
4.50	34.73	0.21	0.01	0.00	0.001	0.000	0.02	0.84	3.80	34.442	265.43	± 3.06
5.00	30.72	0.17	0.01	0.00	0.001	0.000	0.02	1.01	8.00	30.415	236.33	± 2.42
5.50	30.56	0.18	0.00	0.00	0.001	0.000	0.01	0.98	8.22	30.258	235.19	± 2.63
6.00	37.28	0.22	0.03	0.00	0.002	0.000	0.05	1.63	2.06	36.672	281.34	± 4.85
Power(%)	40Ar/39Ar	□	37Ar/39Ar	□	36Ar/39Ar	□	Ca/K	%40Ar atm	f 39Ar	40Ar*/39ArK	1□	
Total/Average	32.570	0.051	0.012	0.000	0.0010	0.0000			100.00	31.855	0.064	
J = 0.0045904 ± 0.0000230			Volume 39ArK =	0.832	Integrated Date =	247.09	± 0.93	Ma				
Plateau age = 233.4 ± 2.0 Ma			(2 σ , including J-error of .6%)		MSWD = 1.9, probability=0.085			Includes 69.5% of the 39Ar		steps 5 through 10		

Table 3-4. Continued.

Inverse isochron (correlation age) results, plateau steps: Model 1 Solution ($\pm 95\%$ -conf.) on 5 points	Age = 269 ± 11 Ma	older 5 steps
Initial $40\text{Ar}/36\text{Ar} = 381 \pm 180$	MSWD = 12.0	Probability = 0.00
<hr/>		
Inverse isochron (correlation age) results, plateau steps: Model 1 Solution ($\pm 95\%$ -conf.) on 8 points	Age = 234.3 ± 3.1 Ma	
Initial $40\text{Ar}/36\text{Ar} = 260 \pm 170$	MSWD = 2.3	Probability = 0.04
<hr/>		

3.7. Discussion

3.7.1. *Pressure-temperature constraints*

An idealized fluid inclusion isoplethic section was constructed based upon three-phase FIT final homogenization temperatures into the liquid and corresponding salinities (Knight et al., 1989, Bakker, 2003). As there are two co-existing fluid phases present in the Byrud emerald, and these are interpreted as conjugates of a boiling system, the pressure of entrapment can be determined from the measured homogenisation temperatures and salinities. The relatively consistent phase ratios and absence of observed halite-dominant three-phase FIT suggests the three phase fluid inclusions were not trapped in the vapour + halite or liquid + halite field (Figure 3-12) nor were these inclusions trapped on the liquid + vapour + halite curve. Therefore, the majority of the Byrud three-phase FIT were likely trapped in a one-phase or liquid only stability field or from the liquid-rich side of the liquid + vapour field for a 30.7 mass percent NaCl solution (Figure 3-12). Similarly, from fluid inclusion and petrographic observations, it can be reasoned that the two-phase FITs were trapped predominantly from the vapour-rich side of the liquid + vapour only stability field (Figure 3-12). Any of the observed fluid inclusions in our study could have been trapped within the medium-gray shaded region of Figure 3-12. Correspondingly no observed fluid inclusions (and microthermometric behaviour) are representative of fluid inclusion compositions from either the light or dark gray fields of figure 3-12. However, experimental data for the NaCl-H₂O system (Bodnar, 2003b) indicate the vapour phase of a 30.7 mass percent NaCl system has NaCl contents of less than 1 mass percent; though our vapour-rich fluid inclusions contain up to 7.6 mass percent NaCl. Thus we interpret the vapour dominant fluid inclusions as a trapped mixture of predominantly vapour with some brine. From microthermometry, the temperature conditions ranging from 161 °C and 383 °C ideally could be used in relation to halite melt temperatures to determine the pressure of entrapment of co-existing vapour and liquid phases of the boiling system. However, a dearth of experimental PVTX and solvi position data for a NaCl dominated brine and complex gas system as determined via the fluid inclusion work precludes the determination of pressures from coexisting temperature points on the solvi.

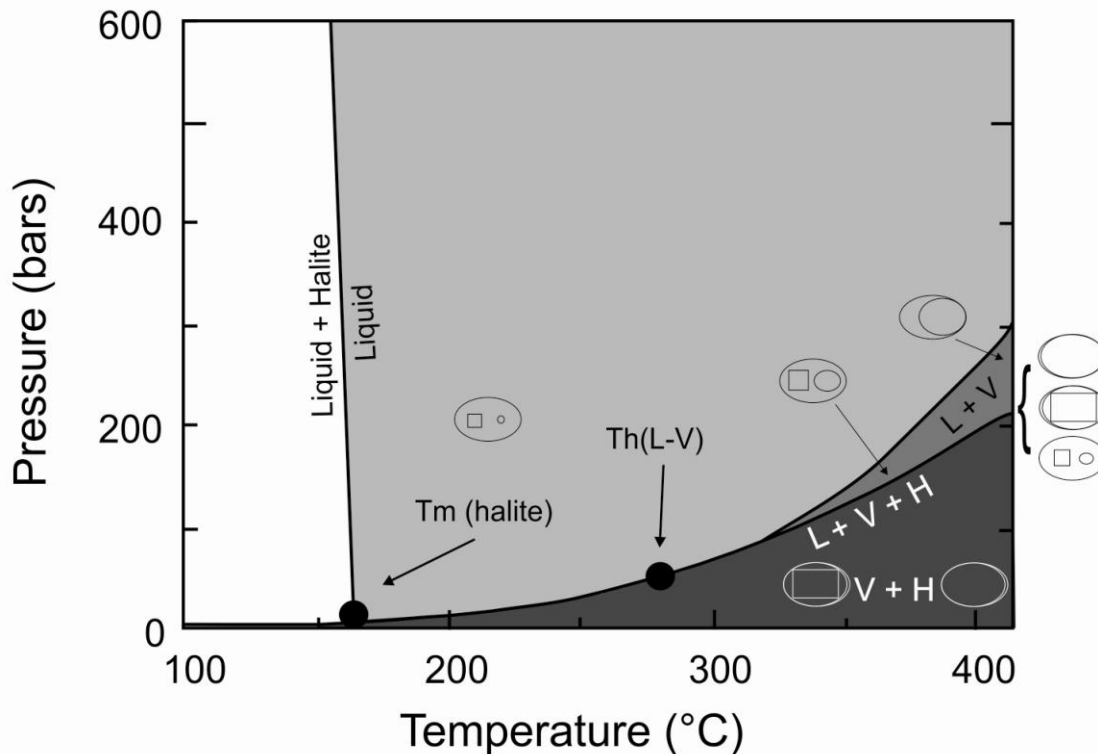


Figure 3-12. Pressure-temperature diagram showing the schematic constraints for the Byrud emerald veins derived from isochore constraints for a 30.7 weight percent NaCl fluid inclusions. Maximum pressure estimates from Anderson (1990) at 1000 bars. Liquidus and field boundaries for the 30.7 mass percent isopleth used for this study were interpolated from the data of Sourirajan and Kennedy (1962), Bodnar (2003b) and Atkinson (2002). T_m = melting temperature of halite. T_h = homogenization temperature.

Previous work (Andersen, 1990) studying the Oslo Paleorift determined that maximum Permo-Triassic fluid pressures for the Byrud area were approximately 1000 bars. Estimated pressures are derived from inferred solidus conditions of the nordmarkite magmas in the Oslo region through microthermometric work and a comparison with the local geology (Andersen, 1990). This is consistent with and supersedes our pressure constraints placed on the emerald mineralization based on andalusite crystals present in the shales proximal to the emerald veins. The presence of

andalusite limits regional pressures during emerald mineralization to below the aluminosilicate invariant point at 3800 bars. However, the lithostatic estimate from Anderson (1990) provides a more tightly constrained maximum pressure for the emerald mineralisation at Byrud, and therefore, we limit the temperatures of vein formation to between 160 °C and 385 °C based on our fluid inclusion study and limit the maximum pressure to below 1000 bars (Anderson, 1990).

The beryl-hosted fluid inclusions observed in this study are trapped both in the clear and green growth zones in some beryl/emerald crystals. These zones are petrographically related to the liquid-rich and vapour-rich portions of a boiling system and thus, indicate that both the liquid and the vapour portion of the boiling system were saturated with respect to beryl/emerald. Our petrographic observations of fluid inclusion compositions hosted within quartz (Figure 3-7) and in emerald (Figure 3-8) are also consistent with our proposed model of boiling as the mechanism for the colour zonation within the Byrud emerald. However, the absence of any growth zones within the quartz limits any applicability of microthermometric measurements of the quartz hosted fluid inclusions. Plots of the two fluid inclusions types within both quartz and emerald in temperature-salinity space do not align along any specific solvus as in Schmidt & Bodnar (2000). This is interpreted to reflect the dynamic environment that the emerald forms in. The banded pattern in the emerald is due to precipitation in either the liquid or vapour portions of a boiling system and therefore, the presence of the multiple bands are consistent with changing pressures in the emerald vein. This continual change in pressure is also consistent with the lack of agreeable solvus data alignment observed in the microthermometric data.

Limited sample material and $\delta^{18}\text{O}$ emerald, quartz, feldspar analyses from the Byrud deposit exclude a detailed discussion of the excessive temperatures obtained from quartz-beryl, feldspar-beryl oxygen isotope thermometry. The excessively high temperatures from $\delta^{18}\text{O}$ thermometry are likely due to our samples containing varying proportions of beryl and emerald from the zoned crystals. The grain and sample size for the $\delta^{18}\text{O}$ emerald analyses is limited to a few small grains and thus, it is difficult to determine colour and zoning in these small samples. Fortunately the sample size required for the channel fluid (δD) measurements is much larger and thus the channel fluid data likely are a mixture of fluids trapped within the different colour zones of a single

emerald crystal and are representative of an overall fluid composition and these data are thus more applicable to deposit genesis (Figure 3-10). However, it is still evident from the detailed fluid inclusion and emerald chemistry on the zonation within this emerald that the green bands within the studied crystals were precipitated from the liquid portion of a boiling system and that the clear zones were precipitated from the vapour portion of the boiling system (Figure 3-8).

3.7.2. Emerald mineralization model and classification

In most emerald deposits, emerald forms when chromium and/or vanadium ions diffuse from intruded country rock into a cooling Be⁺ rich pegmatitic body. This usually takes place near the boundary between the pegmatite and the intruded rock but in the pegmatite itself. Residual Be²⁺ in the pegmatitic solutions combines with Al, Si, and O to form common beryl (Groat et al., 2008). In the case of the Byrud emerald, the chromium and more specifically vanadium in the black shales/hornfels, substitute at the Al-site giving rise to emerald. Whole-rock geochemical analyses (Appendix B) show high concentrations of vanadium and chromium in the black shales/hornfels than the other host rocks. Electron microprobe analyses also show that the emerald is distinctly enriched in vanadium and substitution occurs at the aluminum site (Figure 4-2). The geologic source of vanadium in emerald is not well documented. Vanadium is usually concentrated in rocks that include iron-rich minerals or organic compounds (Moskalyk and Alfantazi, 2003). As shown in the geochemical analyses, the likely source of vanadium for the emerald is the black shale which is also rich in organic matter and sulphides. This source of vanadium at Byrud is comparable to the Colombian deposits and Lened in Canada, where it is the only other localities which vanadium is sourced from organic-rich black shales (Ottaway, 1994; Marshall et al., 2004; Campos et al., 2007). Studies on the valence state of V in emerald have yet to be accomplished, and it is unclear as to the state of V in the mineralising fluids. However, the role of vanadium in the colouration of emerald was affirmed through work completed by Wood and Nassau (1968), who examined emerald from Bahia, Brazil. They noted that the Cr present in the emerald was only 3 ppm and a large concentration of V was present as V³⁺ ions substituting at the octahedral Al³⁺ sites. Furthermore, the beryl crystals grown in the study by Wood and Nassau (1968) in lithium vanadate or vanadium oxide flux are

colorless and suggested that in both, the vanadium is V^{5+} , while in the beryl structure, only the V^{3+} ion is accommodated at the aluminum site (Sinkankas, 1981). The energy levels for V^{2+} , V^{4+} , and V^{5+} were also examined for octahedral coordination in the beryl structure in the samples studied (Wood and Nassau, 1868), however, their spectra did not resemble those collected from the V^{3+} , which gave the emerald its green colour.

A common classification scheme for emerald deposits is split between a Type 1 deposit related to granitic/pegmatitic intrusions and Type 2 deposits controlled by tectonic structures (Schwarz and Giuliani, 2001; Schwarz et al., 2001). Most emerald deposits fall in the first category and are subdivided on the presence or absence of schist at the contact zone. Type 2 deposits are subdivided into schists without pegmatites and black shales with veins and breccias (Schwarz and Giuliani, 2001; Schwarz et al., 2001). The Byrud emerald is categorized as a Type 1 deposit, whereas surrounding rocks are black shale/hornfels rather than schist. The most common example of emerald deriving chromium and vanadium chromophoric material from sediments is the world's largest and richest emerald deposit at Muzo, Colombia (Ottaway et al., 1994; Giuliani et al., 1995). However, based on the observed petrographic similarities between the fluid inclusions in the progenitor granite and occurrence of emerald in miarolitic cavities in the pegmatite, the geological environment at Byrud is interpreted as consistent with the typical Type 1 emerald deposit. Moreover, the colour banding is very similar to that observed at the Emmaville and Torrington pegmatite-related emerald deposits in Australia (Loughrey et al., 2012). As well, similar colour zonations have been identified in Namibia and South Africa. In Figure 3-6, there are distinct overlaps between the Byrud emerald and emerald from the Emmaville and Torrington, Delbegetey, and Kazakhstan deposits as they all present distinctly low magnesium and sodium values (Gravilenko et al., 2006; Loughrey et al., 2012). Both Byrud and the Emmaville-Torrington deposits share many other characteristics such as: (1) low concentrations of Na_2O and MgO , (2) formed in pegmatite sills which intrude black shale, (3) associated minerals include quartz, feldspars, micas, fluorite, topaz, cassiterite, wolframite, and arsenopyrite, (4) similar pressures and temperatures of formation, and (5) presence of both vapour-dominant and halite bearing fluid inclusions (Rondeau et al., 2008; Loughrey et al., 2012). The main difference between the two

deposits is the Byrud deposit contains more vanadium than chromium, and CH₄, N₂, and H₂S gases in the fluid inclusions.

3.8. Conclusions

The Byrud emerald deposit is a Type 1 emerald deposit, hosted within pegmatite intruding graphite- and sulphide-rich black shale/hornfels. This sedimentary sequence is the source of vanadium and to a lesser extent chromium, based on whole rock geochemical analyses, fluid inclusion data, and stable isotopes analyses. The V and Cr interacted with the beryllium, supplied by the pegmatite to form emerald. ⁴⁰Ar-³⁹Ar evidence from muscovite from the pegmatite is consistent with a Middle Triassic age for the emerald-bearing veins. Microprobe analyses show increases in vanadium in the emerald zones of zoned emerald-beryl crystals. Detailed fluid inclusion studies constrain formational temperatures from 160 °C to 385 °C and regional studies limit pressures to a maximum of 1000 bars. The fluid inclusion data and Raman studies limit fluid compositions to an average value of 30.7 mass percent NaCl equivalent with mole fractions of CO₂, N₂, CH₄, and H₂S in the gas phases on the order of 0.8974, 0.0261, 0.0354, and 0.0410, respectively. Stable isotope channel waters from the emerald sample confirms genesis from a mixture of magmatic and metamorphic fluids.

The two FITs observed in the Byrud emerald are petrographically contemporaneous with the zoned emerald from this study based on petrographic relationships between growth zones and fluid inclusions. Emerald crystals from the Byrud deposits display the distinctive emerald banding which is due to emerald/beryl growth in the liquid and vapour portions, respectively, of a boiling system. Additionally, these two FITs represent conjugates of this two-phase system as they were observed in the green and clear zones within one of the zoned crystals. Zoned emerald are markedly different from the more-typical non-zoned or single coloured emerald precipitated from a homogenous fluid source.

3.9. Acknowledgements

The isotopic work by Kerry Klassen of QFIR Stable Isotope Lab at Queen's University is gratefully acknowledged. This study benefitted greatly from samples and field assistance provided by Arnfinn Juliussen. Samples donated by Fred Steinar Nordrum of the Norsk Bergverksmuseum in Kongsberg and Bjorn Skår of Norsk Naturafeln were instrumental in determining fluid timing relationships. Access to the Byrud Mine by the current owners, Anne-Greta Røssa and Ole Jørgen Bjørnstad, is also gratefully acknowledged.

References

- Anderson, T. (1990). Melt-mineral-fluid interaction in Peralkaline Silicic intrusions in the Oslo Rift, Southeast Norway. IV: fluid inclusions in the Sande nordmarkite. *Norges Geologiske Undersøkelse*, **417**: 41–54.
- Atkinson, A.B. (2002). A model for the PTX properties of H₂O-NaCl. MSc thesis, Virginia Polytechnic Institute and State University, USA.
- Bakker, R.J. (2003). Package FLUIDS 1. Computer programs for analysis of fluid inclusion data and for modelling bulk fluid properties. *Chemical Geology*, **194**: 3–23.
- Bodnar, R.J. (2003a). Introduction to fluid inclusions, in Samson, I., Anderson, A. and Marshall, D., eds., *fluid Inclusions: analysis and interpretation: short course*. Mineralogical Association of Canada, **32**: 1–8.
- Bodnar, R.J. (2003b). Introduction to aqueous-electrolyte fluid inclusions, in Samson, I., Anderson, A. and Marshall, D., eds., *fluid Inclusions: analysis and interpretation: short Course*. Mineralogical Association of Canada, **32**: 81–100.
- Burke, E.A.J. (2001). Raman microspectrometry of fluid inclusions. *Lithos*, **55**: 139–58.
- Campos, Alvarez N.O., and Roser, B.P. (2007). Geochemistry of black shales from the Lower Cretaceous Paja Formation, Eastern Cordillera, Colombia: source weathering, provenance, and tectonic setting. *Journal of South American Earth Sciences*, **23**: 271–89.
- Dhamelincourt, P., Beny, J.M., Dubessy, J.C., and Poty, B. (1979). Analysis of fluid inclusions with the Mole Raman microprobe. *Bulletin de Mineralogie*, **102**: 600–10.
- Faul, H., Elmore, P.L.D., and Brannock, W.W. (1959). Age of the Fen carbonatite (Norway) and its relation to the intrusive of the Oslo Region. *Geochimica et Cosmochimica Acta*, **17**: 153–6.
- Giuliani, G., Cheilletz, A., Arboleda, C., Carrillo, V., Rueda, F., and Baker, J.H. (1995). An evaporitic origin of the parent brines of Colombian emeralds: fluid inclusion and sulphur isotopic evidence. *European Journal of Mineralogy*, **7**, 151–65.
- Giuliani, G., France-Lanord, C., Zimmerman, J.L., Cheilletz, A., Arboleda, C., Charoy, B., Coget, P., Fontan, F., and Giard, D. (1997). Fluid composition, dD of channel H₂O and d18O of lattice oxygen in beryls: genetic implications for Brazilian, Colombian, and Afghanistani emerald deposits. *International Geology Review*, **39**: 400–24.

- Giuliani, G., France-Lanord, P., Coget, D., Schwarz, A., Cheilletz, Y., Branquet, D., Giard, A., Martin-Izard, P., Alexandrov, P., and Piat, D.H. (1998). Oxygen isotope systematic of emerald: relevance of its origin and geological significance. *Mineralium Deposita*, **31**: 513–9.
- Goldstein, R. (2003). Petrographic analysis of fluid inclusions, In: *Fluid Inclusions: Analysis and Interpretation: Short Course*. (eds Samson I, Anderson A, Marshall D), Mineralogical Association of Canada, Nepean, ON, **32**: 9–53.
- Gravilenko, E.V., Calvo, P.B., Castroviejo, B.R., and Garcia del Amo, D. (2006). Emeralds from the Delbegetey deposit (Kazakhstan): mineralogical characteristics and fluid-inclusion study. *Mineralogical Magazine*, **70**: 159–73.
- Groat, L., Giuliani, G., Marshall, D., and Turner, D. (2008). Emerald deposits and occurrences: a review. *Ore Geology Reviews*, **34**: 87–112.
- Ihlen, P.M. (1978). Ore deposits in the north-eastern part of the Oslo region and in the adjacent Precambrian areas. *NATO Advanced Study Institutes Series. Series C: Mathematical and Physical Sciences*. **36**: 277–86.
- Ihlen, P.M., Ineson, P.R., and Mitchell, J.G. (1977). K/Ar dating of clay mineral alteration associated with ore deposition in the northern part of the Oslo region. *NATO Advanced Study Institutes Series. Series C: Mathematical and Physical Sciences*. **36**: 255–63.
- Ineson PR, Mitchell JG, Vokes FM (1975) K-Ar Dating of epigenetic mineral deposits: an investigation of the Permian Metallogenic Province of the Oslo Region, Southern Norway. *Economic Geology*, **70**, 1426–36.
- Ineson, P.R., Mitchell, J.G., and Vokes, F.M. (1978). Further K/Ar determinations of clay mineral alteration associated with fluorite deposition in Southern Norway. In: *Petrology and Geochemistry of Continental Rifts* (eds Neuman ER, Ramberg IB), **1**, pp.265–75. NATO Science Series, Norwell, MA.
- Kazmi, A.H., and Snee, L.W. (1989). Geology of the world emerald deposits: a brief review. In: *Emeralds of Pakistan* (eds Kazmi AH, Snee LW), pp. 165–228. Van Nostrand Reinhold, New York, NY.
- Knight, C.L., and Bodnar, R.J. (1989). Synthetic fluid inclusions: IX. Critical PVTX properties of NaCl-H₂O solutions. *Geochimica Cosmochimica Acta*, **53**: 3–8.
- Larsen, B.T., and Sundvoll, B. (1984). The Oslo Graben: A Passive High Volcanicity Continental Rift: *EOS* **65**, **45**: 1084.
- Larsen, B.T., Olaussen, S., Sundvoll, B., and Heeremans, M. (2008). The Permo-Carboniferous Oslo Rift through six stages and 65 million years. *Episodes*, **31**: 52–8.

- Loughrey, L., Marshall, D., Jones, P., Millsteed, P., and Main, A. (2012). Pressure-temperature-fluid constraints for the Emmaville-Torrington emerald deposit, New South Wales, Australia: fluid inclusion and stable isotope studies. *Central European Journal of Earth Sciences*, **4**: 287–99.
- Marshall, D., Groat, L.A., Falck, H., Giuliani, G., and Neufeld, H. (2004). The Lened emerald prospect, Northwest Territories, Canada; insights from fluid inclusions and stable isotopes, with implications for Northern Cordilleran emerald. *Canadian Mineralogist*, **42**: 1523-1539.
- Matsuhisa, Y., Goldsmith, J.R., and Clayton, R.N. (1979). Oxygen isotopic fractionation in the system quartz-albite-anorthite-water. *Geochimica et cosmochimica acta*, **43**: 1131–40.
- Moskalyk, R.R., and Alfantazi, A.M. (2003). Processing of vanadium: a review. *Minerals Engineering*, **16**: 793–805.
- Negro, F., de Sigoyer, J., Goffe, B., Saddiqi, O., and Villa, I.M. (2008). Tectonic evolution of the Betic-Rif arc: new constraints from $^{40}\text{Ar}/^{39}\text{Ar}$ dating on white micas in the Tamsamane units (External Rif, northern Morocco). *Lithos*, **106**: 93–1009.
- Neumann, H. (1960). Apparent ages of Norwegian minerals and rocks. *Norsk Geological Tidsskriftet*, **40**: 173–91.
- Nier, A.O. (1939). The isotopic composition of radiogenic lead and the measurement of geological time, II. *Physical Review*, 2nd ser., **55**: 153–63.
- Nordrum, F.S., and Raade, G. (2006). Das Smaragd-Vorkommen von Byrud (Eidsvoll) in S€ud-Norwegen [The emerald deposit at Byrud (Eidsvoll) in South Norway]. *Mineralien-Welt*, **17**, **4**: 52–64 [in German].
- Olerud, S., and Ihlen, P. (1986). Metallogeny associated with the Oslo paleorift. *Sveriges Geologiska Undersokning, Serie Ca: Avhandlingar och Uppsatser I A4*, **59**: 1–17.
- O’Neil, J.R., and Taylor, H.P. Jr. (1967). The oxygen isotope and cation exchange chemistry of feldspars. *American Mineralogist*, **52**: 1414–37.
- Ottaway, T.L., Wicks, F.J., Bryndzia, L.T., Keyser, T.K., and Spooner, E.T.C. (1994). Formation of the Muzo hydrothermal emerald deposit in Colombia. *Nature*, **369**: 552–4.
- Ramberg, I.B., and Larsen, B.T. (1978). Tectonomagmatic evolution, In: *The Oslo Paleorift*. (eds Dons JA, Larsen BT), *Norges Geologiske Undersøkelse*, **337**: 55–73.
- Renne, P.R., Swisher, C.C. III, Deino, A.L., Karner, D.B., Owens, T., and DePaolo D.J. (1998). Intercalibration of standards, absolute ages and uncertainties in $^{40}\text{Ar}/^{39}\text{Ar}$ dating. *Chemical Geology*, **145**: 117–52.

- Rondeau, B., Fritsch, E., Peucat, J.J., Nordrum, F.S., and Groat, L. (2008). Characterization of Emeralds from a historical deposit: Byrud (Eidsvoll), Norway. *Gems & Gemology*, **44**: 108–22.
- Schmidt, C., and Bodnar, R.J. (2000). Synthetic fluid inclusions: XVI. PVTX properties in the system H₂O-NaCl-CO₂ at elevated temperatures, pressures, and salinities. *Geochimica et Cosmochimica Acta*, **64**: 3853–69.
- Schwarz, D. (1991). Die chemischen Eigenschaften der Smaragde; II, Australien und Norwegen. *Zeitschrift der Deutschen Gemmologischen Gesellschaft*, **40**: 39–66.
- Schwarz, D., and Giuliani, G. (2001). Emerald deposits – A review. *The Australian Gemmologist*, **21**: 17–23.
- Schwarz, D., Giuliani, G., Grundmann, G., and Glas, M. (2001). Die Entstehung der Smaragde, ein vieldiskutiertes Thema, ExtraLapis. In: Smaragd, der Kostbarste Beryll, der Teuerste Edelstein (eds Schwarz D, Hochleitner R), 21, pp. 68–73. ExtraLapis, Munich, Germany.
- Sinkankas, J. (1981). Emeralds and other beryls. pp. 665. Chilton Book Co, Radnor, Pa.
- Sourirajan, S., and Kennedy, G.C. (1962). The system H₂O-NaCl at elevated temperatures and pressures. *American Journal of Science*, **260**: 115–141.
- Sundvoll, B., Neumann, E.R., Larsen, B.T., Tuen, E. (1990). Age relations among Oslo Rift magmatic rocks; implications for tectonic and magmatic modelling. *Tectonophysics*, **178**: 67–87.
- Taylor, R.P., Fallick, A.E., and Breaks, F.W. (1992). Volatile evolution in Archean rare-element granitic pegmatites: evidence from the hydrogen-isotopic composition of channel H₂O in beryl. *The Canadian Mineralogist*, **30**: 877–93.
- Wood, D.L., and Nassau, K. (1968). Characterization of beryl and emerald by visible and infrared absorption spectroscopy. *The American Mineralogist*, **53**: 777–800.
- Wopenka, B., and Pasteris, J.D. (1987). Raman Intensities and Detection Limits of Geochemically Relevant Gas Mixtures for the Laser Raman Microprobe. *Analytical Chemistry*, **59**: 2165–70.
- Xue, G., Marshall, D., Zhang, S., Ullrich, T., Bishop, T., Groat, L., Thorkelson, D., Giuliani, G., and Fallick, A. (2010). Conditions for Early Cretaceous emerald formation at Dyakou, China: fluid Inclusion, Ar-Ar, and stable isotope studies. *Economic Geology*, **105**: 375–94.
- Zheng, Y.F. (1993a). Calculation of oxygen isotope fractionation in anhydrous silicate minerals. *Geochimica et Cosmochimica Acta*, **57**: 1079–91.

4. Additional Research and Deposit Model

4.1. Introduction

Additional research is presented in this chapter that was not included in the submitted journal article in *Geofluids*. Further electron microprobe analyses conducted at the University of British Columbia (Appendix D) complement the probe work presented in that paper. The relationship between the major elements (V, Cr and Fe) reflects substitution at the octahedral sites of the beryl structure. These additional results are consistent with previous work in Chapter 3 and are included here to complement the findings in the paper.

The Byrud emerald have some of the lowest sodium values. Previous researchers have defined a relationship between Na concentrations and the amount of channel water within emerald (Guiliani et al., 1997; Zimmerman et al., 1997). In this chapter, the new Na and H₂O concentrations from the Byrud emerald are compared to a variety of emerald deposits and an improved model for the predication of H₂O in emerald presented.

Lastly the formation of colour zonation observed in the Byrud emerald is examined in greater detail. A model of the movement of the liquid-vapour interface within a vein precipitating emerald is developed and the applicability of the boiling model to other zoned emerald localities discussed.

4.2. Electron microprobe analyses and prediction of H₂O content in emerald

Electron microprobe analyses were conducted along set traverses perpendicular to the *c* axis of two of the samples and parallel to the *c* axis of a third sample. The

traverses were also selected perpendicular to colour zoning. The zoning was imaged via cathodoluminescence (CL) and compared to the electron microprobe data for the major chromophoric oxides of Cr, V, and Fe across a number of growth zones in the three crystals (Figures 4-1 and 4-2). The growth zones perpendicular to the crystal's *c* axis are clearly delineated in the CL images, where the dark bands correspond to colourless beryl, and the lighter bands correlate to the green bands of emerald. There is a reasonable correlation between Cr, V, and Fe concentrations, and in general these elements substitute for Al in beryl. Since substitution occurs at the Y site in the crystal structure of beryl, the variations in colour are attributed to complicated substitutions at this site and/or slight variations in fluid composition. The values of V₂O₃, Cr₂O₃, and Fe₂O₃, range up to 1.875, 0.401, 0.339 mass percent respectively. A decrease in Al content from the colourless to green zone in sample LEL12-veinB-1 (Figure 4-2), is coupled with a general increase in the minor chromophoric elements, V, Cr, and Fe. This inverse pattern is consistent with substitution of these elements for Al in the octahedral site. The values for MgO and Na₂O are extremely low for the Byrud emerald and may be considered an additional characteristic property of the deposit. These low values are quite similar to the Emmaville and Torrington emerald deposit in Australia (Loughrey et al., 2012) and emeralds from Delbegetey, Kazakhstan (Gravilenko et al., 2006).

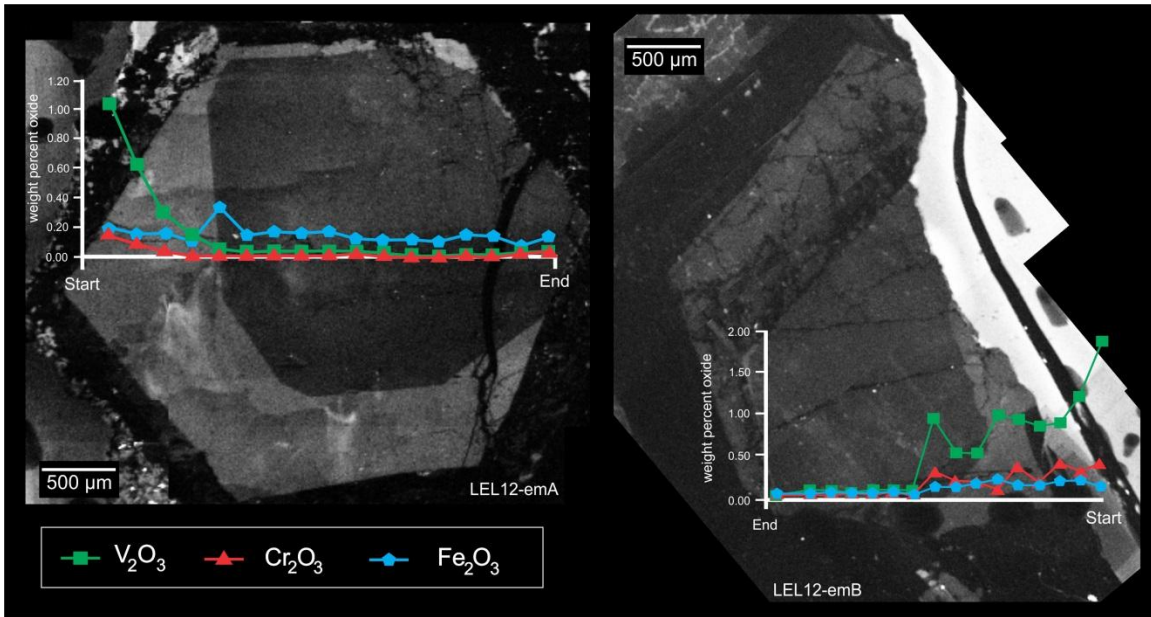


Figure 4-1. Mass percent oxide data for selected oxides in emerald along a microprobe traverse (thick horizontal white line). The photomicrographs are two of the three zoned emerald crystals taken in CL. Electron microprobe analyses points are equally spaced (tick marks) from left to right in sample LEL12-emA and right to left in LEL12-emB. Corresponding analyses in Appendix D.

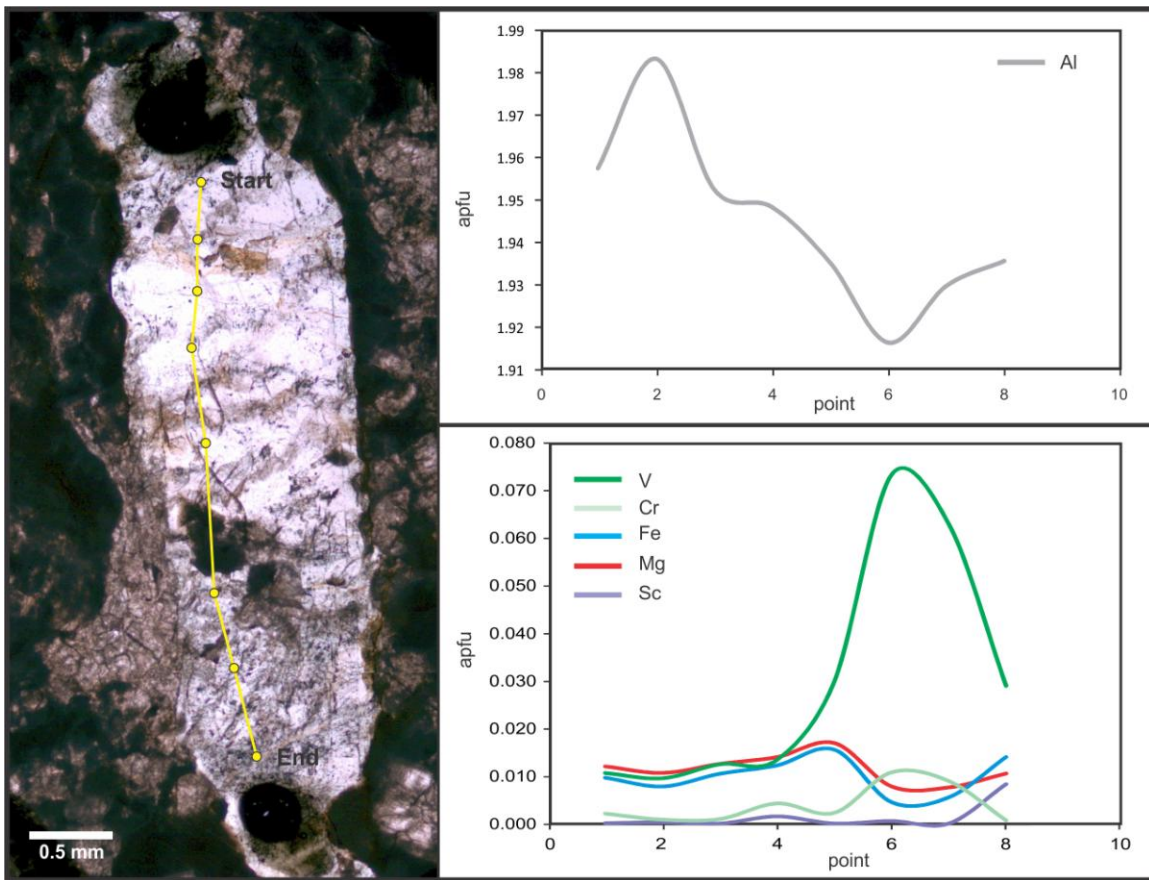


Figure 4-2 Photomicrograph of emerald crystal, sample LEL12-veinB-1, in plane polarized light showing a faint transition from colourless beryl to green emerald from one end of the crystal to the other. The image is compared to traverse points in element plots for Al and minor elements V, Cr, Fe, Mg and Sc (in atoms per formula unit, apfu).

Previous mass-spectrometric studies of fluids trapped within the channels in beryl and within fluid inclusions have been used to characterize the quantitative and qualitative compositions of fluids within emerald (Guiliani et al., 1997; Zimmerman et al., 1997). Water within the structural channels of emerald has been characterized as Type I and Type II, based on the orientation of the water molecule within the *c* axis (Wood and Nassau, 1967). The Type I water is free of alkalis and unbonded. Type II water is coordinated to alkali cations: Na^+ , K^+ , Rb^+ and Cs^+ with two water molecules bonded to a Na^+ ion. Depending on the concentration of Na^+ , enrichment in molecular H_2O can be

predicted. Giuliani et al. (1997) and Zimmerman et al. (1997) fit existing data to the equation:

$$\text{H}_2\text{O} = 0.84958 \times \text{Na}_2\text{O} + 0.8373 \quad (4-1)$$

with H_2O and Na_2O measured in mass%.

The very low water contents of 1.1 to 1.2 mass% (Table 4-1) measured in this study are similar to the value of 1.1 mass% described by Alexandrov et al. (2001). These are some of the lowest water contents documented for emerald from any source (Schwarz, 1987). Correspondingly the Byrud emerald measured in this study also have very low Na_2O contents. These new Byrud data have been combined with all existing literature data (Figure 4-3) and are best defined by the relationship:

$$\text{H}_2\text{O} = 0.5477 \ln \text{Na}_2\text{O} + 2.182 \quad (4-2)$$

with H_2O and Na_2O measured in mass%.

This new equation extends the prediction of H_2O contents from Na_2O concentrations to lower values, such as those observed at Byrud. Additionally this new equation trends towards the theoretical minimum of zero values for both H_2O and Na_2O .

Table 4-1. Channel H₂O and Na₂O contents (mass %) of various emerald deposits worldwide¹

Locality	H ₂ O channels (mass %)	Na ₂ O emerald (mass %)	Locality	H ₂ O channels (mass %)	Na ₂ O emerald (mass %)
Colombia			Emmaville-Torrington	0.83	0.07
Yacopi	2.19	0.77	Canada		
Pava	1.63	0.31	Mountain River	2.4	1.68
Coscuez	1.76	0.47	Mountain River	2.4	1.71
Tequendama	1.8	0.57	Tsa da Glisza	2.07	1.06
Cincho	1.73	0.45	Tsa da Glisza	1.91	0.92
Vega	1.36	0.24	Lened	2.04	0.93
Oriente	1.35	0.25	Lened	1.98	0.91
Palo Aranado	1.45	0.31	Lened	1.92	0.91
Guala	1.45	0.22	Lened	1.84	0.89
Klein	1.45	0.27	Lened	1.94	0.88
Brazil			China		
Carnaíba	2.37	1.24	Davdar	2.1	0.8
Santa Terezinha	2.88	2.02	Davdar	2.3	0.79
Norway			Dyakou	2.9	1.34
Byrud	1.1	0.15	Dyakou	2.7	1.34
Byrud	1.1	0.2	South Africa		
Byrud	1.1	0.11	Ledysorp	2.45	2.46
Byrud	1.2	0.17	Pakistan		
Australia			Khaltaro	2.12	0.92
Emmaville-Torrington	0.87	0.08			

¹Concentrations of H₂O obtained by stable isotope analyses and quadrupolar mass spectrometry. Na₂O contents obtained by microprobe analysis on an SX-50 CAMECA microprobe. Data compiled from this study and other data from the literature, Loughrey et al. (2012), Hewton et al. (2012), Marshall et al. (2012), Xue et al. (2010), Groat et al. (2008), Marshall et al. (2004), Neufeld (2004), Zimmerman et al. (1997), Giuliani et al. (1997), Hammarstrom (1989), Grundmann and Morteani (1989).

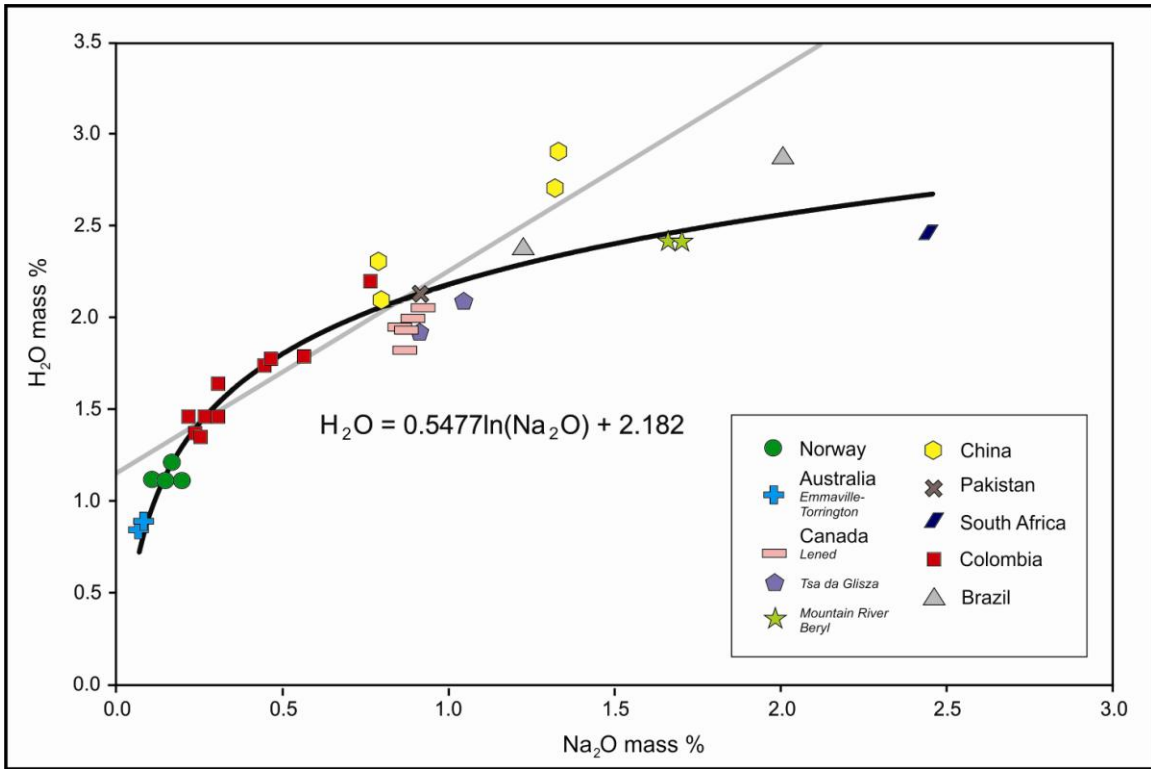


Figure 4-3. Channel H_2O versus emerald Na_2O contents for a variety of emerald deposits. For comparison to the new fit, the previously derived equation of Giuliani et al., 1997 is shown in gray. The R^2 value for the new fit is 0.8923.

4.3. Deposit Model and Comparison to Other Zoned Emerald Deposits

Byrud is a unique emerald occurrence with the highest concentrations of vanadium in emerald worldwide. The Byrud deposit is categorized as a Type 1 deposit (Schwarz et al., 2001; Schwarz et al., 2001), without schist at the contact zone, but rather black shales. The geological environment at Byrud resembles the Emmaville-Torrington deposit; however the Byrud host rocks are shales. Although not common, shales have been documented as host rocks to a number of Type 1 emerald deposits. The Norwegian and Emmaville/Torrington emerald deposits share many similarities in that the deposits contain: (1) low concentrations of H_2O , Na_2O and MgO , (2) pegmatite

which intrudes host rocks, (3) associated minerals quartz, feldspars, micas, fluorite, topaz, cassiterite, and wolframite, (4) strong colour zonations parallel to the basal plane, and (5) both vapour-dominant and halite bearing fluid inclusions (Rondeau et al., 2008; Ventalon et al., 2009; Loughrey et al., 2012; Loughrey et al., 2013). The main difference between the two is the Emmaville/Torrington deposits contains more chromium than vanadium and the Byrud deposit has minor amounts of CH₄ in the fluid inclusions (Figure 3-9).

The similar phenomenon of emerald banding is observed in emerald from the Erongo Mountains, Namibia (Pirajno, 1990; Wigand et al., 2004; Gentry et al., 2004). The growth zones in the Erongo emerald are similar to the Byrud and Emmaville-Torrington emerald with a sharp contact between a dark region (emerald) and a lighter region (beryl) (Figure 4-4). Zoned emerald also have been observed at the Swat Valley emerald deposit in Pakistan, Kafubu deposit in Zambia, and the Leydsdorp deposit in South Africa. The crystals from the Swat emerald locality are not homogeneous, but many display similar colour zoning to Byrud. The emerald display colourless core surrounded by emerald and as well as alternating colourless beryl to emerald zones (Hammerstrom, 1989). At the Leydsdorp deposit in South Africa, colour banded emerald have also been observed (Grundmann and Morteani, 1989). The characteristics of these deposits with zoned emerald are very similar to Byrud with the exception that the Byrud emerald is dominantly coloured by V as opposed to Cr.



Figure 4-4. Colour zonations parallel to the basal pinacoid from dark green (emerald) to light blue to colourless beryl. Sample from the Erongo deposit, Namibia. Scale bar in centimetres.

The boiling model derived for the formation of emerald colour zonation at Emmaville/Torrington was assessed as a model to explain similar textures at the Byrud deposit. The formation of the observed colour zones in the Byrud emerald are related to the activity of vanadium and $\pm\text{Cr}$ partitioning during different phases in a conjugate two-phase boiling system. The green bands in these crystals are a result of V ($\pm\text{Cr}$) ions partitioning into the liquid phase of a boiling system. The two phase FITs observed in the colourless beryl zones indicate beryl precipitation from a low-salinity vapour phase relatively depleted in V ($\pm\text{Cr}$). Conjugately, the three-phase FITs present within the green emerald zones are consistent with the precipitation of emerald in a high saline liquid portion of the boiling system, ultimately trapping the liquid-rich three-phase fluid inclusions. Increased activity of V and Cr within the liquid portion of the boiling system is indicated by the elevated concentrations of vanadium and chromium in the green zones. This relationship indicates the liquid-vapour interface dropped, and the space previously occupied by the liquid portion of the system would be primarily within the vapour field (Figure 4-5).

The correlation of high salinity fluid inclusions associated with V-rich beryl (emerald) is consistent with V being transported as a chloride complex in the beryl saturated pegmatite-related fluids. Vanadium bearing species in hydrothermal fluids include: VCl_2 , VCl_3 , VCl_5 , VF_2 , VF_3 , VF_5 , VO_2 , VCl_3O , and VF_3O (Churakov, 2001). In all likelihood the chloride species will dominate in the liquid portion of a boiling system with the fluorine and oxygen bearing species becoming more prevalent in a vapour phase. Thus, the oxidation of V (and hence its solubility) in the vapour versus the liquid portions of the boiling system may play some role in the colour zonations. However, there are no published experimental data with measured V concentrations from the conjugate fluids of a boiling system and thus it is impossible to evaluate whether a change in the oxidation state of V may also drastically change its solubility within a fluid and contribute to colour banding within emerald or other minerals.

Petrographic observations of fluid inclusion compositions hosted in quartz are also similar to those observed in emerald. Consistent with the proposed model of boiling for the colour zonation, the quartz hosted two-phase vapour-rich and three-phase highly saline fluid inclusions are interpreted to represent the two fluid endmembers and potential mixtures observed in the emerald. Due to the lack of growth zones in the quartz and fluorite, the applicability of the microthermometric measurements obtained in this study are limited and can only be based on the similarity of the fluid inclusion compositions and microthermometry of the two FITs, each observed in the quartz, fluorite, and zoned emerald. Additional microthermometric data for fluorite is supplied in Appendix C.

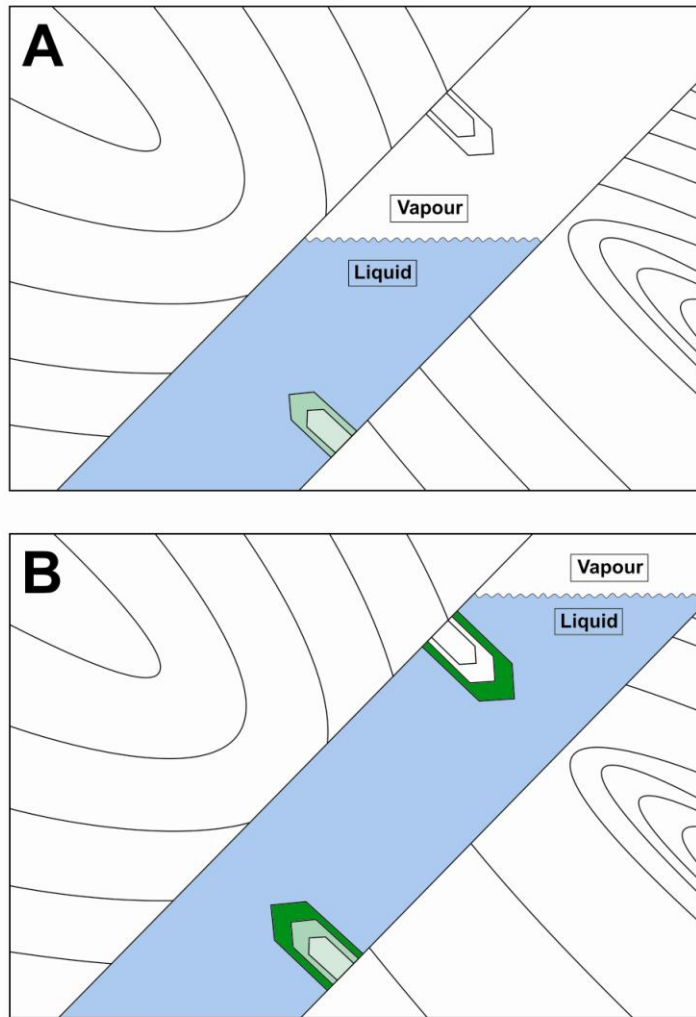


Figure 4-5. Schematic diagram showing the relationship of co-existing liquid and vapour phases of a saline fluid within a vein/fracture system A) represents conditions where a beryl (white) growth zone is precipitating from the vapour portion of the fluid in the upper parts of the vein and emerald (green) growth zones are precipitating from the liquid phase in the lower portion of the vein B) represents changing condition where the liquid-vapour interface has risen within the vein system, and the emerald (dark green) growth zones are precipitating on both crystals. As the liquid-vapour interface within the vein system ascends and descends, the crystals will have new growth zones of emerald or colourless beryl precipitated, depending upon whether precipitation occurs from the liquid or vapour respectively (modified from Loughrey et al., 2012).

References

- Alexandrov, P., Giuliani, G., and Zimmermann, J.L. (2001). Mineralogy, age and fluid geochemistry of the Rila emerald deposit, Bulgaria. *Economic Geology*, **96**: 1469–1476.
- Churakov, S. (2001). Physical-chemical properties of complex natural fluids. Unpublished PhD thesis. Berlin Technical University, Berlin, Germany.
- Gentry, R.M., Wise, M.A., and Pierro, R.C. (2004). Pocket Paragenesis of the Erongo Pegmatites, Namibia. *Rocks & Minerals*, **79**: 186-189.
- Gravilenko, E.V., Calvo, P.B., Castroviejo, B.R., and Garcia del Amo, D. (2006). Emeralds from the Delbegetey deposit (Kazakhstan): mineralogical characteristics and fluid-inclusion study. *Mineralogical Magazine*, **70**: 159–73.
- Giuliani, G., France-Lanord, C., Zimmerman, J.L., Cheilletz, A., Arboleda, C., Charoy, B., Coget, P., Fontan, F., and Giard, D. (1997). Fluid composition, dD of channel H₂O and d18O of lattice oxygen in beryls: genetic implications for Brazilian, Colombian, and Afghanistani emerald deposits. *International Geology Review*, **39**: 400–24.
- Groat, L., Giuliani, G., Marshall, D., and Turner, D. (2008). Emerald deposits and occurrences: a review. *Ore Geology Reviews*, **34**: 87–112.
- Grundmann, G. and Morteani, G. (1989). Emerald mineralization during regional metamorphism; the Habachtal (Austria) and Leydsdorp (Transvaal, South Africa) deposits, *Economic Geology*, **84**: 1835-1849.
- Hammarstrom, J.M. (1989). Mineral chemistry of emeralds and associated minerals from Pakistan and Afghanistan: an electron microprobe study. *In Emeralds of Pakistan: Geology, Gemology and Genesis* (A.H. Kazmi & L.W. Snee, eds.) pp. 125-500, Van Nostrand Reinhold Company, New York, N.Y.
- Hewton, M. (2012). Investigation of the Mountain River beryl (emerald variety) occurrence, Mackenzie Mountains, Northwest Territories, MSc Thesis. Simon Fraser University, British Columbia, Canada.
- Loughrey, L., Marshall, D., Jones, P., Millsted, P., and Main, A. (2012). Pressure-temperature-fluid constraints for the Emmaville-Torrington emerald deposit, New South Wales, Australia: fluid inclusion and stable isotope studies. *Central European Journal of Earth Sciences*, **4**: 287–99.
- Marshall, D., Pardiou, V., Loughrey, L., Jones, P., and Xue G. (2012). Conditions for emerald formation at Davdar, China; fluid inclusion, trace element and stable isotope studies. *Mineralogical Magazine*, **76**: 213-226.

- Marshall, D.D., Groat, L.A., Falck, H., Giuliani, G., and Neufeld, H. (2004). The Lened emerald prospect, Northwest Territories, Canada; insights from fluid inclusions and stable isotopes, with implications for Northern Cordilleran emerald. *Canadian Mineralogist*, **42**: 1523-1539.
- Neufeld, H. (2004). The Tsa Da Glisza (Regal Ridge) emerald occurrence, Southeastern Yukon Territory, Canada: descriptive, genetic, and exploration models. MSc thesis. University of British Columbia, Vancouver, Canada.
- Pirajno, F. (1990). Geology, geochemistry, and mineralisation of the Erongo Volcanic Complex, Namibia. *S. Afr. J. Geol.*, **93**: 485-504.
- Rondeau, B., Fritsch, E., Peucat, J.J., Nordrum, F.S., and Groat, L. (2008). Characterization of Emeralds from a historical deposit: Byrud (Eidsvoll), Norway. *Gems & Gemology*, **44**: 108–22.
- Schwarz, D., and Giuliani, G. (2001). Emerald deposits – A review. *The Australian Gemmologist*, **21**: 17–23.
- Schwarz, D. (1991). Die chemischen Eigenschaften der Smaragde; II, Australien und Norwegen. *Zeitschrift der Deutschen Gemmologischen Gesellschaft*, **40**: 39–66.
- Schwarz, D. (1987). Esmeraldas: Inclusões em Gemas [Emeralds: Inclusions in Gems]. *Imprensa Universitaria Universidad Federal de Ouro Preto*, pp.439, Ouro Preto, Brazil.
- Ventalon, S., Dubois, M., Rondeau, B., and Régnier, S. (2009). Mineralising fluid properties of the emerald deposit of Byrud, Norway. *European Current Research on Fluid Inclusions (ECROFI XX)*, Granada, Spain, 273-274.
- Wigand, M., Schmitt, A.K., Trumbull, R.B., Villa, I.M., and Emmermann, R. (2004). Short-lived magmatic activity in an anorogenic subvolcanic complex: $^{40}\text{Ar}/^{39}\text{Ar}$ and ion microprobe U-Pb zircon dating of the Erongo, Damaraland, Namibia. *Journal of Volcanology and Geothermal Research*, **130**: 285-305.
- Wood, D.L., and Nassau, K. (1967). Infrared spectra of foreign molecules in beryl. *Journal Chem. Phys.*, **47**: 2220-2228.
- Xue, G., Marshall, D., Zhang, S., Ullrich, T., Bishop, T., Groat, L., Thorkelson, D., Giuliani, G., and Fallick, A. (2010). Conditions for Early Cretaceous emerald formation at Dyakou, China: fluid Inclusion, Ar-Ar, and stable isotope studies. *Economic Geology*, **105**: 375–94.
- Zimmermann, J.L., Giuliani, G.G., Cheilletz, A.A., and Arboleda, C.C. (1997). Mineralogical significance of fluids in channels of Colombian emeralds; a mass-spectrometric study. *International Geology Review*, **39**: 425-437.

5. Conclusions

Emerald mineralization at the Byrud deposit is hosted within pegmatite and aplite veins intruding black shales/hornfels. This sedimentary sequence is the source of vanadium and chromium which interacts with beryllium supplied by the pegmatite and aplite dykes via an exsolving fluid. A Middle Triassic age for the emerald-bearing veins was determined from ^{40}Ar - ^{39}Ar analyses on muscovite. Microprobe analyses determined that increases in vanadium and chromium content are observed in the emerald zones of the crystals. New data from Byrud was combined with existing literature data relating the concentration of Na^+ and channel H_2O content, and is defined by the equation: $\text{H}_2\text{O} = 0.5477 \text{ In Na}_2\text{O} + 2.182$. The fluid inclusion studies provided information on the temperature and pressure conditions for emerald mineralization from 160 °C to 385 °C to a maximum of 1000 bars. Raman studies combined with fluid inclusion data limit fluid compositions to a 30.7 percent mass saline fluid with mole fractions CO_2 , N_2 , CH_4 , and H_2S in the gas phases on the order of 0.8974, 0.0261, 0.0354, and 0.0410, respectively.

The presence of two fluid inclusion populations represents conjugates of a boiling system. In this study, the petrographic work and microthermometry conclude that beryl saturated and precipitated both in the liquid and vapour stability field of a boiling system. Within the liquid portion of the boiling system, the emerald bands precipitated due to the enrichment of V, and Cr and to a lesser extent Fe. Other gem deposits display similar growth banding similar to the Byrud emerald deposit, may have precipitated via a similar model of formation. Therefore, the mechanism of boiling as mode of formation to these colour zonations can be applied not only to other emerald localities but other gem deposits such as sapphire, ruby, and semi-precious stones such as topaz and alexandrite.

A comprehensive study of the Byrud emerald has provided a more detailed understanding of vanadium-bearing emerald, which is far less studied than the chromium-rich varieties. In addition to describing and characterizing the geology,

petrogenesis, and geochemistry of the emerald deposit, this enhanced understanding of the genetic model of the Byrud emerald deposit may lead to continued exploration in the area. This model also has applications for other deposits containing colour-zoned emeralds such as those from Australia, Pakistan, Zambia, South Africa and Namibia.

Appendices

Appendix A: Sample locations and descriptions.

Table A-1. Listed locations, descriptions, samples, and measured structures from field stations.

Station ID	Easting UTM32V	Northing UTM32V	General Rock Type	Detailed Rock Description	Mineralization	Alteration	Structure Type	Strike	Dip
LEL001	620851	6700790	Shale	black sulphidic shale	Pyrite				
LEL002	620822	6700573	Quartzite?	fine-grained quartzite?	Pyrite veinlets, disseminated and cubic, sub- to mm-scale				
LEL003	620800	6700620	Shale / Syenite sill	black, fine grained sulphidic shale; light-gray, fine-grained syenite sill also observed in tunnel - quartz-rich	Pyrite observed in both, disseminated, sub to mm-scale	pervasive silicification in syenite sill	Bedding	24	26
LEL003	620800	6700620	Shale / Syenite sill	black, fine grained sulphidic shale; light-gray, fine-grained syenite sill also observed in tunnel - quartz-rich	Pyrite observed in both, disseminated, sub to mm-scale	pervasive silicification in syenite sill	Tunnel Orientation	90	
LEL003	620800	6700620	Shale / Syenite sill	black, fine grained sulphidic shale; light-gray, fine-grained syenite sill also observed in tunnel - quartz-rich	Pyrite observed in both, disseminated, sub to mm-scale	pervasive silicification in syenite sill	Bedding	360	28

Table A-1. Continued.

LEL004	619924	6699446	Hornfels	white- to dark gray with minor red and green-gray layering of silicified hornfels; cm-scale layers displaying sharp contacts; one area displays V-shaped intersect of hornfels layers	Pyrite	pervasive silicification in syenite sill	Bedding	249	72
LEL005	619967	6699341	Granite	reddish-white amphibole granite, equigranular with up to 2mm-size crystals					
LEL006	620800	6700620							
LEL007	620830	6700633	Shale	black shale, hornfels above; observed 30-50 cm primary sedimentary layering between shale and hornfels	pyrite	silicification	Tunnel Orientation	253	
LEL007	620830	6700633					Bedding	352	28
LEL008	620835	6700654	Shale				Tunnel Orientation	252	
LEL008	620835	6700654	Shale				Bedding	352	28
LEL008	620835	6700654	Pegmatite Vein	2 main vein sets	none	none	Vein Set	352	27
LEL008	620835	6700654	Shale				Bedding	210	34
LEL009	620834	6700671	Hornfels	gray to dark gray hornfels and black shale (dominantly hornfels)	pyrite	silicification	Tunnel Orientation	226	

Table A-1. Continued.

LEL009	620834	6700671	Pegmatite Vein	white to -gray crystalline pegmatite vein with hornfels at the contact; veins up to 20 cm width	emerald, fluorite; emerald crystals 0.5 cm, mostly in hornfels	silicification	Vein Set	182	18
LEL009	620834	6700671	Shale				Bedding	340	20
LEL009	620834	6700671					Contact	351	10
LEL010	620834	6700694					Tunnel Orientation	277	
LEL010	620834	6700694	Shale / Hornfels	gray to dark gray hornfels and black shale (dominantly black shale)	Pyrite	pervasive silicification	Tunnel Orientation	20	
LEL010	620834	6700694	Pegmatite Vein	white to -gray crystalline pegmatite vein with hornfels at the contact			Vein Set	190	21
LEL011	620835	6700714	Shale	black shale	Pyrite		Tunnel Orientation	356	
LEL011	620835	6700714	Pegmatite Vein	30 cm wide pegmatite vein, contact alteration - silicified hornfels, biggest vein is ~0.5 m	emerald, fluorite		Vein Set	360	0
LEL011	620835	6700714	Shale				Bedding	15	0
LEL012	620820	6700606					Tunnel Orientation	262	
LEL012	620820	6700606	Hornfels / Shale	Interlayered hornfels and shale with minor chert	Pyrite	selective silicification	Bedding	176	28
LEL013	620813	6700550	Hornfels	minor chert layer		pervasive silicification	Tunnel Orientation	328	

Table A-1. Continued.

LEL014	620814	6700491	Shale		Tunnel Orientation	240	
LEL014	620814	6700491	Shale	Shale + hornfels	Bedding	222	8
LEL015	620801	6700450	Shale		Tunnel Orientation	6	
LEL015	620801	6700450	Shale	Shale + hornfels	Bedding	12	39
LEL016	620809	6700436	Shale		Tunnel Orientation	270	
LEL016	620809	6700436	Shale		Bedding	14	32
LEL016	620809	6700436	Shale		Bedding	14	42

Table A-2. Sample descriptions of samples taken from the Byrud deposit by Peter Ihlen.

Sample #	Sample Description
LL11-01A	Unaltered bituminous black shale
LL11-01B	Black unaltered black shale consisting of organic matter, clay and minor sulphide mineralization (pyrite, pyrrhotite)
LL11-02A	Contact –metamorphic “sulphidic” black shale, biotite hornfels
LL11-02B	Contact metamorphic black shale with bleached gray silicified zones. Sulphide mineralization present: pyrite, pyrrhotite +/- Fe Oxides, and possible bornite and chalcopyrite -near emerald pegmatites
LL11-03A	Barren pegmatite enveloped by bleached black shales
LL11-03B	Barren rust-stained pegmatite in syenite sill
LL11-04A	Fresh syenite sill from lower sill hosting emerald pegmatite
LL11-04B	Fresh gray syenite sill with minor sulphide mineralization
LL11-04C	Contact-phase riebeckite granite, sulphide mineralization dominantly pyrrhotite.
LL11-05A	Pegmatite containing emerald
LL11-05B	Pegmatite containing emerald
LL11-05C	Pegmatite containing emerald
LL11-06	Pegmatite containing clear beryl
LL11-07	Zoned beryl
LL11-08a, LL11-08a-1, LL11-08a-2	Quartz crystal
LL11-08b-1, LL11-08b-2, LL11-08b-3	Quartz and feldspar crystal intergrowth + emerald

Table A-3. Sample and field photographs taken at the Byrud deposit.



Contact between pegmatite vein and black shale/hornfels, hosting subhedral to euhedral emerald and fluorite. Pencil tip for scale.



Massive pegmatite vein of colourless beryl, emerald and topaz within small cavities. Scratchers tip for scale.

Table A-3 continued.



Pegmatite vein with euhedral emerald and fluorite crystals. Vein crosscuts rusty-weathered syenite sill. Scratcher tip for scale.



Lower syenite sill at the entrance of one of the northern adits (Tunnel 1). The contacts are shown in the image as a black stippled line between the black shale and syenite sill. As well as parallel emerald-bearing pegmatite vein in contact with the sill. Hammer for scale.

Appendix B: Bulk rock geochemistry.

Four samples of the host rocks were chosen from the Byrud deposit, (1) unaltered black shale, (2) metamorphosed black shale, (3) fresh syenite sill and (4) granite and submitted for bulk rock geochemical analyses (Table B-1). Quality control data is presented in Table B-2. These samples were chosen based on the absence of alteration, veins and weathering. Samples were cut by rock saw and cleaned with water and a scrub brush to remove any weathering or oxidation staining. Approximately 50 grams of fresh sample was sent to Activation Laboratories Ltd. In Ancaster, Ontario, and analyzed for major oxides, minor and trace elements and total carbon and total sulphur. The samples were crushed in the lab, split and pulverized with mild steel. Total carbon and sulphur concentrations were acquired by infrared (IR) by the 4F-C,S Infrared method. The samples are subjected to an accelerator which causes the sample to combust in a pure oxygen environment. During combustion, the carbon and sulphur-bearing elements are reduced, binds with oxygen to form CO, CO₂ and SO₂. Carbon is measured as CO₂ in the IR cell. An Eltra CS-800 was used for the analysis. Major oxide and some minor and trace element concentrations were obtained by fusion-inductively-couple mass spectrometry (FUS-IP) by the Code 4E-Research method. The samples were mixed with a combination of lithium metaborate/lithium tetraborate and fused in a graphite crucible. The molten mixture is poured into a 5% nitric acid solution and shaken until dissolved (~ 30 minutes). The samples were run for major oxides and selected traces on a combination simultaneous/sequential Thermo Jarrell-Ash Enviro II ICP. An assortment of international reference materials and independent control standards are also analyzed for calibration. Certain minor and trace element concentrations were obtained by instrumental neutron activation analysis (INAA) obtained through the Code 4E-Research method. A 1 gram aliquot is encapsulated in a polyethylene vial and irradiated with flux wires at a thermal neutron flux of $7 \times 10^{12} \text{ n cm}^{-2} \text{ s}^{-1}$. After a seven day decay. The samples are counted on a high purity Ge detector with resolution of greater than 1.7 KeV for the 1332 KeV Co-60 photopeak. Using the flux wires, the decay-corrected activities are compared to a calibration developed from multiple certified international reference

materials. One blank and one standard were analyzed. Some minor and trace elements were analysed by total digestion ICP (TD-ICP) again with the Code 4E-Research method. The samples were digested with four acids beginning with hydrofluoric, followed by a mixture of nitric and perchloric acids, and heated to dry the samples. The samples are brought back into solution using hydrochloric acid. With this digestion certain phases may be only partially solubilized. Samples are analyzed using a Varian Vista ICP. An internal standard or certified reference material was used for quality control.

Table B-1. Major, minor, and trace element compositions of whole rock samples.

		SiO ₂ %	Al ₂ O ₃ %	Fe ₂ O ₃ %	MnO %	MgO %	CaO %	Na ₂ O %	K ₂ O %	TiO ₂ %	P ₂ O ₅ %	LOI %	Total %
Detection Limit		0.01	0.01	0.01	0.001	0.01	0.01	0.01	0.01	0.001	0.01	n.d	
Analysis Method		FUS-ICP	FUS-ICP	FUS-ICP	FUS-ICP	FUS-ICP	FUS-ICP	FUS-ICP	FUS-ICP	FUS-ICP	FUS-ICP	FUS-ICP	FUS-ICP
Sample	Description												
LL11-01B	Unaltered black shale	62.78	13.1	2.13	0.019	0.97	0.05	0.11	4.37	0.751	0.02	14.87	99.16
LL11-02B	Metamorphosed black shale	56.97	19.05	5.67	0.036	1.77	1.71	2.08	5.92	1.043	0.12	3.7	98.07
LL11-04B	Syenite sill	66.29	15.79	2.9	0.026	0.55	1.53	3.75	5.32	0.417	0.1	1.67	98.34
LL11-04C	Granite	73.88	12.1	3.04	0.111	0.06	0.2	4.03	4.55	0.132	< 0.01	0.77	98.86
		Au ppb	Ag ppm	As ppm	Ba ppm	Be ppm	Bi ppm	Br ppm	Cd ppm	Co ppm	Cr ppm	Cs ppm	Cu ppm
Detection Limit		1	0.5	1	1	1	2	0.5	0.5	0.1	0.5	0.2	1
Analysis Method		INAA	MULT INAA / TD-ICP	INAA	FUS-ICP	FUS-ICP	TD-ICP	INAA	TD-ICP	INAA	INAA	INAA	TD-ICP
Sample	Description												
LL11-01B	Unaltered black shale	7	4.3	24	827	4	< 2	2.9	< 0.5	1.3	119	9	16
LL11-02B	Metamorphosed black shale	5	0.9	21	967	55	5	< 0.5	< 0.5	19.8	108	24.6	100
LL11-04B	Syenite sill	< 1	1.3	2	2772	7	< 2	< 0.5	< 0.5	3.2	11.7	6.7	28
LL11-04C	Granite	< 1	< 0.5	3	9	6	< 2	2.3	< 0.5	1.8	14.3	1.5	31

Table B-1. Continued.

		Hf ppm	Hg ppm	Ir ppb	Mo ppm	Ni ppm	Pb ppm	Rb ppm	S %	Sb ppm	Sc ppm	Se ppm	Sr ppm
Detection Limit		0.2	1	1	2	1	5	10	0.001	0.1	0.01	0.5	2
Analysis Method		INAA	INAA	INAA	TD-ICP	TD-ICP	TD-ICP	INAA	TD-ICP	INAA	INAA	INAA	FUS-ICP
Sample	Description												
LL11-01B	Unaltered black shale	3.7	< 1	< 1	86	30	54	120	1.46	36.2	11.4	28.8	94
LL11-02B	Metamorphosed black shale	4.7	< 1	< 1	98	144	10	970	2.12	1.8	17.9	< 0.5	254
LL11-04B	Syenite sill	9.4	< 1	< 1	14	5	24	480	0.682	0.6	2.79	< 0.5	634
LL11-04C	Granite	7.6	< 1	< 1	3	2	< 5	230	0.414	0.4	2.39	< 0.5	6
		Ta ppm	Th ppm	U ppm	V ppm	W ppm	Y ppm	Zn ppm	Zr ppm	La ppm	Ce ppm	Nd ppm	Sm ppm
Detection Limit		0.3	0.1	0.1	5	1	1	1	2	0.05	1	1	0.01
Analysis Method		INAA	INAA	INAA	FUS-ICP	INAA	FUS-ICP	MULT INAA / TD-ICP	FUS-ICP	INAA	INAA	INAA	INAA
Sample	Description												
LL11-01B	Unaltered black shale	1.6	4	15.4	2720	< 1	8	39	123	10.3	12	7	1.2
LL11-02B	Metamorphosed black shale	2.1	16	35.7	899	19	40	21	184	53.9	79	62	9.46
LL11-04B	Syenite sill	7.8	19.5	12.2	13	12	26	29	464	98.5	148	68	8.67
LL11-04C	Granite	14.3	28.4	28.6	< 5	< 1	29	71	218	41	62	26	2.93

Table B-1. Continued.

		Eu ppm	Tb ppm	Yb ppm	Lu ppm	Mass g	C-Total %	Total S %
Detection Limit		0.05	0.1	0.05	0.01		0.01	0.01
Analysis Method		INAA	INAA	INAA	INAA	INAA	IR	IR
Sample	Description							
LL11-01B	Unaltered black shale	< 0.05	< 0.1	1.03	0.15	1.071	9.72	1.4
LL11-02B	Metamorphosed black shale	1.86	1.4	4.74	0.67	1.431	0.05	2.05
LL11-04B	Syenite sill	2.04	< 0.1	3.13	0.43	1.191	0.08	0.76
LL11-04C	Granite	< 0.05	< 0.1	4.43	0.78	1.497	0.06	0.44

Table B-2. Quality control data for whole rock geochemical standards and blanks.

Analyte Symbol	SiO₂	Al₂O₃	Fe₂O₃	MnO	MgO	CaO	Na₂O	K₂O	TiO₂	P₂O₅	LOI	Total
Unit Symbol	%	%	%	%	%	%	%	%	%	%	%	%
Detection Limit	0.01	0.01	0.01	0.001	0.01	0.01	0.01	0.01	0.001	0.01		0.01
Analysis Method	FUS-ICP	FUS-ICP	FUS-ICP	FUS-ICP	FUS-ICP	FUS-ICP	FUS-ICP	FUS-ICP	FUS-ICP	FUS-ICP	FUS-ICP	FUS-ICP
GXR-1 Meas												
GXR-1 Cert												
GXR-4 Meas												
GXR-4 Cert												
SDC-1 Meas												
SDC-1 Cert												
SCO-1 Meas												
SCO-1 Cert												
GXR-6 Meas												
GXR-6 Cert												
LKSD-4 Meas												
LKSD-4 Cert												
BaSO4 Meas												
BaSO4 Cert												
W-2a Meas												
W-2a Cert												
DNC-1a Meas												
DNC-1a Cert												
OREAS 13b (4-Acid) Meas												
OREAS 13b (4-Acid) Cert												

Table B-2. Continued.

Analyte Symbol	SiO₂	Al₂O₃	Fe₂O₃	MnO	MgO	CaO	Na₂O	K₂O	TiO₂	P₂O₅	LOI	Total
Unit Symbol	%	%	%	%	%	%	%	%	%	%	%	%
Detection Limit	0.01	0.01	0.01	0.001	0.01	0.01	0.01	0.01	0.001	0.01		0.01
Analysis Method	FUS-ICP	FUS-ICP	FUS-ICP	FUS-ICP	FUS-ICP	FUS-ICP	FUS-ICP	FUS-ICP	FUS-ICP	FUS-ICP	FUS-ICP	FUS-ICP
OREAS 13b (4-Acid) Meas												
OREAS 13b (4-Acid) Cert												
LL11-01B Orig												
LL11-01B Dup												
LL11-04C Orig	74.46	12.26	3.06	0.111	0.06	0.2	4.06	4.58	0.134	< 0.01	0.77	99.69
LL11-04C Dup	73.29	11.94	3.01	0.11	0.06	0.19	4.01	4.52	0.13	< 0.01	0.77	98.03
Method Blank												
Method Blank												
Method Blank												

Note: Meas –measured value, Cert –certified value, Orig –Original, Dup –Duplicate

Table B-2. Continued.

Analyte Symbol	Au	Ag	Ag	As	Ba	Be	Bi	Br	Cd	Co	Cr	Cs	Cu
Unit Symbol	ppb	ppm											
Detection Limit	1	0.5	5	1	1	1	2	0.5	0.5	0.1	0.5	0.2	1
Analysis Method	INAA	TD-ICP	INAA	INAA	FUS-ICP	FUS-ICP	TD-ICP	INAA	TD-ICP	INAA	INAA	INAA	TD-ICP
GXR-1 Meas		31.4					1390		3.3				1170
GXR-1 Cert		31					1380		3.3				1110
GXR-4 Meas		3.5					5		< 0.5				6460
GXR-4 Cert		4					19		0.86				6520
SDC-1 Meas		< 0.5					< 2		< 0.5				31
SDC-1 Cert		0.041					2.6		0.08				30
SCO-1 Meas		< 0.5					< 2		< 0.5				29
SCO-1 Cert		0.134					0.37		0.14				29
GXR-6 Meas		0.5					< 2		< 0.5				67
GXR-6 Cert		1.3					0.29		1				66
LKSD-4 Meas													
LKSD-4 Cert													
BaSO4 Meas													
BaSO4 Cert													
W-2a Meas			< 5	2						47.1	97.5	< 0.2	
W-2a Cert			0.046	1.2						43	92	0.99	
DNC-1a Meas													98
DNC-1a Cert													100
OREAS 13b (4-Acid) Meas		1											2360
OREAS 13b (4-Acid) Cert		0.86											2300

Table B-2. Continued.

Analyte Symbol	Au	Ag	Ag	As	Ba	Be	Bi	Br	Cd	Co	Cr	Cs	Cu
Unit Symbol	ppb	ppm	ppm	ppm	ppm	ppm	ppm	ppm	ppm	ppm	ppm	ppm	ppm
Detection Limit	1	0.5	5	1	1	1	2	0.5	0.5	0.1	0.5	0.2	1
Analysis Method	INAA	TD- ICP	INAA	INAA	FUS- ICP	FUS- ICP	TD- ICP	INAA	TD- ICP	INAA	INAA	INAA	TD- ICP
OREAS 13b (4-Acid) Meas													
OREAS 13b (4-Acid) Cert													
LL11-01B Orig													
LL11-01B Dup													
LL11-04C Orig					9	6							
LL11-04C Dup					9	6							
Method Blank													
Method Blank		< 0.5					< 2		< 0.5				< 1
Method Blank	< 1		< 5	< 1				< 0.5		< 0.1	< 0.5	< 0.2	

Note: Meas –measured value, Cert –certified value, Orig –Original, Dup –Duplicate

Table B-2. Continued.

Analyte Symbol	Hf	Hg	Ir	Mo	Ni	Pb	Rb	S	Sb	Sc	Se	Sr
Unit Symbol	ppm	ppm	ppb	ppm	ppm	ppm	ppm	%	ppm	ppm	ppm	ppm
Detection Limit	0.2	1	1	2	1	5	10	0.001	0.1	0.01	0.5	2
Analysis Method	INAA	INAA	INAA	TD-ICP	TD-ICP	TD-ICP	INAA	TD-ICP	INAA	INAA	INAA	FUS-ICP
GXR-1 Meas				15	45	761		0.223				
GXR-1 Cert				18	41	730		0.257				
GXR-4 Meas				313	45	48		1.79				
GXR-4 Cert				310	42	52		1.77				
SDC-1 Meas				< 2	38	25		0.065				
SDC-1 Cert				0.25	38	25		0.065				
SCO-1 Meas				< 2	32	29		0.071				
SCO-1 Cert				1.4	27	31		0.063				
GXR-6 Meas				< 2	27	92		0.014				
GXR-6 Cert				2.4	27	101		0.016				
LKSD-4 Meas												
LKSD-4 Cert												
BaSO4 Meas												
BaSO4 Cert												
W-2a Meas	2.6						< 10		0.9	36		
W-2a Cert	2.6						21		0.79	36		
DNC-1a Meas					252							
DNC-1a Cert					247							
OREAS 13b (4-Acid) Meas				8	2240			1.14				
OREAS 13b (4-Acid) Cert				9	2247			1.2				
OREAS 13b (4-Acid) Meas												
OREAS 13b (4-Acid) Cert												

Table B-2. Continued.

Analyte Symbol	Hf	Hg	Ir	Mo	Ni	Pb	Rb	S	Sb	Sc	Se	Sr
Unit Symbol	ppm	ppm	ppb	ppm	ppm	ppm	ppm	%	ppm	ppm	ppm	ppm
Detection Limit	0.2	1	1	2	1	5	10	0.001	0.1	0.01	0.5	2
Analysis Method	INAA	INAA	INAA	TD- ICP	TD- ICP	TD- ICP	INAA	TD- ICP	INAA	INAA	INAA	FUS- ICP
LL11-01B Orig												
LL11-01B Dup												
LL11-04C Orig												6
LL11-04C Dup												6
Method Blank												
Method Blank				< 2	< 1	< 5		<0.001				
Method Blank	< 0.2	< 1	< 1				< 10		< 0.1	< 0.01	< 0.5	

Note: Meas –measured value, Cert –certified value, Orig –Original, Dup –Duplicate

Table B-2. Continued.

Analyte Symbol	Eu	Tb	Yb	Lu	Mass	C-Total	Total S
Unit Symbol	ppm	ppm	ppm	ppm	g	%	%
Detection Limit	0.05	0.1	0.05	0.01		0.01	0.01
Analysis Method	INAA	INAA	INAA	INAA	INAA	IR	IR
GXR-1 Meas							
GXR-1 Cert							
GXR-4 Meas							
GXR-4 Cert							
SDC-1 Meas							
SDC-1 Cert							
SCO-1 Meas							
SCO-1 Cert							
GXR-6 Meas							
GXR-6 Cert							
LKSD-4 Meas						18.8	0.97
LKSD-4 Cert						17.7	0.99
BaSO4 Meas							14.1
BaSO4 Cert							14
W-2a Meas	1.13	0.6	2.2	0.34			
W-2a Cert	1	0.63	2.1	0.33			
DNC-1a Meas							
DNC-1a Cert							
OREAS 13b (4-Acid) Meas							1.18
OREAS 13b (4-Acid) Cert							1.2
OREAS 13b (4-Acid) Meas							1.11
OREAS 13b (4-Acid) Cert							1.2
LL11-01B Orig						9.74	1.41
LL11-01B Dup						9.7	1.39
LL11-04C Orig							
LL11-04C Dup							

Table B-2. Continued.

Method Blank						< 0.01	< 0.01
Method Blank							
Method Blank	< 0.05	< 0.1	< 0.05	< 0.01	1		

Note: Meas –measured value, Cert –certified value, Orig –Original, Dup –Duplicate

Appendix C: Fluid inclusion data.

Table C-1. *Microthermometric measurements on the fluid inclusions from the Byrud deposit in emerald, quartz and fluorite.*

finc number	Mineral	Tn cla	Tn ice	Tm ice	Tn CO₂	Tm CO₂	Tm hydrohalite	Tm cla	Tmhal	Th total	Fluid Inclusion Assemblages
1	Emerald	-38.4	-58.3	-3.9	nv	nv	nv	11.1	nv	383.3	S (1)
2	Emerald	-35.7	-54.3	-3.8	nv	nv	nv	11.4	nv	380.2	S(1)
3	Emerald	-36.1	-55.4	-3.8	nv	nv	nv	11.3	nv	376.4	S (1)
4	Emerald	-34.8	-36.7	-3.7	nv	nv	nv	nv	nv	348.9	PS(1)
5	Emerald	nv	-36.5	-3.1	nv	nv	nv	nv	nv	nv	PS (1)
6	Emerald	nv	-36.4	-3.4	nv	nv	nv	nv	nv	362.4	PS (1)
7	Emerald	-30.4	-52.4	-2.0	nv	nv	nv	12.1	nv	280.4	P (1)
8	Emerald	-31.4	-58.5	-2.1	nv	nv	nv	11.9	nv	309.7	P (1)
9	Emerald	nv	-53.7	-1.9	nv	nv	nv	nv	nv	275.9	P (1)
10	Emerald	nv	-82.4	-0.5	nv	nv	nv	12.7	nv	280.2	S (2)
11	Emerald	-38.4	-55.7	-4.1	-107.9	-56.6	nv	9.8	nv	nv	P (3)
12	Emerald	-48.2	-62.4	-4.7	nv	nv	nv	10.5	nv	290.2	S(4)
13	Emerald	-48.7	-61.4	-3.9	nv	nv	nv	nv	nv	287.4	S(4)
14	Emerald	-38.7	-58.4	-3.7	nv	nv	nv	11.2	nv	375.1	PS (5)
15	Emerald	-39.8	-54.2	-2.5	-103.4	-55.2	nv	9.1	nv	352.8	PS (6)
16	Emerald	-37.9	-57.4	-2.9	-109.9	-52.4	nv	10.6	nv	371.1	PS (6)

Table C-1. Continued.

17	Emerald	nv	-42.5	-0.2	nv	nv	nv	nv	nv	271.4	S (7)
18	Emerald	-45.9	-66.7	-1.5	nv	nv	nv	10.7	nv	297.8	PS (8)
19	Emerald	nv	-51.2	-0.8	nv	nv	nv	nv	nv	270.1	S (9)
20	Emerald	-40.5	-58.4	-0.1	nv	nv	nv	12.1	nv	261.4	S (10)
21	Emerald	-48.1	-57.6	-4.6	nv	nv	nv	nv	nv	281.4	S (11)
22	Emerald	nv	-51.6	-3.5	nv	nv	nv	nv	nv	218.2	S(12)
23	Emerald	nv	-50.1	-3.4	nv	nv	nv	nv	nv	178.1	S(12)
24	Emerald	-48.4	-53.4	-3.5	nv	nv	nv	9.8	nv	251.2	S(12)
25	Emerald	-46.2	-49.8	-4.1	nv	nv	nv	nv	nv	230.2	P (13)
26	Emerald	-43.6	-52.2	-4.3	nv	nv	nv	11.0	nv	229.4	P (13)
27	Emerald	-45.2	-50.9	-4.2	nv	nv	nv	11.2	nv	238.4	P (13)
28	Emerald	-44.1	-53.4	-2.4	nv	nv	nv	11.4	nv	200.1	P (14)
29	Emerald	-44.4	-53.5	-2.5	nv	nv	nv	nv	nv	199.8	P (14)
30	Emerald	nv	-53.9	-2.5	nv	nv	nv	nv	nv	161.2	P (14)
31	Emerald	-45.9	-56.7	-3.4	nv	nv	nv	nv	nv	267.1	S (15)
32	Emerald	-51.6	-57.8	-5.1	nv	nv	nv	nv	nv	285.4	S (16)
33	Emerald	-50.4	-61.3	-5.1	nv	nv	nv	10.4	nv	231.4	S (16)
34	Emerald	-52.4	-60.1	-5.0	nv	nv	nv	10.8	nv	248.5	S (16)
35	Emerald	-55.9	-60.4	-5.3	nv	nv	nv	11.0	nv	194.5	P (17)
36	Emerald	-53.4	-67.6	-5.7	nv	nv	nv	nv	nv	237.4	S (18)
37	Emerald	nv	-60.4	-5.8	nv	nv	nv	nv	nv	239.7	S (19)

Table C-1. Continued.

38	Emerald	nv	-84.2	-25.1	nv	nv	-1.1	nv	161.2	317.9	S (20)
39	Emerald	nv	-87.4	-22.5	nv	nv	-0.5	10.3	168	287.9	S (20)
40	Emerald	nv	-84	-29.4	nv	nv	nv	11.8	179.2	259.4	S (21)
41	Emerald	-63.4	-89.4	-23.4	nv	nv	-5.1	10.3	192.4	264.2	S (22)
42	Emerald	nv	-89.2	-24.1	nv	nv	-5.5	10.8	185.4	221.0	S (23)
43	Emerald	nv	-86.4	-19.1	nv	nv	-0.3	nv	184.1	290.2	S (24)
44	Emerald	nv	-89.4	-20.5	nv	nv	-0.4	nv	178.2	292.4	S (25)
45	Emerald	nv	-89.6	-25.2	nv	nv	-5.6	nv	182.1	231.7	S (26)
46	Emerald	nv	-88.1	-23.9	nv	nv	-5.4	nv	175.7	234.1	S (27)
47	Emerald	nv	-89.9	-26.8	nv	nv	-5.1	14.2	173.2	242.7	S (28)
48	Emerald	-72.1	-78.4	-22.1	nv	nv	-4.8	13.8	169.4	298.4	S (28)
49	Emerald	nv	-89.7	-19.8	nv	nv	-4.1	nv	nv	nv	S (29)
50	Emerald	nv	-88.7	-27.4	nv	nv	-4.2	nv	178.4	301.4	S (30)
51	Emerald	nv	-89.4	-25.1	nv	nv	-4.5	nv	169.2	237.4	S (31)
52	Emerald	nv	-88.9	-18.3	nv	nv	-4.5	nv	152.4	238.2	S (31)
53	Emerald	nv	-87.1	-25.2	nv	nv	-4.0	nv	164.2	319.4	S (32)
54	Quartz	-38.2	-62.1	-29.1	nv	nv	-1.1	nv	218.1	386.4	S (33)
55	Quartz	-40.2	-58.2	-24.9	nv	nv	-0.8	12.3	217.8	385.6	S (33)
56	Quartz	-38.7	-61.7	-23.6	nv	nv	nv	13.0	218.9	390.1	S (33)
57	Quartz	-30.1	-86.1	-28.8	-101.2	-51.5	nv	12.2	242.1	>420	S (34)
58	Quartz	nv	-52.3	-21.7	nv	nv	nv	nv	194.2	380.2	S (35)

Table C-1. Continued.

59	Quartz	nv	-51.6	-24.9	nv	nv	nv	nv	246.1	420.2	S (36)
60	Quartz	nv	-68	-25.1	nv	nv	nv	nv	244.1	412.1	S (36)
61	Quartz	nv	-62	-24.8	nv	nv	nv	nv	242.4	414.3	S (36)
62	Quartz	-40.2	-51.7	-4.3	-109.2	-55.6	nv	9.2	nv	>420	S (37)
63	Quartz	-42.5	-71.9	-6.1	-106.5	-53.7	nv	10.4	nv	>420	S (38)
64	Quartz	-45.3	-57.2	-5.4	-106.3	-53.9	nv	10.1	nv	>420	S (38)
65	Quartz	-43.2	-50.2	-5.2	-107.1	-53.7	nv	9.8	nv	>420	S (38)
66	Quartz	-37.4	-48.9	-2.4	-108.4	-54.9	nv	8.9	nv	>420	S (39)
67	Quartz	-38.4	-50.5	-4.9	-106.1	-53.6	nv	9.7	nv	>420	S (40)
68	Quartz	-38.2	-49.7	-5.0	-106.3	-53.7	nv	9.5	nv	>420	S (40)
69	Quartz	-47.2	-54.1	-6.2	-104.5	-53.1	nv	9.5	nv	>420	S (41)
70	Quartz	-41.2	-55.4	-5.8	-105.2	-53.9	nv	10.1	nv	>420	S (41)
71	Quartz	nv	-75.4	-20.2	nv	nv	-1.2	nv	196.4	>420	S (41)
72	Quartz	-44.1	-72.6	-28.4	-105.7	-53.8	-1.2	11.9	250.2	373.2	S (42)
73	Quartz	-38.8	-68.3	-24.8	nv	nv	nv	12.2	231.5	335.4	S (42)
74	Quartz	-37.9	-65.4	nv	nv	nv	-0.8	11.8	232.7	361.2	S (42)
75	Quartz	-34.5	-60.4	-1.6	-101.2	-53.7	nv	10.7	nv	>420	S (43)
76	Quartz	-34.7	-57.8	-1.9	-102.1	-56.6	nv	9.2	nv	>420	S (43)
77	Quartz	-39.1	-67.5	-24.2	nv	nv	nv	nv	255.2	398.5	S (44)
78	Quartz	-38.4	-68.1	-26.1	nv	nv	nv	12.1	260.1	396.1	S (44)
79	Quartz	nv	-79.2	-21.6	nv	nv	nv	nv	257.7	270.1	S (45)

Table C-1. Continued.

80	Quartz	nv	-75.7	-22.1	nv	nv	nv	nv	253.4	258.1	S (45)
81	Quartz	nv	-81.4	-25.8	nv	nv	nv	nv	258.1	281.6	S (45)
82	Quartz	-34.0	nv	-3.1	-98.7	-53.5	nv	11.2	nv	>400	S (46)
83	Quartz	nv	-38.6	-1.1	nv	nv	nv	nv	nv	300.9	S (47)
84	Quartz	nv	-36.7	-0.9	nv	nv	nv	nv	nv	301.2	S (47)
85	Quartz	nv	-36.5	-0.8	nv	nv	nv	nv	nv	291.7	S (47)
86	Fluorite	nv	-55.2	-3.2	nv	nv	nv	nv	nv	344.2	S (48)
87	Fluorite	nv	-60.7	-3.9	nv	nv	nv	nv	nv	366.5	S (49)
88	Fluorite	nv	-61.2	-3.5	nv	nv	nv	nv	nv	367.2	S (49)
89	Fluorite	nv	-53.7	-3.6	nv	nv	nv	nv	nv	377.1	S (50)
90	Fluorite	nv	-60.1	0.0	nv	nv	nv	nv	nv	261.4	S (51)
91	Fluorite	nv	-62.5	-1.4	nv	nv	nv	nv	nv	339.2	S (52)
92	Fluorite	nv	-62.6	-6.1	nv	nv	nv	nv	nv	332.1	S (53)
93	Fluorite	nv	-57.7	-4.9	nv	nv	nv	nv	nv	375.8	S (54)
94	Fluorite	nv	-52.4	-4.2	nv	nv	nv	nv	nv	310.4	S (55)
95	Fluorite	nv	-51.2	-2.9	nv	nv	nv	nv	nv	388.4	S (56)
96	Fluorite	nv	-54.5	-2.8	nv	nv	nv	nv	nv	290.1	S (57)
97	Fluorite	nv	-40.1	-0.2	nv	nv	nv	nv	nv	324.2	S (58)
98	Fluorite	nv	-45.9	-2.4	nv	nv	nv	nv	nv	328.5	S (59)
99	Fluorite	nv	-39.4	-4.8	nv	nv	nv	nv	nv	294.1	S (60)
100	Fluorite	nv	-47.2	-1.8	nv	nv	nv	nv	nv	327/4	S (61)

Table C-1. Continued.

101	Fluorite	nv	-39.8	-0.5	nv	nv	nv	nv	nv	280.2	S (62)
102	Fluorite	nv	-40.2	-0.9	nv	nv	nv	nv	nv	300.7	S (62)
103	Fluorite	nv	-53.4	-5.1	nv	nv	nv	nv	nv	376.3	S (63)
104	Fluorite	nv	-52.7	-2.1	nv	nv	nv	nv	nv	311.6	PS (64)
105	Fluorite	nv	-50.1	-1.9	nv	nv	nv	nv	nv	294.2	S (65)

All temperatures reported in Celsius, Tn cla=Clathrate nucleation temperature, Tn ice=Ice nucleation temperature, Tm ice=Ice melting temperature, Tm cla=Clathrate melting temperature, Tn CO₂= solid CO₂ nucleation temperature, Tm CO₂= solid CO₂ melting temperature, Tm hydrohalite=hydrohalite melt temperature, Tm hal=halite melting/dissolution temperature, Th total= final homogenization temperature to a one-phase fluid, nv=not visible, P=primary, S=secondary, PS=pseudo-secondary, (1),(2),(3)=individual fluid inclusion assemblage.

Appendix D: Electron microprobe analysis

A second set of electron microprobe analyses were conducted at the University of British Columbia. Carbon-coated polished thin sections of the three emerald crystals previously imaged by CL at Simon Fraser University were analysed on a fully automated CAMECA SX-50 microprobe operating in the wavelength-dispersion mode. Analyses are presented in table B-1. Operating conditions were set to an excitation voltage of 15 kV, beam current of 20 nA, peak count time of 50s, and background count-time of 25s (20s Na, Al, Si peak count time, 10s background count-time), with a spot diameter of 10 μm for standards and specimens. Data reduction was done using the 'PAP' $\Phi(\rho\alpha Z)$ method (Pouchou and Pichoir 1985). For the elements considered, the following standards, X-ray lines and crystals were used: albite, NaK_{α} , AlK_{α} , SiK_{α} , TAP; diopside, MgK_{α} , TAP; diopside, CaK_{α} , PET; orthoclase, KK_{α} , PET; elemental Sc, Sc K_{α} , PET; rutile, TiK_{α} , PET; elemental V, VK_{α} , PET; synthetic magnesiochromite, CrK_{α} , LIF; synthetic rhodonite, MnK_{α} , LIF; synthetic fayalite, FeK_{α} , LIF; gahnite, ZnK_{α} , LIF; pollucite, CsL_{α} , PET.

Table D-1. Compositions of the Byrud emerald from electron microprobe analysis.

Oxide (%)	LEL12_ veinB-1	LEL12_ veinB-2	LEL12_ veinB-3	LEL12_ veinB-4	LEL12_ veinB-5	LEL12_ veinB-6	LEL12_ veinB-7	LEL12_ veinB-8	LEL12_ emB-1	LEL12_ emB-2	LEL12_ emB-3	LEL12_ emB-4
SiO ₂	66.773	66.158	66.984	66.221	66.764	65.910	66.328	66.381	66.846	66.709	66.378	66.159
TiO ₂	0.020	0.021	0.001	0.011	0.014	0.012	0.000	0.021	0.002	0.000	0.017	0.009
Al ₂ O ₃	18.468	18.592	18.470	18.233	18.268	17.894	18.134	18.173	18.786	18.522	18.720	18.624
Sc ₂ O ₃	0.001	0.003	0.000	0.019	0.000	0.007	0.000	0.105	0.010	0.012	0.000	0.000
V ₂ O ₃	0.147	0.131	0.173	0.184	0.413	1.005	0.868	0.399	0.048	0.056	0.049	0.066
Cr ₂ O ₃	0.029	0.011	0.013	0.059	0.031	0.149	0.125	0.009	0.020	0.010	0.014	0.000
La ₂ O ₃	0.000	0.000	0.000	0.000	0.000	0.000	0.000	0.000	0.000	0.000	0.000	0.000
Ce ₂ O ₃	0.000	0.000	0.000	0.000	0.000	0.000	0.000	0.000	0.000	0.000	0.000	0.000
BeO	13.877	13.877	13.877	13.877	13.877	13.877	13.877	13.877	13.877	13.877	13.877	13.877
MgO	0.089	0.079	0.094	0.103	0.126	0.057	0.056	0.078	0.067	0.080	0.092	0.078
CaO	0.005	0.002	0.000	0.000	0.001	0.001	0.008	0.015	0.014	0.005	0.002	0.000
MnO	0.000	0.000	0.011	0.000	0.006	0.010	0.000	0.021	0.000	0.000	0.010	0.009
FeO	0.128	0.103	0.139	0.161	0.206	0.059	0.073	0.185	0.044	0.094	0.067	0.061
ZnO	0.000	0.032	0.000	0.000	0.033	0.000	0.000	0.016	0.000	0.023	0.010	0.009
Li ₂ O	0.000	0.000	0.000	0.000	0.000	0.000	0.000	0.000	0.000	0.000	0.000	0.000
Na ₂ O	0.104	0.096	0.113	0.136	0.095	0.059	0.070	0.109	0.073	0.080	0.069	0.064
K ₂ O	0.012	0.016	0.014	0.021	0.022	0.004	0.000	0.010	0.007	0.002	0.018	0.011
Rb ₂ O	0.000	0.000	0.000	0.000	0.000	0.000	0.000	0.000	0.000	0.000	0.000	0.000
Cs ₂ O	0.008	0.033	0.005	0.023	0.000	0.000	0.009	0.000	0.000	0.029	0.019	0.043
H ₂ O	0.340	0.846	0.108	0.954	0.144	0.955	0.452	0.602	0.208	0.501	0.659	0.992

Table D-1. Continued.

Oxide (%)	LEL12_emB-5	LEL12_emB-6	LEL12_emB-7	LEL12_emB-8	LEL12_emB-9	LEL12_emB-10	LEL12_emB-11	LEL12_emB-12	LEL12_emB-13	LEL12_emB-14	LEL12_emB-15	LEL12_emB-16
SiO ₂	66.780	66.733	66.105	66.126	66.030	66.216	66.438	65.913	65.946	66.129	65.969	64.239
TiO ₂	0.000	0.000	0.010	0.015	0.013	0.020	0.033	0.041	0.003	0.050	0.018	0.008
Al ₂ O ₃	18.521	18.562	18.429	17.778	18.179	18.119	17.781	17.497	17.817	17.416	17.493	16.852
Sc ₂ O ₃	0.006	0.009	0.016	0.057	0.000	0.009	0.068	0.057	0.025	0.056	0.049	0.056
V ₂ O ₃	0.094	0.077	0.071	0.934	0.546	0.519	1.003	0.929	0.828	0.886	1.197	1.875
Cr ₂ O ₃	0.022	0.039	0.006	0.298	0.209	0.160	0.087	0.346	0.152	0.401	0.302	0.390
La ₂ O ₃	0.000	0.000	0.000	0.000	0.000	0.000	0.000	0.000	0.000	0.000	0.000	0.000
Ce ₂ O ₃	0.000	0.000	0.000	0.000	0.000	0.000	0.000	0.000	0.000	0.000	0.000	0.000
BeO	13.877	13.877	13.877	13.877	13.877	13.877	13.877	13.877	13.877	13.877	13.877	13.877
MgO	0.086	0.078	0.070	0.108	0.141	0.124	0.114	0.174	0.093	0.157	0.132	0.095
CaO	0.009	0.006	0.002	0.019	0.000	0.000	0.005	0.008	0.002	0.013	0.005	0.005
MnO	0.000	0.000	0.000	0.000	0.026	0.005	0.008	0.020	0.005	0.000	0.020	0.000
FeO	0.093	0.094	0.044	0.136	0.131	0.177	0.210	0.154	0.145	0.186	0.212	0.138
ZnO	0.000	0.034	0.000	0.000	0.000	0.040	0.001	0.033	0.000	0.000	0.000	0.000
Li ₂ O	0.000	0.000	0.000	0.000	0.000	0.000	0.000	0.000	0.000	0.000	0.000	0.000
Na ₂ O	0.092	0.074	0.084	0.091	0.150	0.117	0.120	0.145	0.107	0.172	0.152	0.114
K ₂ O	0.001	0.010	0.010	0.018	0.018	0.020	0.019	0.018	0.004	0.023	0.036	0.018
Rb ₂ O	0.000	0.000	0.000	0.000	0.000	0.000	0.000	0.000	0.000	0.000	0.000	0.000
Cs ₂ O	0.023	0.018	0.035	0.028	0.021	0.020	0.006	0.003	0.034	0.007	0.046	0.023
H ₂ O	0.396	0.391	1.242	0.515	0.659	0.578	0.230	0.786	0.962	0.630	0.494	2.312

Table D-1. Continued.

Oxide (%)	LEL12_ emA-1	LEL12_ emA-2	LEL12_ emA-3	LEL12_ emA-4	LEL12_ emA-5	LEL12_ emA-6	LEL12_ emA-7	LEL12_ emA-8	LEL12_ emA-9	LEL12_ emA-10
SiO₂	65.639	66.057	66.148	66.282	65.967	66.196	66.303	65.775	66.000	65.895
TiO₂	0.002	0.009	0.012	0.069	0.117	0.000	0.013	0.000	0.031	0.001
Al₂O₃	17.722	18.169	18.399	18.523	17.997	18.611	18.601	18.540	18.588	18.594
Sc₂O₃	0.035	0.000	0.017	0.093	0.244	0.045	0.037	0.055	0.024	0.046
V₂O₃	1.031	0.620	0.310	0.144	0.015	0.017	0.000	0.011	0.000	0.012
Cr₂O₃	0.147	0.080	0.041	0.000	0.000	0.000	0.003	0.000	0.024	0.000
La₂O₃	0.000	0.000	0.000	0.000	0.000	0.000	0.000	0.000	0.000	0.000
Ce₂O₃	0.000	0.000	0.000	0.000	0.000	0.000	0.000	0.000	0.000	0.000
BeO	13.877	13.877	13.877	13.877	13.877	13.877	13.877	13.877	13.877	13.877
MgO	0.117	0.105	0.115	0.081	0.163	0.098	0.080	0.076	0.062	0.050
CaO	0.007	0.001	0.003	0.000	0.000	0.007	0.002	0.000	0.000	0.000
MnO	0.026	0.004	0.008	0.006	0.001	0.017	0.000	0.000	0.000	0.015
FeO	0.184	0.148	0.145	0.100	0.339	0.154	0.164	0.154	0.157	0.128
ZnO	0.000	0.000	0.055	0.025	0.000	0.043	0.000	0.000	0.031	0.000
Li₂O	0.000	0.000	0.000	0.000	0.000	0.000	0.000	0.000	0.000	0.000
Na₂O	0.124	0.099	0.086	0.114	0.196	0.128	0.148	0.117	0.147	0.080
K₂O	0.021	0.016	0.019	0.015	0.024	0.019	0.013	0.026	0.022	0.010
Rb₂O	0.000	0.000	0.000	0.000	0.000	0.000	0.000	0.000	0.000	0.000
Cs₂O	0.028	0.022	0.024	0.006	0.086	0.013	0.033	0.011	0.005	0.039
H₂O	1.043	0.794	0.744	0.664	0.975	0.778	0.727	1.359	1.034	1.254

Table D-1. Continued.

Oxide (%)	LL12-emA-11	LL12-emA-12	LL12-emA-13	LL12-emA-14	LL12-emA-15	LL12-emA-16	LL12-emA-17
SiO₂	65.970	65.739	65.713	65.631	66.096	65.487	66.328
TiO₂	0.000	0.000	0.038	0.000	0.018	0.027	0.015
Al₂O₃	18.605	18.436	18.355	18.339	18.402	18.454	18.388
Sc₂O₃	0.053	0.035	0.105	0.108	0.119	0.000	0.000
V₂O₃	0.025	0.000	0.011	0.009	0.000	0.057	0.131
Cr₂O₃	0.010	0.000	0.000	0.000	0.000	0.015	0.022
La₂O₃	0.000	0.000	0.000	0.000	0.000	0.000	0.000
Ce₂O₃	0.000	0.000	0.000	0.000	0.000	0.000	0.000
BeO	13.877	13.877	13.877	13.877	13.877	13.877	13.877
MgO	0.039	0.058	0.056	0.069	0.056	0.073	0.099
CaO	0.009	0.000	0.002	0.000	0.014	0.000	0.000
MnO	0.000	0.011	0.006	0.000	0.004	0.000	0.009
FeO	0.098	0.121	0.096	0.143	0.133	0.055	0.126
ZnO	0.024	0.043	0.003	0.044	0.000	0.000	0.000
Li₂O	0.000	0.000	0.000	0.000	0.000	0.000	0.000
Na₂O	0.075	0.108	0.104	0.117	0.082	0.073	0.069
K₂O	0.006	0.019	0.025	0.010	0.026	0.003	0.015
Rb₂O	0.000	0.000	0.000	0.000	0.000	0.000	0.000
Cs₂O	0.019	0.026	0.036	0.026	0.050	0.029	0.067
H₂O	1.192	1.528	1.573	1.629	1.124	1.851	0.854

Note: All analyses are calculated based on 18 oxygen and 3 beryllium. H₂O is calculated by difference from the sum of all oxides.